UNIVERSIDADE FEDERAL DO CEARÁ

CENTRO DE CIÊNCIAS

DEPARTAMENTO DE FÍSICA

PROGRAMA DE PÓS-GRADUAÇÃO EM FÍSICA

DOUTORADO EM FÍSICA

MICHAEL TORRES RAMIREZ

CHANNEL INSTABILITY IN BINARY MIXTURES WITH DIFFERENTIAL DIFFUSIVITY

FORTALEZA

2025

MICHAEL TORRES RAMIREZ

CHANNEL INSTABILITY IN BINARY MIXTURES WITH DIFFERENTIAL DIFFUSIVITY

Tese apresentada ao Programa de Pós-Graduação em Física do Centro de Ciências da Universidade Federal do Ceará, como requisito parcial à obtenção do título de doutor em Física. Área de Concentração: Física

FORTALEZA

2025

Dados Internacionais de Catalogação na Publicação
Universidade Federal do Ceará
Sistema de Bibliotecas
Gerada automaticamente pelo módulo Catalog, mediante os dados fornecidos pelo(a) autor(a)

R139c Ramirez, Michael Torres.
Channel Instability in binary mixtures with Differential Diffusivity / Michael Torres Ramirez. – 2025.
89 f. : il. color.

Tese (doutorado) – Universidade Federal do Ceará, Centro de Ciências, Programa de Pós-Graduação em Física , Fortaleza, 2025.
Orientação: Prof. Dr. André Auto Moreira.

1. Active matter. 2. Rupture dynamics. I. Título.

CDD 530

MICHAEL TORRES RAMIREZ

CHANNEL INSTABILITY IN BINARY MIXTURES WITH DIFFERENTIAL DIFFUSIVITY

Tese apresentada ao Programa de Doutorado em Física do Programa de Pós-Graduação em Física do Centro de Ciências da Universidade Federal do Ceará, como requisito parcial à obtenção do título de doutor em Física. Área de Concentração: Física

Aprovada em: 16/05/2025

BANCA EXAMINADORA

Prof. Dr. André Auto Moreira (Orientador)
Universidade Federal do Ceará (UFC)

Prof. Dr. César Ivan Nunes Sampaio Filho
Universidade Federal do Ceará (UFC)

Prof. Dr. Saulo Davi Soares e Reis
Universidade Federal do Ceará (UFC)

Prof. Dr. Francisca Guzmán Lastra
Universidad de Chile (UCh)

Prof. Dr. Tayroni Francisco de Alencar Alves
Universidade Federal do Piauí (UFPI)

A mi familia...

AGRADECIMENTOS

Agradezco a mis padres por todo su sacrificio y por creer siempre en mí; a mis hermanos, porque siempre me han apoyado y, a pesar de la distancia, siempre han estado presentes; a mi novia, Milena, por todo su amor y apoyo en todo momento; a Kira; y a todos los miembros de mi familia que han sido parte de esta etapa tan feliz de mi vida.

Quiero agradecer a mi orientador, el profesor André, por toda la confianza y libertad que me brindó durante el doctorado. Gracias a él, fueron años tranquilos y de mucho aprendizaje. También agradezco a los demás profesores del grupo con quienes compartí y de quienes aprendí mucho, como el profesor Soares, el profesor César, a todos los demás profesores y miembros del departamento.

Agradezco a mis amigos, que, a pesar de mi dificultad con la distancia, siempre estuvieron pendientes; a todas las personas que conocí durante estos seis años en Brasil y de quienes aprendí mucho, como mis amigos del laboratorio: Israel, Marciel, Edson, Rafael, Germano, Samuel, Laisa, Koala, Victor y Hermes.

También quiero agradecer a mis amigos que compartieron conmigo la experiencia de ser extranjeros y estar lejos de nuestros países: William, Erik, Tamia, Yenny y Alejandra, por todas las risas y momentos vividos.

Quiero agradecer al profesor Diego Gallego, porque me ayudó a confiar más en mis capacidades y, de algún modo, me motivó a continuar con la física. También agradezco a Ludwing por toda la ayuda que me brindó desde el comienzo en Brasil.

Gracias a todas las personas que, de una u otra forma, hicieron esto posible.

This study was financed in part by the Coordenação de Aperfeiçoamento de Pessoal de Nível Superior - Brasil (CAPES) - Finance Code 001.

ABSTRACT

Rupture dynamics and pinch-off phenomena are essential to understanding instabilities in both fluid dynamics and biological systems. In this thesis, I study the rupture behavior of two-dimensional, channel-like structures formed in a binary mixture of particles with differential diffusivities. Using computational simulations, I explore the evolution of these instabilities under a variety of conditions, focusing on the roles of key parameters such as aspect ratio, particle density, and external drift. Although the observed behavior bears similarities to the Plateau-Rayleigh instability (PRI), the underlying mechanism is fundamentally different, as PRI is inherently three-dimensional. Instead, the instability investigated here emerges from non-equilibrium interactions unique to two-dimensional systems. Notably, comparable behaviors have been reported in chiral fluids, supporting the idea that this is a genuinely new type of instability. The results presented in this work indicate that the instability is not a finite-size effect but an intrinsic feature of systems driven by differential diffusivity. In the latter part of the thesis, I extend the analysis to study the surface dynamics of the active interface. By applying tools from capillary wave theory, I show that the interface roughening follows equilibrium-like scaling laws, even though the system is inherently out of equilibrium. This surprising result allows for the definition of an effective surface tension, whose evolution reveals a gradual weakening of interfacial cohesion leading up to rupture. These findings provide a deeper understanding of how non-equilibrium forces shape interface behavior and suggest new avenues for investigating instability and pattern formation in active matter.

Keywords: active matter; rupture dynamics.

RESUMO

A dinâmica de ruptura e os fenômenos de estrangulamento (pinch-off) são essenciais para a compreensão de instabilidades tanto em sistemas de dinâmica de fluidos quanto em sistemas biológicos. Nesta tese, estudo o comportamento de ruptura de estruturas bidimensionais semelhantes a canais, formadas em uma mistura binária de partículas com difusividades diferenciais. Utilizando simulações computacionais, exploro a evolução dessas instabilidades sob uma variedade de condições, com foco no papel de parâmetros-chave como a razão de aspecto, a densidade de partículas e o arrasto externo. Embora o comportamento observado apresente semelhanças com a instabilidade de Plateau-Rayleigh (PRI), o mecanismo subjacente é fundamentalmente diferente, uma vez que a PRI é intrinsecamente tridimensional. A instabilidade investigada aqui, por outro lado, emerge de interações fora do equilíbrio, características de sistemas bidimensionais. Comportamentos semelhantes têm sido relatados em fluidos quirais, o que reforça a ideia de que estamos diante de uma nova tipo de instabilidade. Os resultados apresentados neste trabalho indicam que essa instabilidade não é um efeito de tamanho finito, mas sim uma característica intrínseca de sistemas impulsionados por difusividades diferenciais. Na parte final da tese, amplio a análise para estudar a dinâmica da superfície da interface ativa. Aplicando ferramentas da teoria das ondas capilares, demonstro que o enrugamento da interface segue leis de escala típicas do equilíbrio, mesmo que o sistema esteja intrinsecamente fora do equilíbrio. Este resultado permite definir uma tensão superficial efetiva, cuja evolução revela um enfraquecimento gradual da coesão interfacial até a ruptura. Essas descobertas fornecem uma compreensão mais profunda de como forças fora do equilíbrio moldam o comportamento das interfaces e sugerem novos caminhos para investigar instabilidades e formação de padrões em sistemas de matéria ativa.

Palavras-chave: matéria ativa; dinâmicas de ruptura.

LIST OF FIGURES

CONTENTS

1 INTRODUCTION: EMERGENT BEHAVIOR IN ACTIVE MATTER

The laws of physics provide universal principles for describing natural phenomena, from the interactions of microscopic particles to the behavior of living systems. Statistical mechanics exemplifies this approach by using probabilistic laws to relate the behavior of large assemblies of entities, often on the order of Avogadro's number, to a small set of macroscopic state variables, under the assumption of thermodynamic equilibrium [5]. However, many systems, particularly in biology, operate far from equilibrium, where features such as energy dissipation, intrinsic fluctuations, and irreversible dynamics are essential for sustaining life. These non-equilibrium systems challenge traditional frameworks and demand new approaches to understand how complexity can emerge from seemingly disordered interactions [6].

Active matter exemplifies far-from-equilibrium systems, describing individual agents that dissipate energy locally to self-propel or exert forces [7]. These systems span a wide range of scales, from bacterial colonies to macroscopic animals [8, 9], and exhibit collective phenomena absent in passive matter, such as spontaneous flocking (emergence of alignment without external forces) [10, 11], motility-induced phase separation (density clustering driven by self-propulsion) [12, 13], and demixing in mixtures with differential diffusivity [4]. Such behaviors emerge from the interplay of local energy dissipation, particle interactions, and broken time-reversal symmetry, raising fundamental questions: How do microscopic rules dictate macroscopic order? Can equilibrium concepts like surface tension or stiffness be extended to active matter, or do they require redefinition?

This thesis investigates how non-equilibrium energy injection transform collective phenomena and interfacial stability in active matter, focusing on a novel two-dimensional instability in a binary mixture of particles with differential diffusivity. Inspired by the Plateau-Rayleigh instability (PRI), where surface tension ruptures a fluid column into droplets to minimize energy [14], this work explores a visually analogous but intrinsically distinct process in active systems. Unlike passive fluids, active matter present energy dissipation at the microscale, which alters the forces governing pattern formation. Recent studies reveal that activity can destabilize interfaces in ways reminiscent of classical instabilities, yet the mechanisms are not well understood [15, 16, 17]. Through computational simulations, we examine how non-equilibrium driving redefines interfacial rupture dynamics in active mixtures. By linking microscale activity to macroscale stability, this work advances our understanding of segregation processes in biological and synthetic systems.

The significance of this study extends beyond theoretical advances non-equilibrium systems, offering potential applications in emergent technologies. By characterizing how activity governs interfacial stability, we identify key parameters, such as system aspect ratio, particle flux and density, that control pattern formation in binary active mixtures. Such control, which dictates the system's response to surface perturbations, is critical for applications like targeted drug delivery, adaptive materials, and synthetic active particles [18, 19, 20]. Furthermore, our computational framework provides strategies to suppress or harness instabilities in active microfluidics, enabling precise manipulation of colloidal flows [21]. By bridging hydrodynamics concepts with active matter physics, this work not only advances our understanding of non-equilibrium phenomena but also offers practical strategies to regulate instability thresholds. The following chapters expand on these themes, beginning with a review of active systems classification to contextualize our work into instability mechanisms framework.

1.1 Active Matter: Non-Equilibrium Physics at the Mesoscale

Active matter represents systems where individual components transduce energy, often from chemical, optical, or thermal sources into mechanical work, displaying non-equilibrium dynamics [7, 22]. This localized energy input drives pattern formation that are absent in passive systems, such as spontaneous flows and density oscillations. As illustrated in Fig. 1, active systems span diverse scales: biomolecular motors uses ATP to generate force, bacterial colonies exploit chemical gradients for propulsion [23, 24, 25], and synthetic agents like Janus particles exhibit programmable motion via self-phoresis [12]. At macroscopic scales, alignment interactions in bird flocks or fish schools yield emergent directional order [26, 27]. Despite their diversity, these systems share a unifying feature: their constituents are self-propelled agents, whose motion arises from internal energy-consuming mechanisms (e.g., metabolism, catalytic reactions).

The behavior of active matter is governed by the competition between stochastic forces and the energy driving self-propulsion. Randomness in these systems arise from thermal fluctuations, self-propulsion energy, or their interplay, depending on the system's scale. These factors set the energy scale of stochastic forces, and consequently dictate macroscopic properties like collective motion and phase separation [28]. For instance, the diffusion coefficient quantifies particle spreading due to random motion, while the persistence time measures how long a particle maintains direction before stochastic forces randomize its trajectory [29]. Quantifying these properties is critical not only to identify deviations from equilibrium but also to construct

Figura 1 – **Active Matter Across Length Scales.** Examples of active agents span a wide range of sizes, from nanometers to meters. Shown here (left to right) are: biomolecular motors, bacteria, sperm cells, synthetic Janus particles, zebrafish embryos, robotic swarms, and animals that exhibit collective behaviors such as flocking and herding.

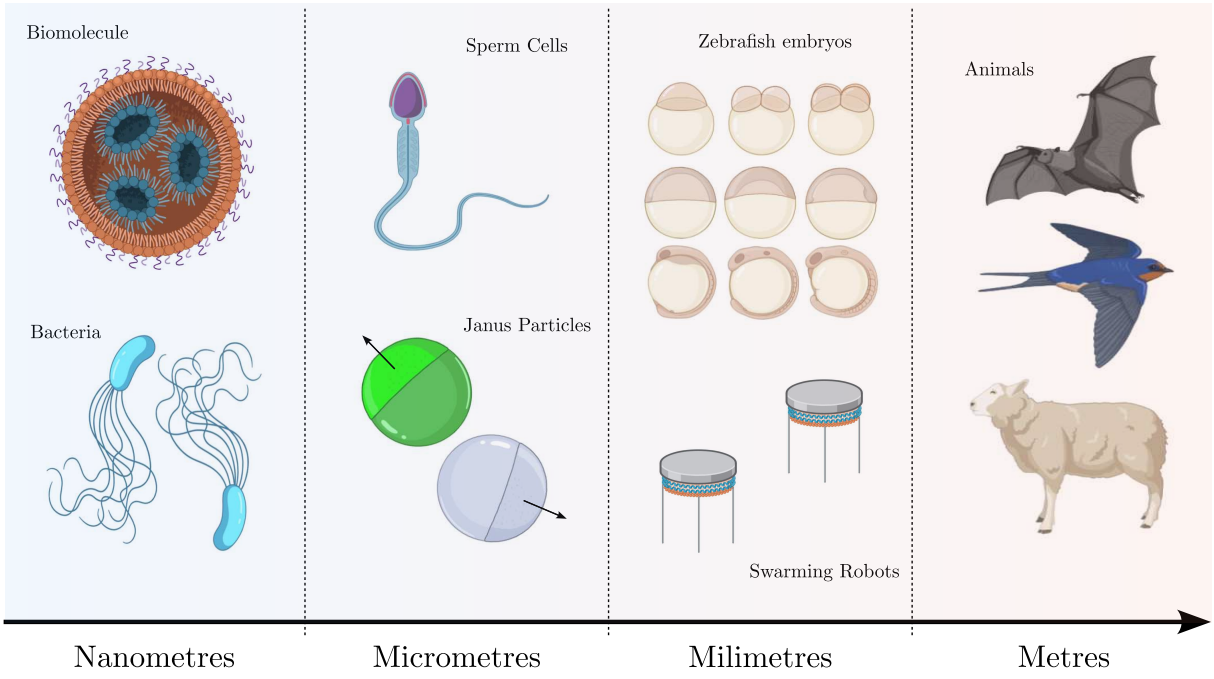

Source: Autor.

predictive active matter models. Such deviations challenge equilibrium statistical mechanics: fundamental principles like the fluctuation-dissipation theorem, often fail in active matter. For example, in living cells, this breakdown can be used to quantify forces generated by active processes such as intracellular transport [30, 31]. These violations highlight the need for new theoretical frameworks to describe these non-equilibrium systems.

Various theoretical frameworks have emerged to model active matter [32]. One strategy extends equilibrium thermodynamics by defining effective steady states under specific conditions, such as weak activity, where systems approximate equilibrium-like behavior [33, 34]. Another approach generalizes familiar concepts from passive systems: for example, “active pressure” incorporates self-propulsion forces [35, 36], while “negative surface tension” captures interface perturbations driven by energy injection [37, 38]. However, these efforts face significant challenges in extending such concepts to broader classes of active matter. Addressing these limitations requires novel theoretical frameworks that go beyond traditional statistical mechanics, offering insights into universal principles governing far-from-equilibrium systems.

Overcoming these challenges requires a deeper understanding of how energy dissipation and local interactions govern emergent behaviors in active matter. Stochastic thermodyna-

mics provides a powerful framework for this purpose, extending classical thermodynamics to account for microscale fluctuations and irreversibility [39]. By quantifying entropy production rates, a measure of broken time-reversal symmetry, this approach reveals how active systems sustain non-equilibrium states and how these states influence collective dynamics [40, 32]. However, despite progress, a unified framework for active matter remains elusive due to the diversity of stochastic interactions.

To bridge this gap, organizing active systems by their symmetry properties offers a promising perspective. For instance, distinguishing polar (directional) from nematic (headless/-tailless) order in individual agents provides a categorization that aligns with distinct universality classes [41]. This classification organizes active matter into categories with shared theoretical foundations, enabling experimental insights and facilitating computational modeling. In the next section, we outline key models within this framework, setting the stage for our investigation of active mixtures.

1.2 Classification of active systems: Symmetries

Theoretical frameworks for active matter are fundamentally defined by the symmetries of both the constituent particles and their interactions [42]. For elongated, rod-like agents, orientational order arises from alignment forces parallel to the particle's long axis. These systems exhibit two distinct symmetry classes: (i) polar (vectorial) order, where particles develop a collective preferred direction of motion [10]. This symmetry is captured by hydrodynamic theories like the Toner-Tu equations [43, 44], and (ii) nematic (apolar) order, where particles align head-to-tail but lack net directional motion [45]. This symmetry-based classification organizes active systems into universality classes while dictating their emergent dynamics.

For particles symmetric under rotation, isotropic spheres, the absence of alignment interactions results in isotropic activity, where motion lacks a defined directionality. These systems, called scalar active particles, exhibit emergent phenomena driven solely by density-dependent motility, a scalar field [46]. Beyond systems with intrinsic self-propulsion, activity can emerge in passive mixtures through high contrast in components diffusivity. Activity, often quantified as an effective temperature imbalance, drives non-equilibrium phase segregation [33, 47, 4]. With this framework, we now examine each category in more detail:

Polar active matter

Polar active particles are self-propelled, elongated agents with head-tail asymmetry, giving them a preferred direction of motion, as shown in Fig. 2b). This intrinsic polarity drives collective alignment, producing ferromagnetic-like states with macroscopic directed flow [41]. A paradigmatic example is the Vicsek model [10], where particles align their velocities to the average direction of neighbors within a fixed radius, subject to noise. Reducing noise or increasing density triggers a phase transition from disordered motion to long-range polar order, forming coherent flocks or swarms.

Figura 2 – **Polar Symmetry in Active Matter.** a) Polar vibrated granular rods (from [1]) b) A polar active particle with self-propulsion speed v_0. c) Representation of the vectorial order parameter P (arrows).

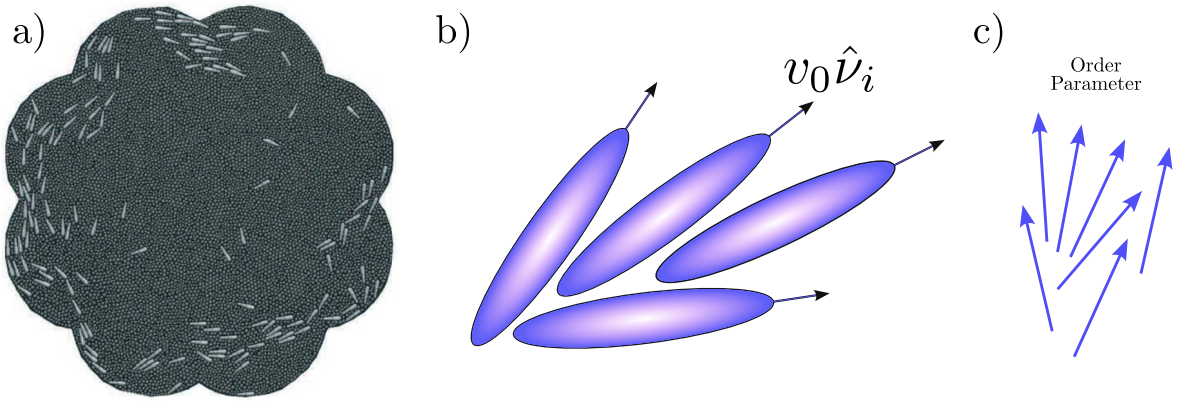

Source: Autor.

Polar order spans biological and synthetic systems: for example, in biological systems, migrating bird flocks [26] and bacterial swarms [48] align via social interactions, while in synthetic systems, vibrated granular rods achieve polar order through inelastic collisions and substrate energy injection as in Fig. 2a). Polar systems are described by the Toner-Tu equations, which extend Navier-Stokes theory to include active stresses and density-dependent motility. These equations predict propagating density waves and giant number fluctuations.

Active nematics

Active nematics describe elongated, rod-like particles with head-tail symmetry, resulting in orientational order without net directional motion. Like their equilibrium counterparts (nematic liquid crystals [49]), these systems exhibit long-range alignment of particle axes, but

energy transduction at the microscale drives chaotic dynamics absent in passive systems. This interplay between nematic order and activity produces self-sustained spatiotemporal patterns [41].

Figura 3 – **Nematic Symmetry in Active Matter.** a) Nematic ordering in microtubule-kinesin mixtures at a water-oil interface, driven by motor-protein activity [2]. b) Apolar active particles exerting force dipoles along their orientation. c) Representation of the tensor order parameter Q.

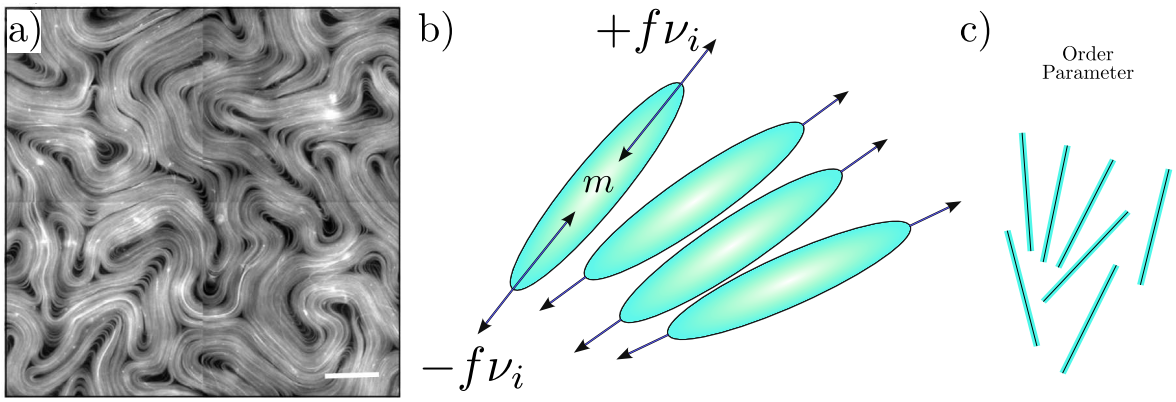

Source: Autor.

A theoretical framework for active nematics arises from active nematohydrodynamics, which extends liquid crystal theory to include active stresses [50]. These systems presents intriguing phenomena, such as the emergence of topological defects [51] and turbulent-like flows, known as active turbulence [52]. Examples include biological systems like microtubule-kinesin mixtures [53] as showed in Fig. 3a), and synthetic systems like vertical vibrated granular rods [54].

Scalar active matter

Scalar active matter represents spherical particles lacking alignment interactions, resulting in isotropic motion with no preferred direction. Despite this simplicity, these particles exhibit a variety of non-equilibrium dynamics driven by self-propulsion and density fluctuations [46]. Their behavior is governed by a single scalar field, the particle density, making them a minimal framework to study activity-driven behavior [55, 42].

One of the most well-known models for describing scalar active matter is the Active Brownian Particles (ABP) framework. Here, particles present translational diffusion (as in traditional Brownian motion) and rotational diffusion, which randomizes their self-propulsion direction over a characteristic persistent time. This minimal model neglects hydrodynamic and

phoretic interactions, focusing instead on the interplay between particle motility and repulsive interactions [56]. Remarkably, even without attractive forces, ABPs undergoes motility-induced phase separation (MIPS), as shown in Fig. 4a), where dense liquid-like phases coexist with dilute gas-like regions [3, 13].

Figura 4 – **Scalar Symmetry in Active Matter.** a) Motility-induced phase separation (MIPS) in a simulation of self-propelled disks [3]. b) Schematic of scalar active particles with isotropic motion (no alignment). c) Scalar order parameter defined as the density difference between the liquid phase (ρ_L) and the gaseous phase (ρ_G).

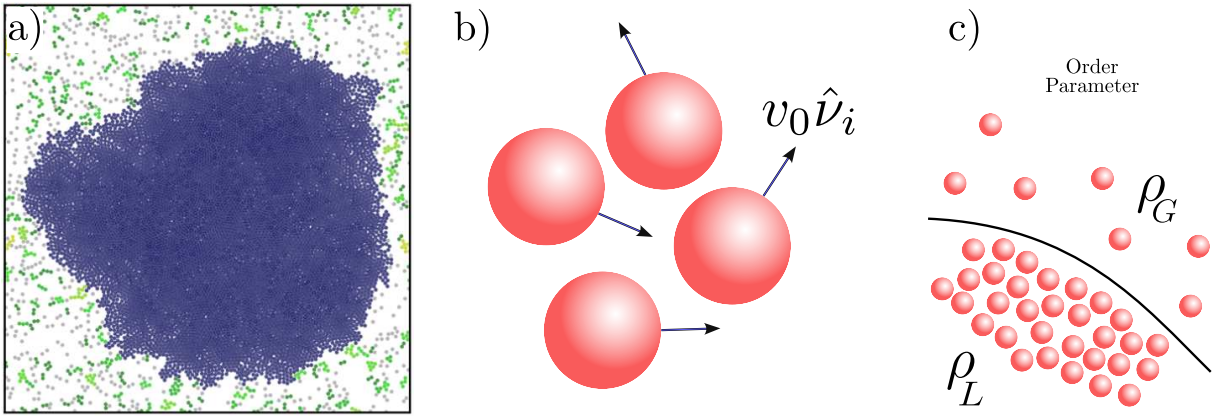

Source: Autor.

Active diffusive mixtures

There are examples of systems where activity does not stem from self-propulsion but instead arises from differential diffusivity between passive components. These systems are the central focus of this thesis, and for simplicity, we will refer to them as active diffusive mixtures. In these systems, activity is a scalar quantity and emerges from the non-equilibrium coupling of species with large diffusivity imbalances. This model was independently proposed by two groups: one approached it analytically, considering particles coupled to different thermostats [33], while the other explored it computationally, simulating phase separation in mixtures with significant diffusivity contrast [4]. In such systems, one species remains out of equilibrium with the thermal bath, creating a pronounced diffusivity gap. Although the individual components are passive, their interaction under this gradient mimics active matter by driving sustained energy dissipation and emergent order.

This diffusivity imbalance gives rise to phenomena that are absent in equilibrium systems. A notable example is phase separation via nucleation: low-diffusivity (“cold”) particles

coalesce into dense droplets, while high-diffusivity (“hot”) particles form a surrounding gas-like phase, Fig. 5. As the droplets of cold particles grow in size, the high diffusion of hot particles induces depletion-like forces, ultimately leading to the formation of a single dominant cluster of cold particles in low-density systems. This mechanism destabilizes the homogeneous mixed state, driving the system toward phase-segregated configurations. Unlike equilibrium phase separation, which typically requires attractive interactions, this liquid-gas transition occurs without any explicit attraction between particles. Such instabilities exemplify how activity, even without alignment or propulsion, can reconfigure matter far from equilibrium.

Figura 5 – **Active Mixtures.** a) Demixing in a binary mixtures of particles with differential diffusivity [4]. b) Schematic representation of the binary components, the shadow around the particles represents the magnitude of the diffusion coefficients, being the red (“hot”) particle the more diffusive. c) Representation of the interaction between the two species at the interface of separation.

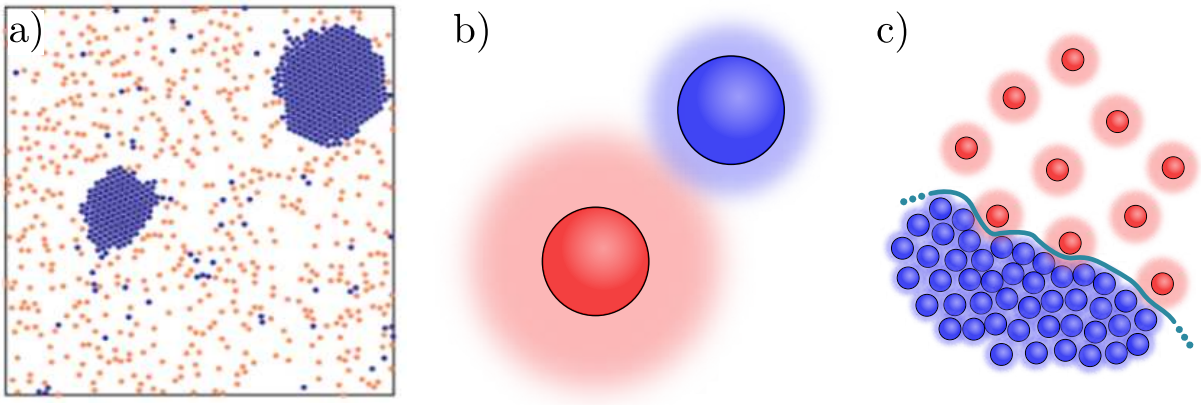

Source: Autor.

Although early models of activity driven by differential diffusivity focused primarily on systems of spherical particles, the idea of representing activity-induced fluctuations as interactions at an “effective” temperature first emerged in the context of chromosome segregation within the cell nucleus [47]. In that model, the nucleus is treated as a confining spherical shell densely packed with linear polymer chains consisting of active and inactive monomers. This approach inspired further computational studies on binary mixtures of polymers with differing diffusivities. These studies showed that the diffusivity contrast required to induce phase segregation is substantially lower for polymers than for spherical particles [57]. Moreover, the required gradient decreases even further as the polymer chains become longer.

Most theoretical advances within this framework remain limited to dilute systems,

where analytical solutions for emergent effective quantities, such as interfacial pressure and surface tension at the interface, are tractable [15, 58]. These results are derived by integrating the multiparticle Fokker-Planck equation under the assumption of weak interactions. However, the omission of higher-order corrections, such as three-body interactions and correlation effects, restricts the model's predictive power in describing behaviors at intermediate and high densities. For instance, the theory fails to capture density-dependent suppression of demixing, a phenomenon observed in crowded environments and highly relevant for describing biological processes such as cell sorting [59].

Experimental evidence for non-persistent active behavior has been observed in a variety of systems. For instance, enzymes exhibit activity-driven diffusion enhancement in the presence of their reactants [60]. Similar behavior has been reported in other systems involving local chemical transformations, such as chromatin methylation or acetylation [33]. Additionally, chemically reactive mixtures have been shown to sustain non-equilibrium phase separation [61]. These examples highlight the broad applicability of active mixtures, characterized by isotropic but energy-consuming processes, to both biological systems and synthetic materials.

Despite being one of the simplest systems of active matter physics, where activity emerges as a result of the high diffusivity contrast between passive components, it exhibits rich dynamical behaviors and intriguing collective phenomena. This system provides a versatile framework for studying a wide range of physical properties and processes, including surface dynamics and surface tension [62], transport properties [58], correlated motions in motorized genomes [63], liquid-crystalline phases [64], long-time diffusion enhancement [65], and entropy production [66], among others.

As the central focus of this thesis, we investigate how the interplay between differential diffusivity and particle interactions determines the nature of non-equilibrium fluctuations at the interface formed during phase separation. To analyze the time evolution of these fluctuations and their characteristic length scales, we adapt the geometry of the Plateau-Rayleigh instability in passive fluids [14] to a two-dimensional configuration within the context of active diffusive mixtures. Subsequent chapters explore how this interplay gives rise to complex pattern formation, including:

1. Unstable configurations with no equilibrium analog, such as 2D channel instabilities under varying conditions.
2. The rupture dynamics governing these instabilities, including their scaling properties.

3. Emergent effective surface tension, a non-equilibrium analog of interfacial energy that influences pattern stability.

By understanding these dynamics, this work advances our understanding of non-equilibrium self-organization, with implications for rupture processes and potential applications in biological systems.

1.3 Emergent collective behavior

A characteristic feature of active matter is its ability to undergo self-organized phase separation, a process in which systems spontaneously segregate into dense and dilute phases without the need for external fields or attractive interactions. This phenomenon arises through distinct mechanisms, depending on the interplay among activity, particle interactions and symmetry. One of the most paradigmatic examples is MIPS, commonly observed in scalar active systems. As introduced in Sec.1.2, MIPS occurs when particle motility decreases as a result of local density fluctuations. Despite all particles having identical intrinsic properties, the system separate into a dense (liquid-like) phase and a dilute (gas-like) phase as shown in Fig. 4a) [13, 67].

These non-equilibrium phases display unique dynamical features that distinguish them from their equilibrium counterparts. Examples include propagating interfaces driven by particle flux imbalances [68], self-similar cluster growth [69], and surface phenomena characterized by novel properties such as surface growth [70], kinetic roughening [71] and interface height fluctuations [72].

Beyond characterizing MIPS, this phenomenon has motivated extensive research aimed at redefining classical thermodynamic concepts—such as pressure and surface tension—for non-equilibrium systems [73]. Recent studies have incorporated the activity-driven interfacial stresses into these definitions [37], yet there remains no consensus on how to measure or interpret these emergent quantities. For example, pressure-tensor methods predict negative interfacial tensions in ABPs at steady-state [38], challenging the traditional equilibrium notion of surface tension. Such discrepancies highlight the need for universal definitions of emergent quantities in active matter.

The insights gained from studying surface dynamics in ABPs have inspired methodological advances applicable to broader non-equilibrium systems, such as phase separation in active diffusive mixtures. By adapting techniques originally developed for ABPs, such as pres-

sure tensor analysis and interface fluctuations studies [38], researches have extended concepts like effective surface tension and scaling laws to systems with differential diffusivity [33, 74, 75] including the case of polymer segregation [62]. These frameworks now enable quantitative descriptions of interfacial properties in active diffusive mixtures; however, their analytical applicability remains limited to dilute regimes.

The self-organized dynamics of phase separation in active diffusive mixtures depend strongly on the system's density (packing fraction) [59]. As described in Sec. 1.2, at low densities, the system reaches a steady state characterized by a single cluster of cold particles surrounded by hot particles, as shown in Fig. 5. This configuration resembles equilibrium phase separation, where surface tension minimizes interfacial contact between phases. At intermediate densities in square domains, however, the system exhibits counterintuitive behavior: cold particles form a channel structure enveloped by hot particles, suggesting that the circular geometry does not represent a dominant configuration under these conditions. This finding becomes even more intriguing in rectangular domains, where the channel often aligns with the longer axis, as illustrated in Fig. 6. These results highlight how geometry and non-equilibrium dynamics interact to dictate emergent order.

Figura 6 – **Demixing in active mixtures at intermediate densities.** Time evolution of the demixing process in a binary mixture of particles with differential diffusivity at intermediate densities (packing fraction $\phi = 0.72$) in a rectangular domain. The initial uniformly distributed configuration is unstable and evolves into a steady-state configuration characterized by a channel of cold particles surrounded by hot particles. The yellow lines in the final stage highlight the phase separation between the two components of the mixture.

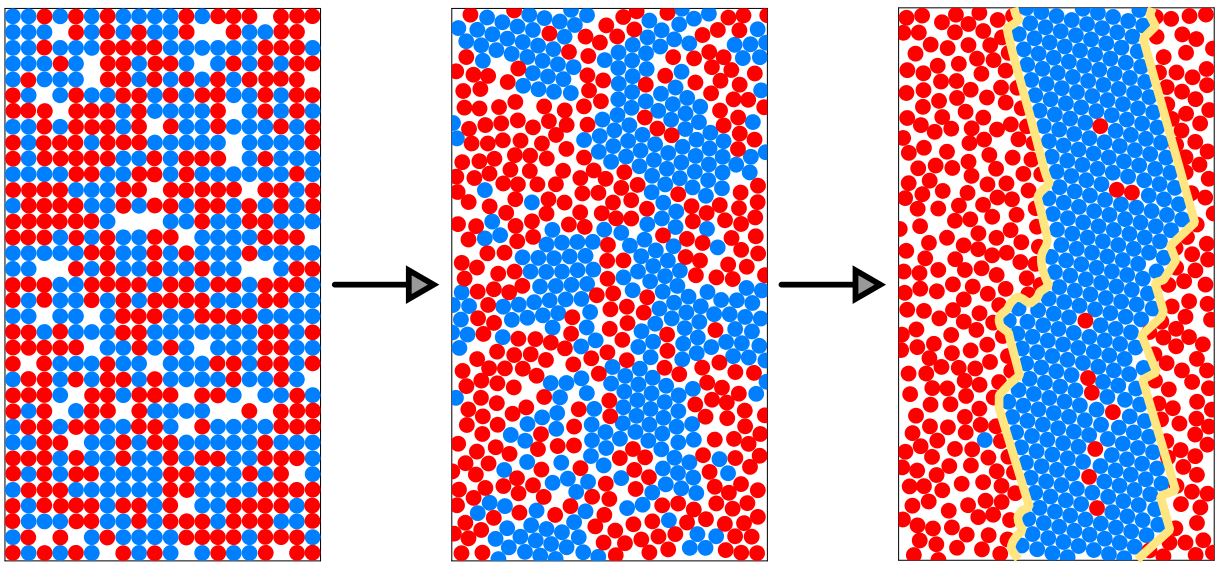

Source: Autor.

In the final state depicted in Fig. 6, the two yellow lines represent stable interfaces. Despite perturbations induced by the hot particles, these interfaces remain stationary, suggesting the presence of an effective surface tension that balances the non-equilibrium stresses arising from interactions with the hot particles. This behavior cannot be explained by existing analytical frameworks [15], which are restricted to dilute regimes. Another key finding beyond current theoretical predictions is the suppression of phase separation at high packing fractions, where insufficient free space prevents diffusivity contrasts from driving segregation. These results are supported by computations of entropy production [59].

As mentioned above, there are several methods to determine the effective surface tension at stationary interfaces. One approach is the pressure tensor method, which identifies anisotropies in the vertical and horizontal components of the interface. Another is capillary wave theory, which relates the energy required to deform a flat interface to its fluctuations [76, 72]. By analyzing the work needed to deform an interface through height fluctuations, this method leads to a quadratic effective Hamiltonian in Fourier space, where $\langle |h(k)|^2 \rangle$, is related to the effective surface tension. In equilibrium, interfacial fluctuations follow the scaling law $\langle |h(k)|^2 \rangle \sim 1/k^2$. Deviations from this behavior indicate violations of the fluctuation-dissipation theorem, a characteristic of non-equilibrium dynamics [77]. These results and their implications for active diffusive mixtures will be explored in depth in Chapter 2.

Studying emergent phenomena such as phase separation and the corresponding interfacial dynamics is essential for advancing both theoretical frameworks and computational models of non-equilibrium physics [78, 71]. Theoretically, these phenomena challenge the foundations of equilibrium statistical mechanics, revealing how collective behaviors emerge from individual particle interactions that violate detailed balance. The redefinition of classical concepts, in active systems opens new avenues for understanding biological processes [62, 79]. By linking microscale activity to macroscopic stability in two-dimensional configurations, this work contributes to the characterization of effective interactions in active matter.

1.4 Instabilities and pattern formation

Instabilities are fundamental to understanding a wide range of phenomena in soft matter physics, from equilibrium phase transitions to active self-organization [55]. In passive systems, steady-state configurations result from a balance of competing forces, such as elastic, viscous, and interfacial forces that collectively minimize the system's free energy. When external

perturbations are introduced, this balance can be disrupted, potentially driving the system toward a new equilibrium state. Such transitions occur when a control parameter—which determines the system's response to external perturbations—exceeds a critical threshold. Beyond this point, the system becomes unstable: perturbations with wavelengths $\lambda > \lambda_c$ (the critical wavelength) grow exponentially, while shorter-wavelength modes $\lambda < \lambda_c$ decay over time. This wavelength selectivity, characteristic of instabilities like the Plateau-Rayleigh breakup of liquid jets [80], leads to pattern formation governed by the interplay of geometry and fluctuations. In active systems, similar instabilities emerge from energy input at the microscale, often leading to qualitatively new behaviors [81]. While the underlying mechanisms differ from those in passive systems, both cases display wavelength-selective growth of perturbations, suggesting that certain mathematical features remain robust across equilibrium and non-equilibrium regimes.

The exponential growth of perturbation amplitudes often leads to abrupt transitions, driving the system toward distinct spatial or temporal patterns, such as stripes [82], vortices [83], or oscillatory waves [84]. These emergent patterns reflect the nature of the underlying instability, which may arise from external driving, competing interactions, or gradients in activity. As the instability develops, the system evolves toward a new configuration characterized by a dynamic balance of forces. Analyzing these transitions provides key insights into the mechanical and dynamical principles governing soft matter systems. Given the ubiquity of instabilities in natural processes [85, 86] and their relevance to material science applications [87, 88], developing methods to predict and control them has become a central challenge [89]. Beyond practical applications, such studies also improve our understanding of pattern formation and emergent behavior in complex systems.

Classical Examples of Instabilities in Passive Systems

Two well-known examples of instabilities in classical fluids are Rayleigh-Bénard convection, Fig. 7, and the Plateau-Rayleigh instability (PRI), Fig. 8. These phenomena exemplify how competing forces can destabilize a system and drive to the emergence of spatial patterns in passive fluids. Although both originate from perturbations to equilibrium states, their underlying mechanisms differ fundamentally. Rayleigh-Bénard convection is driven by external thermal gradients resulting in the formation of convection rolls. In contrast, the Plateau-Rayleigh instability arises from interfacial tension, which drives the breakup of cylindrical fluid jets to minimize surface area and reduce interfacial energy. These classical cases illustrate how

instabilities can emerge from either external driving forces (as in Rayleigh-Bénard) or intrinsic thermodynamic reasons (as in PRI).

Rayleigh-Bénard convection arises in a horizontal fluid layer confined between two thermally conducting, parallel plates. When the temperature difference ΔT between the plates exceeds a critical threshold ΔT_c, buoyancy forces overcome viscous damping and thermal diffusion, causing the fluid to become unstable. This instability leads to the formation of convection cells, Fig. 7, with a characteristic wavelength determined by the balance between thermal gradients, viscosity, and gravity. Rayleigh-Bénard convection stands as a canonical example of how external energy input, such as heat, can drive the spontaneous emergence of complex, self-organized structures [90].

Figura 7 – **Rayleigh-Bénard convection** Schematic illustrating the formation of convective cells in a fluid layer subjected to a temperature gradient, driven by buoyancy forces. As the lower surface is heated and the upper surface is cooled, the system undergoes instability, leading to the spontaneous emergence of regular, periodic flow structures.

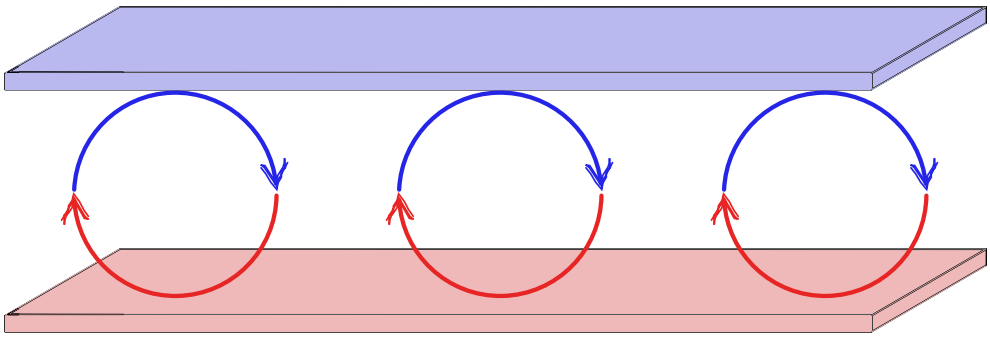

Source: Autor.

Plateau-Rayleigh instability, in contrast, governs the breakup of liquid columns into droplets, due to the amplification of perturbations caused by surface tension. Specifically, perturbations with wavelengths $\lambda > 2\pi r$ (where r is the column radius) grow exponentially as surface tension minimizes interfacial energy by reducing surface area (Fig. 8). This instability provides a foundational understanding of how fluids respond to perturbations [91] and helps identify the key variables governing rupture dynamics of free-surface flows [92, 93]. Precise control over these parameters enables the manipulation of factors like breakup time and droplet size, which are critical in technologies and applications that depend on micro-scale fluid behavior [94, 95].

These two phenomena demonstrate how pattern formation emerges from force imbalances, where the wavelengths of perturbation dictates the resulting structures. Although

Figura 8 – **Plateau-Rayleigh instability** Schematic illustrating the formation of perturbations with wavelength λ along the surface of a cylinder of radius R, driven by surface tension. As the perturbations grow, the cylinder becomes unstable and may eventually break up into droplets.

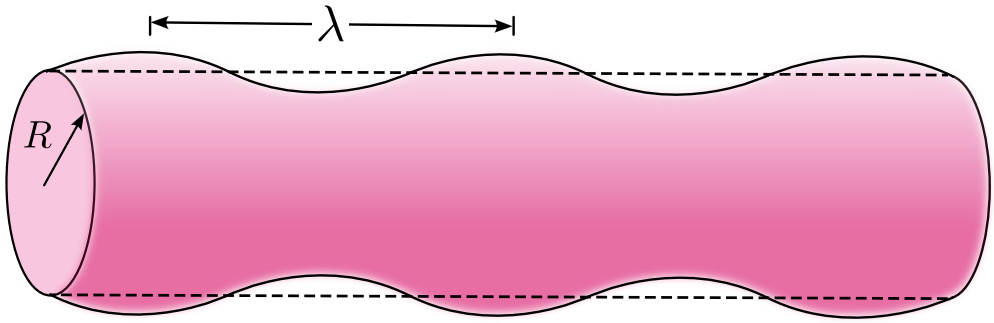

Source: Autor.

these and other instabilities, such as Rayleigh–Taylor [96], Saffman–Taylor [97], and Kelvin–Helmholtz [98], are well studied within fluid dynamics, they are not exclusive to fluids. Similar behaviors are observed in granular matter and passive colloids [99, 100], drawing a connection to discrete models of active matter and motivating the exploration of such instabilities within active diffusive mixtures. In active matter, however, the treatment of instabilities becomes more complex. Unlike passive systems, effective non-equilibrium quantities, such as active-pressure and surface tension, are not well-defined thermodynamic variables. Moreover, active systems operate far from equilibrium, where transitions between states cannot be explained by free energy minimization. Instead, stability depends on a dynamic balance between activity and dissipation, requiring new theoretical approaches to quantify perturbations and predict pattern formation.

Instabilities in Active Matter

Many instabilities observed in passive systems have been extended into the non-equilibrium domain of active matter, often exhibiting analogous behaviors governed by similar mathematical frameworks [101]. These extensions reveal how the presence of self-propelled micro-swimmers can fundamentally alter fluid properties and drive new forms of collective dynamics, introducing additional degrees of freedom such as self-propulsion, non-equilibrium interactions, and in some cases, effective surface tension-like behaviors even in the absence of attractive forces [15]. Moreover, activity gives rise to entirely novel classes of instabilities with no passive counterpart. Examples include the two-dimensional channel instability observed in

chiral active fluids [102] and the system explored in this thesis.

Beyond the practical interest in controlling instabilities, a central motivation of this thesis is to characterize and understand a new two-dimensional instability unique to non-equilibrium systems: the rupture of channel-like configurations in segregated systems with differential diffusivity. In contrast to passive fluids, where such two-dimensional geometries are generally stable, active channels destabilize under non-equilibrium driving forces, as demonstrated experimentally in chiral active fluids and computationally in driven liquids and active mixtures [102, 72].

This instability is fundamentally distinct from classical analogs like the Plateau-Rayleigh instability, despite visual similarities in the emergent patterns. While PRI minimizes interfacial energy in three-dimensional systems, it cannot manifest in two-dimensional geometries due to dimensionality constraints [103]. In contrast, the active channel rupture observed here arises from the interplay between activity-driven forces and repulsive interactions, generating emergent effective surface forces that mimic equilibrium-like droplet formation through purely non-equilibrium mechanisms.

To explain this instability and quantify its rupture dynamics, we develop both an analytical and computational framework. The next chapter introduces essential concepts from stochastic dynamics, including the Langevin and Fokker-Planck equations, which form the foundation for modeling active matter systems. By connecting theoretical predictions with simulation results, we extract the parameters governing rupture dynamics and identify universal features of active interfaces.

2 STOCHASTIC PHENOMENA IN ACTIVE MIXTURES

Active matter systems are inherently stochastic, driven by thermal noise, self-propulsion fluctuations, and energy transduction at the microscale. Their dynamics are governed by particle symmetries, interaction forces, and activity types. These properties determine how stochasticity manifests in collective phenomena like instabilities or phase separation. Building on insights from Chapter 1, this chapter explores analytical and computational frameworks to model the dynamics of active mixtures, with a focus on instabilities driven by emergent surface tension-like forces (non-equilibrium interfacial stresses).

The first part of the chapter introduces theoretical concepts for modeling stochastic processes, emphasizing spherical active particles. We begin with Brownian motion, the prototypical stochastic process in passive systems, and then extend to the Langevin equation, a stochastic differential equation that incorporates deterministic forces and random noise. This framework establishes the foundation for constructing coupled systems of stochastic differential equations used in simulations. We then derive the Fokker-Planck equation, which describes the time evolution of the probability density for particle positions and velocities. While the Langevin equation tracks individual trajectories, the Fokker-Planck equation provides insights into the system's behavior at the ensemble level, making it particularly useful for describing low-density active mixtures [33].

The latter part of the chapter applies these theoretical tools to computationally simulate stochastic systems. First, we construct an ensemble of particles with differential diffusivity, modeling their interactions via short-range repulsive potentials. We then introduce percolation techniques to analyze rupture dynamics. The Newman-Ziff algorithm [104] is employed to identify the wrapping condition of the "cold" particles cluster, quantifying the breakup time, t_b, when the channel fractures. Finally, we adapt capillary wave theory (CWT) to study active interfaces, using Fourier analysis to decompose height fluctuations $h(\mathbf{x},t)$ into spectral modes. By analyzing the fluctuation spectrum, we extract the scaling exponent and quantify emergent effective surface tension.

Different types of random noise, such as thermal, active, or chiral, define distinct classes of active matter systems, ranging from Brownian particles to self-propelled or spinning agents. Each type of noise generates unique emergent forces and behaviors, including MIPS, flocking, and demixing driven by differential diffusivity. In these systems, activity acts as a local stochastic property that, when combined with deterministic interactions, drives collective

dynamics beyond the scope of equilibrium thermodynamics. To study these phenomena, we model the system using stochastic processes, which describe how random variables evolve over time. We begin with the classical Brownian particle and systematically build toward more complex active matter systems, incorporating particle interactions and diffusivity contrasts to reveal how microscopic noise gives rise to macroscopic patterns.

2.1 Brownian dynamics and the Langevin Equation

When considering stochastic processes in physics, one of the first examples that comes to mind is the trajectory of a Brownian particle—a microscopic particle suspended in a fluid, subjected to coarse-grained interactions with surrounding molecules. These interactions manifest as two complementary forces: (i) a drag force proportional to the particle's velocity, opposing its motion, and (ii) random impulses arising from molecular collisions due to thermal fluctuations. The interplay between these forces produces the particle's characteristic random trajectory, known as Brownian motion. Mathematically, this behavior is described by [55]:

$$m\frac{d\mathbf{v}}{dt} = \mathbf{F}_{\text{drag}} + \mathbf{F}_{\text{collisions}}, \tag{2.1}$$

where m is the particle's mass and $\mathbf{v}$ its velocity.

The forces governing Brownian dynamics are determined by the fluid's properties. For example, in the low Reynolds number regime (where viscous forces dominate inertia), Stokes' law dictates the drag force on a spherical particle as linearly proportional to its velocity. In this regime, the fluid's damping force takes the form $\mathbf{F}_{\text{drag}} = -\gamma\mathbf{v}$, where γ is the damping coefficient. For spherical particles, $\gamma = 6\pi\eta a$, whit η the dynamic viscosity of the fluid and a is the particle's radius [55].

Defining the collision force $\mathbf{F}_{\text{collisions}}$ explicitly is challenging, as a deterministic approach would require precise knowledge of the fluid's molecular configuration and solving the equations of motion for every collision, a task computationally intractable and physically impractical due to the immense number of interactions. Instead, we adopt a statistical ensemble approach: by considering many non-interacting particles in the fluid (dilute limit), we model molecular collisions as a stochastic process averaged over the ensemble. This allows us to represent the collision force as a random variable $\xi(t)$, leading to the Langevin equation:

$$m\frac{d\mathbf{v}}{dt} = -\gamma\mathbf{v} + \xi(t). \tag{2.2}$$

The Langevin equation is a type of stochastic differential equation, where one or more terms—typically forces—are modeled as random functions of time with well-defined statistical properties [105]. The stochastic force $\xi(t)$ must satisfy two essential conditions:

1. Zero Mean

The ensemble average of the noise vanishes at all times:

$$\langle \xi(t) \rangle = 0, \tag{2.3}$$

reflecting the absence of a preferred direction for molecular collisions. This ensures no net drift in the particle's motion over time.

2. Delta Correlation

Collisions at different times are statistically independent, enforcing:

$$\langle \xi(t)\xi(t') \rangle = 2\gamma k_B T \delta(t-t'), \tag{2.4}$$

where γ is the Stokes coefficient, k_B is the Boltzmann's constant, and T the fluid temperature. The Dirac delta $\delta(t-t')$ ensures that the noise has no memory, while the factor $2\gamma k_B T$ enforces the fluctuation-dissipation theorem, balancing energy injection (noise) and dissipation (drag). Together with the linear damping $(-\gamma \mathbf{v})$, these conditions define a Langevin force.

This formulation provides a simplified yet powerful framework for studying Brownian dynamics [106]. The Langevin equation governs the time evolution of the particle's velocity $\mathbf{v}(t)$, given the initial condition $\mathbf{v}_0 = \mathbf{v}(t=0)$. By integrating Eq. 2.2 and applying the noise properties (Eq. 2.3 and Eq. 2.4), we derive key statistical properties of the particle's motion, such as velocity fluctuations and mean squared displacement (MSD), arising from thermal interactions with the fluid (at equilibrium temperature T).

In the long-time limit ($t >> \gamma^{-1}$), the system reaches equilibrium, and the mean square fluctuations exhibit two key behaviors:

$$\langle \Delta \mathrm{v}^2(t) \rangle = \frac{k_B T}{m}, \tag{2.5}$$

$$\langle \Delta \mathrm{x}^2(t) \rangle = \frac{2k_B T}{\gamma} t. \tag{2.6}$$

The velocity fluctuations given by Eq. 2.5 reflects the equipartition theorem, where thermal energy k_BT partitions equally into each degree of freedom. Meanwhile, the mean square displacement given by Eq. 2.6 grows linearly with time, expressing the essence of diffusive motion. The proportionality constant is the Einstein relation:

$$D = \frac{k_BT}{\gamma} = \frac{k_BT}{6\pi\eta a}, \tag{2.7}$$

which links the diffusion coefficient D to the fluid's viscosity η, particle radius a and temperature T. This relation directly connects microscopic stochastic forces to macroscopic transport, exemplifying the fluctuation-dissipation theorem's role in equilibrium systems [55].

2.2 The Fokker-Planck Equation

The Fokker-Planck equation provides a complementary framework to the Langevin formalism for analyzing stochastic processes. Instead of tracking individual trajectories through stochastic differential equations, it describes the time evolution of the probability density $\mathscr{P}(\mathbf{x},\mathbf{v},t)$ in phase space, where each point $(\mathbf{x},\mathbf{v})$ corresponds to a possible state of the system. This approach change the perspective from single-particle dynamics to the statistical behavior of ensembles, making it particularly powerful for systems where emergent phenomena depend on collective averages rather than specific realizations.

Mathematically, the Fokker-Planck equation is a partial differential equation governing the evolution of the probability density $\mathscr{P}(\mathbf{x},\mathbf{v},t)$ under deterministic drift and stochastic diffusion. For systems described by the Langevin dynamics, it arises naturally when averaging over noise realizations, bridging microscopic stochastic trajectories to macroscopic observables such as probability currents and stationary distributions [106]. In active matter, a key advantage of this framework lies in its ability to identify non-equilibrium steady states: by analyzing non-zero probability fluxes in phase space, one can quantify the degree of detailed balance violation, distinguishing equilibrium-like behavior from intrinsically non-equilibrium dynamics [107, 108]. These insights are critical for understanding how energy dissipation and activity sustain order in systems like active diffusive mixtures.

Connecting Langevin and Fokker-Planck Formalisms

The Langevin equation specifies the first two statistical moments of the stochastic process $\xi(t)$, the mean and variance. For Gaussian white noise, all higher-order cumulants

vanish, meaning these moments fully characterize the noise. This reduces its description to a single parameter: the noise strength in Eq. 2.4. The general Langevin equation for a stochastic variable $\mathrm{X}(t)$ is:

$$\frac{d\mathrm{X}}{dt} = f(\mathrm{X}) + g(\mathrm{X})\xi(t), \tag{2.8}$$

where $f(\mathrm{X})$ is the deterministic drift, $g(\mathrm{X})$ scales the noise amplitude, and $\xi(t)$ is Gaussian white noise [105]. Under the Itô interpretation [105], the corresponding Fokker-Planck equation governing the probability density $\mathscr{P}(\mathrm{X},t)$ is derived as:

$$\frac{\partial \mathscr{P}}{\partial t} = -\frac{\partial}{\partial \mathrm{X}}\left[f(\mathrm{X})\mathscr{P}\right] + \frac{1}{2}\frac{\partial^2}{\partial \mathrm{X}^2}\left[g^2(\mathrm{X})\mathscr{P}\right]. \tag{2.9}$$

The coefficients $f(\mathrm{X})$ and $g(\mathrm{X})$ are general real-valued differentiable functions Eq. 2.9 can be rewritten in the form of a continuity equation for the probability density:

$$\frac{\partial \mathscr{P}(\mathrm{X,t})}{\partial t} = -\frac{\partial J(\mathrm{X,t})}{\partial \mathrm{X}}, \tag{2.10}$$

where $J(\mathrm{X,t})$, the probability flux, is defined as

$$J(\mathrm{X,t}) = f(\mathrm{X})\mathscr{P} - \frac{1}{2}\frac{\partial}{\partial \mathrm{X}}\left[g^2(\mathrm{X})\mathscr{P}\right]. \tag{2.11}$$

The first term corresponds to the drift contribution—deterministic transport of probability—while the second term accounts for diffusive spreading caused by stochastic fluctuations. In a steady state, the probability density becomes time-independent, i.e., $\partial \mathscr{P}(\mathrm{X,t})/\partial t = 0$. This condition implies that the probability current $J(\mathrm{X,t})$ must be spatially constant, and we denote it as J_{ss}. Two distinct scenarios may arise:

1. **Equilibrium:** If $J_{ss}(\mathrm{X},t) = 0$ (with J_{ss} the probability flux at steady-state), detailed balance holds, and the system is in thermodynamic equilibrium.
2. **Non-equilibrium:** If $J_{ss}(\mathrm{X},t) \neq 0$, the probability flux forms a rotational curl in phase space, signaling broken detailed balance and sustained dissipation.

This distinction has enabled experimental detection of detailed balance violations and how such non-equilibrium dynamics are manifest at the mesosopic scale [109].

For one-dimensional Brownian motion in velocity space ($\mathrm{X} = \mathrm{v}$), the drift term reduces to $f(\mathrm{X}) = -\gamma\mathrm{v}$ (damping), while the noise is additive $g(\mathrm{X}) = 1$, recovering the standard Langevin equation (Eq. 2.2). The corresponding Fokker-Planck equation for the velocity distribution $\mathscr{P}(\mathrm{v},t)$ is:

$$\frac{\partial \mathscr{P}}{\partial t} = \gamma\frac{\partial}{\partial \mathrm{v}}(\mathrm{v}\mathscr{P}) + \gamma\frac{k_B T}{m}\frac{\partial^2}{\partial \mathrm{v}^2}\mathscr{P}. \tag{2.12}$$

The first term on the right-hand side corresponds to damping (velocity-dependent friction), while the second term captures diffusion driven by stochastic thermal collisions. Solving the time-dependent Fokker-Planck equation reproduces dynamical predictions identical to those of the Langevin formalism, confirming the equivalence between stochastic trajectory-based and probabilistic density-based descriptions [105]. The stationary solution ($\partial_t \mathscr{P} = 0$, $J_{ss} = 0$) recovers the Maxwell-Boltzmann equilibrium distribution:

$$\mathscr{P}_{\mathrm{eq}}(\mathrm{v}) \propto \exp\left(-\frac{m\mathrm{v}^2}{2k_B T}\right), \tag{2.13}$$

reflecting the equipartition of kinetic energy in thermal equilibrium. This result inherently satisfies the fluctuation-dissipation theorem, Eq. 2.7, which relates the damping coefficient γ to the diffusion constant D and temperature T.

In the overdamped regime (high friction limit, $\gamma \to \infty$), inertial effects become negligible, reducing the Fokker-Planck equation to a diffusion equation for the position probability density $\mathscr{P}(\mathrm{x},t)$:

$$\frac{\partial \mathscr{P}(\mathrm{x},t)}{\partial t} = D\frac{\partial^2 \mathscr{P}(\mathrm{x},t)}{\partial \mathrm{x}^2}, \tag{2.14}$$

where $D = k_B T/\gamma$ is the diffusion coefficient. This equation describes the classic diffusive spreading of probability density, a characteristic of Brownian motion.

Beyond equilibrium systems, the Fokker-Planck formalism has been used for studying active diffusive mixtures in dilute regimes [33]. It serves as a theoretical foundation for understanding non-equilibrium steady states maintained by continuous energy input, emergent phase separation in active diffusive mixtures, and effective surface forces generated by particle activity [15].

2.3 Interacting particles

Thus far, our discussion has been centered on non-interacting particles, realistic systems require incorporating both interparticle interactions and external fields. For a systems of N interacting particles, the total potential energy $\mathscr{V}$ takes the general form:

$$\mathscr{V} = \sum_i v_1(\mathbf{r}_i) + \sum_i \sum_{j>i} v_2(\mathbf{r}_i, \mathbf{r}_j) + \sum_i \sum_{j>i} \sum_{k>j} v_3(\mathbf{r}_i, \mathbf{r}_j, \mathbf{r}_k) + \ldots, \tag{2.15}$$

where $v_1(\mathbf{r}_i)$ describes interactions with external fields (e.g., gravitational potentials, optical traps). The pairwise interaction term $v_2(\mathbf{r}_i, \mathbf{r}_j)$ depends solely on interparticle separation $r_{ij} =$

$|\mathbf{r}_i - \mathbf{r}_j|$, and is thus commonly written as $v_2(r_{ij}) = v_2(r)$. Three-body interactions v_3 become relevant at liquid densities, they are rarely included in computational simulations due to time-consuming [110].

Pairwise interaction (v_2) dominate in most systems due to their computational simplicity and effectiveness in scenarios with weak correlations. However, many-body contributions ($v_3, ...$) become essential in high densities systems or under non-equilibrium conditions (e.g., colloidal glasses, active turbulence), where strong correlations emerge. In active diffusive mixtures, neglecting these higher-order terms limits the ability to capture biologically relevant collective phenomena [59].

The general Langevin equation for a system of N interacting Brownian particles (in the absence of external fields) is:

$$m_i \frac{d\mathrm{v}_i}{dt} = -\gamma \mathrm{v}_i - \frac{\partial}{\partial r_i}\left[\sum_{j\neq i}^{N} v_2(r_{ij})\right] + \xi_i(t), \tag{2.16}$$

this equation incorporates pairwise interactions through the potential $v_2(r_{ij})$, which depends on the interparticle distance r_{ij}. The corresponding Fokker-Planck equation for the probability density $\mathscr{P}(\mathrm{r}_i, \mathrm{v}_i, t)$ is:

$$\frac{\partial \mathscr{P}}{\partial t} = \sum_i \left[-\frac{\partial}{\partial r_i}\mathrm{v}_i + \frac{\partial}{\partial \mathrm{v}_i}\left(\gamma \mathrm{v}_i + \frac{1}{m_i}\frac{\partial}{\partial r_i}\sum_{j>i}^{N} v_2(r_{ij})\right) + \frac{\gamma k_B T}{m_i}\frac{\partial^2}{\partial \mathrm{v}_i^2}\right]\mathscr{P}. \tag{2.17}$$

This formulation describes the time evolution of the probability density for particle positions and velocities, accounting for both deterministic forces and stochastic noise.

In this dissertation, we focus solely on the pairwise dynamics of particles in active diffusive mixtures, excluding external fields. We consider short-range, soft repulsive interactions, with the repulsive potential $\mathscr{V}_R$ taking the following form:

$$\mathscr{V}_R(r_{ij}) = \begin{cases} 2k(r_{ij} - \sigma)^2, & r_{ij} \leq \sigma, \\ 0, & r_{ij} > \sigma, \end{cases} \tag{2.18}$$

where k governs the repulsion strength, and σ is the interaction cutoff distance beyond which particles do not interact. This quadratic form ensures smooth, singularity-free repulsion for $r_{ij} \leq \sigma$, avoiding singularities that can arise from hard-core potentials. The potential is minimized ($F = 0$) at $r_{ij} = \sigma$, ensuring particles repel only when overlapping, making it ideal for simulating soft active particles.

To investigate the role of attraction in active systems, we also consider the Lennard-Jones potential:

$$\mathscr{V}_A = 4\varepsilon \left[\left(\frac{\sigma}{r_{ij}} \right)^{12} - \left(\frac{\sigma}{r_{ij}} \right)^{6} \right], \tag{2.19}$$

where ε sets the depth of the potential well, and σ is the distance at which the potential crosses zero (with the minimum energy occurring at $r_{\min} = 2^{1/6}\sigma$). By incorporating this potential, we aim to probe how attraction modifies collective behavior in active systems, in particular the stability in two-dimensional configurations. The interplay between repulsion and attraction plays a crucial role in determining the emergent properties of active diffusive mixtures. For instance, purely repulsive interactions often lead to phase separation driven by density gradients, whereas attractive forces can stabilize clusters or induce dynamic arrest.

2.4 Numerical approach

Recent advances in computational methods have enabled highly controlled experiments on large groups of interacting particles using computer simulations. These simulations provide precise measurements of key properties, such as order parameters and correlation lengths, and offer flexibility in modeling a variety of interactions. [110]. The behavior of each particle is governed by the Langevin equation (Eq. 2.8). To numerically solve this equation, we use the Euler-Maruyama method, a finite-difference scheme that extends the classical Euler method to stochastic differential equations [111].

In the overdamped limit ($m \to 0$), the Langevin equation for an interacting system (Eq. 2.16) reduces to:

$$\frac{d\mathrm{r}_i}{dt} = \mu \xi_i + \mu \sum_{j>i}^{N} F_{ij}, \tag{2.20}$$

where $\mu = 1/\gamma$ is the mobility (inverse of the Stokes coefficient), and $F_{ij} = -\nabla_i v_2(r_{ij})$ is the pairwise interaction force derived from the potential $v_2(r_{ij})$.

To numerically solve this equation, we discretize time into intervals Δt and update particle positions using the Euler-Maruyama scheme:

$$r_{i,n+1} = r_{i,n} + \mu \sum_{j>i}^{N} F_{ij}\Delta t + \sqrt{2D_i\Delta t}W_n, \tag{2.21}$$

where D_i is the diffusion coefficient of particle i, which depends on its species ($D_i \in [D_{\text{cold}}, D_{\text{hot}}]$). The last term arises from the time discretization of the stochastic process, where $\xi_n = W_n/\sqrt{\Delta t}$,

and W_n are Gaussian random variables generated using the Box-Muller method [112]. This ensures that the stochastic noise satisfies the desired statistical properties, such as zero mean and unit variance.

This numerical framework enables the study of active diffusive mixtures under different channel-like geometries, identifying critical length thresholds for instabilities driven by differential diffusivity. Using Eq. 2.21, we investigate how collective behaviors emerge under variations in density, drift strength, and pairwise interactions. The nature of these interactions significantly influences stability: repulsive interactions amplify non-equilibrium effects, triggering instabilities, while attractive forces suppress activity-induced disorder, stabilizing the system. These findings help us understand how geometry and interparticle interactions jointly govern phase transitions in active matter systems.

2.5 Capillary wave theory

Previous sections focused on methods for describing individual particle dynamics and pairwise interactions through stochastic models, forming the foundation for computational simulations of active diffusive mixtures. While these approaches provide valuable insights into microscopic behaviors, they lack the macroscopic perspective needed to capture emergent phenomena such as phase separation, interface stability, and collective fluctuations. To address this gap, we introduce capillary wave theory, a continuum framework that quantifies the statistical mechanics of interfacial fluctuations. Originally developed for equilibrium systems like liquid-gas boundaries [113, 114] and thin films [115], CWT models interfaces as thermally excited capillary waves, linking microscopic fluctuations to macroscopic properties such as surface tension.

In non-equilibrium systems, like phase segregation in active matter [116] or activity-induced instabilities [102], can be adapted to account for fluctuations driven by continuous energy dissipation rather than thermal noise. By analyzing the spectrum of interfacial fluctuations, CWT provides a framework to infer effective surface tensions, identify stability thresholds, and, in some cases, distinguish equilibrium-like behavior from genuinely non-equilibrium dynamics [116, 117]. This makes it a valuable tool for understanding the interfacial dynamics and scaling properties associated with phase separation in active diffusive mixtures.

This theoretical model describes the roughening transition experienced by a flat interface at equilibrium at very low temperatures, where thermal fluctuations increase both the

total energy and the surface area [118]. In the simplest one-dimensional case, the energy of the interface is described by a quadratic Hamiltonian that depends on the vertical displacement $h(x)$:

$$H = \frac{\rho}{2} \int_L dx \left| \frac{dh(x)}{dx} \right|^2, \tag{2.22}$$

where ρ is the free energy cost per unit length in the absence of fluctuations, commonly referred to as the stiffness or surface tension, and L is the total length of the interface. Assuming small-amplitude distortions, where $\left| \frac{dh(x)}{dx} \right| \ll 1$, this Hamiltonian captures the energetic cost associated with deforming the interface.

To analyze the statistical properties of these fluctuations, we transform the problem into Fourier space using Parseval's identity. This approach allows us to decompose the height profile $h(x)$ into its spectral components $h(k)$, where k denotes the wavenumber, an schematic representation of this can be seen in Fig. 9. By applying the equipartition theorem to thermal fluctuations, the spectral density of height fluctuations is found to be:

$$\langle |h(k)|^2 \rangle = \frac{k_B T}{L \rho k^2}. \tag{2.23}$$

This result reveals the characteristic $1/k^2$ scaling associated with equilibrium interfaces. In non-equilibrium systems that exhibit similar power-law behavior, one can define an effective surface tension ρ_{eff} by fitting the fluctuation spectrum to the $1/k^2$ form. However, deviations from this scaling carry important information about how far the system is from equilibrium. For instance, changes in the power-law exponent may indicate a breakdown of the fluctuation-dissipation theorem, with the altered scaling behavior reflecting the nature of the underlying non-equilibrium dynamics.

Figura 9 – **Fourier Decomposition of Capillary Waves at the Interface.** Schematic representation of the interface roughness and its Fourier decomposition, showing how capillary waves can be analyzed in frequency space. This approach highlights the role of wave modes in characterizing interfacial fluctuations.

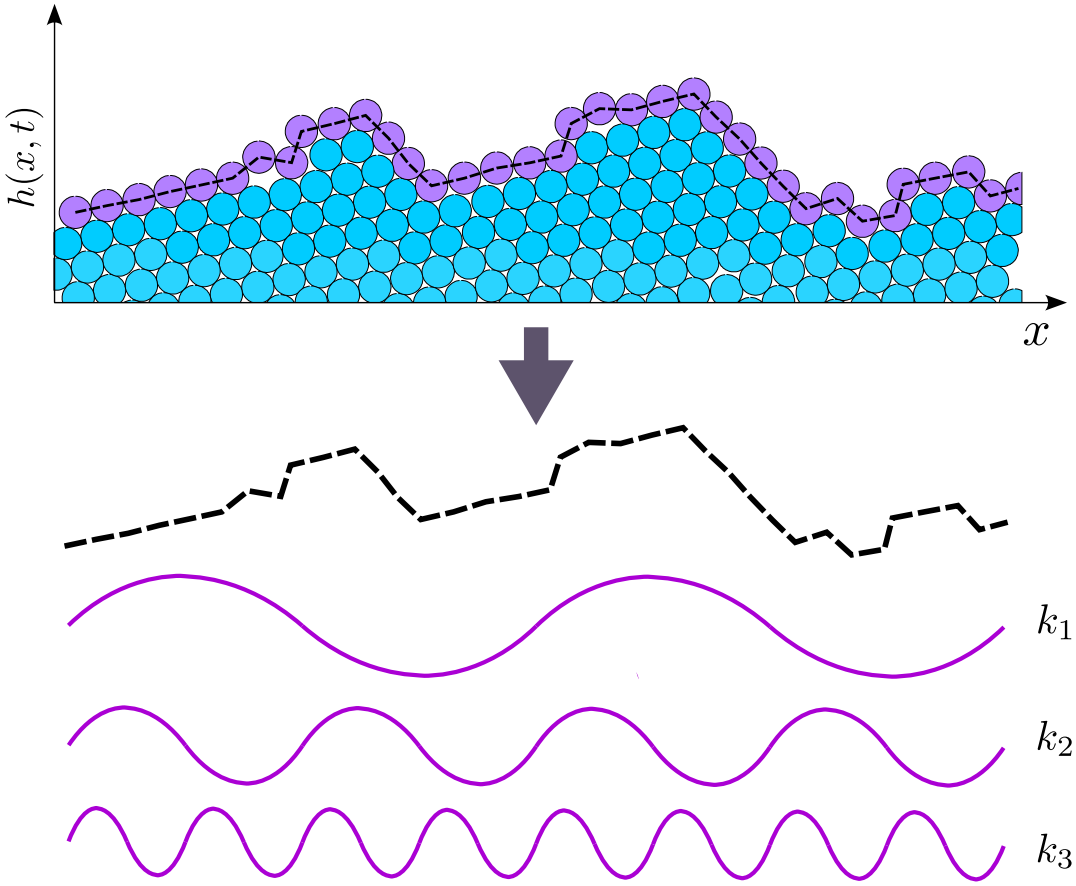

Source: Autor.

3 CHANNEL INSTABILITY IN BINARY MIXTURES WITH DIFFERENTIAL DIFFUSIVITY

This chapter investigates how differential diffusivity drives interfacial instabilities in two-dimensional active matter, inspired by the classical Plateau-Rayleigh instability (PRI). In passive fluids, the PRI describes how surface tension amplifies perturbations to rupture liquid columns into droplets (see Chapter 1) [91]. Here, we adapt this concept to a binary colloidal mixture where particles differ only in diffusivity. By constructing a channel of "cold" (low-diffusivity) particles surrounded by a "hot" (high-diffusivity) gas-like phase, we study the dynamics and stability of this out-of-equilibrium interface.

We chose to model our system around the PRI concept for two main reasons. First, it provides insight into how disturbances grow in free-surface flows [92, 93], analogous to how noise-driven fluctuations affect active systems. Second, it highlights the interplay between interfacial forces and stresses, enabling us to investigate effective surface tension in active mixtures, where stability is governed by non-equilibrium effects rather than cohesive forces. This analogy allows precise control over parameters such as channel length scales and drift, which determine breakup timescales and droplet sizes in the PRI and are crucial for applications reliant on microscale fluid behavior [94, 95].

Although the PRI is not limited to conventional fluids, it also arises in other soft matter systems, such as granular media [119], viscoelastic materials [120], and solids [121], particularly in regimes where surface tension dominates over other stabilizing forces. The critical behavior of the instability, however, depends on the system's dimensionality. The threshold wavelength, which defines the length scale of exponentially growing perturbations, is given by:

$$\lambda_c = \frac{2\pi R}{\sqrt{D-2}} \tag{3.1}$$

where R is the radius of the cylinder and D is the system's dimension. In three dimensions ($D = 3$), perturbations with wavelengths larger than the cylinder's perimeter trigger the instability. In contrast, for two-dimensional systems ($D = 2$), λ_c becomes not finite, indicating that the PRI does not occur in strictly bidimensional configurations, rendering all such systems stable [103].

While two-dimensional fluid-like systems are theoretically stable according to the Plateau-Rayleigh criterion, recent studies have found instabilities in two-dimensional, channel-

like geometries that visually resemble the PRI, despite lacking its classical surface tension mechanism. For instance, chiral fluids display strip breakup into disc-shaped droplets due to stresses caused by "odd viscosity" [102], while driven liquids [116, 72] and active systems [122, 123, 59] present analogous ruptures during segregation processes mediated by activity gradients. These phenomena suggest a distinct instability mechanism that mimics PRI's morphology but originates from non-equilibrium forces such as chiral fluxes, active stress, or motility contrasts. Critically, the role of differential diffusivity in driving interfacial destabilization remains unexplored. This gap in knowledge motivates our study of binary colloidal mixtures, where different diffusivities control how patterns form in non-equilibrium conditions.

In this chapter, we present a numerical analysis of the rupture dynamics of a channel-like structure in a two-dimensional system composed of particles with differing diffusivities. Observations of two-dimensional instabilities in such systems reveal that their collective behavior cannot be fully explained by surface tension effects alone, as assumed in the classical Plateau–Rayleigh instability (PRI) framework. Instead, the instability arises from the interplay between differential diffusivity and repulsive interactions—a dynamic that predominates in two-dimensional environments such as biological systems and active matter. The primary objective is to identify the key variables that govern this instability, using the breakup time (t_b)—defined as the time at which the first rupture occurs—as a quantitative measure of the channel's stability [124].

To study this instability, we perform simulations based on Langevin dynamics, combined with percolation techniques, to measure the breakup time t_b. Our results show that this channel structure is inherently unstable under high diffusivity contrast and repulsive interactions. By systematically varying parameters such as channel width, and particle density, we found that these factors can either delay or accelerate the rupture process. However, the instability is unavoidable due to persistent energy injection at the constituent level.

To better understand the breakup process, we analyze the temporal evolution of the channel's minimum width $w_{\min}(t)$ as it approaches the pinching time ($t \to t_b$). By extracting the power-law scaling $w_{\min} \sim |t - t_b|^{\beta}$, we compare the exponent β with universal similarity solutions derived for pinch-off phenomena in passive fluids [125]. This comparison reveals whether non-equilibrium activity imposes distinct scaling regimes or if it follows the same patterns seen in classical fluid dynamics.

Active Diffusive Mixture

Segregation phenomena have been widely studied in both equilibrium and non-equilibrium systems. In equilibrium, phase separation typically arises from differences in particle size or interaction strength, for instance, entropic demixing of non-adhesive particles driven by depletion forces. In contrast, non-equilibrium systems can exhibit segregation even among identical particles. Examples include MIPS in active Brownian particles and vibrated granular media, where segregation emerges due to activity or external forcing rather than intrinsic particle differences.

In systems of interacting particles with differential diffusivity, thermal equilibrium is maintained only when the diffusivity contrast is low. Beyond a critical threshold, the more diffusive species effectively decouples from the thermal bath, leading to a non-equilibrium steady state characterized by phase separation [15]. Although this mechanism differs fundamentally from the phase separation observed in mixtures of ABPs, where self-propulsion drives MIPS, a striking duality emerges under specific conditions. In particular, ABP mixtures with persistence lengths shorter than the particle radius exhibit dynamics that closely resemble those of diffusive mixtures [4]. This duality highlights how distinct microscopic mechanisms—persistent motion versus differential diffusion—can give rise to similar macroscopic phase behavior.

Systems of active diffusive mixtures arise naturally across biological and synthetic contexts. Examples include chromosome spatial segregation in the nucleus [47], phase separation in cell nucleus [63], enhanced diffusion in enzymes [60], and dynamic rearrangements in crowded cellular environments relevant to biological processes [59]. These phenomena are often governed by differential diffusivity, which also drives non-equilibrium phase separation in polymers and biomolecular condensates: even small differences in mobility can trigger demixing in polymer solutions [57] or influence genome organization through folding kinetics [126]. Notably, unlike equilibrium phase separation, these processes do not require large diffusivity contrasts, as minor asymmetries amplify under non-equilibrium conditions.

This broad applicability, spanning intracellular organization, synthetic active colloids, and polymer physics, highlights the unifying role of differential diffusivity in understanding instabilities across scales. By bridging biological and engineered systems, such models offer insights into how microscopic mobility gradients govern macroscopic self-organization.

3.1 Model

We study a system composed of N particles of radius a, divided into two types that differ solely in their diffusion coefficients: $D_i \in \{D_c, D_h\}$, where D_c and D_h correspond to "cold" (less diffusive) and "hot" (more diffusive) particles, respectively, with $D_c \leq D_h$. The particles interact through the short-range, soft repulsive interactions given by the potential described by Eq. 2.18:

$$\mathbf{F}_{ij} = \begin{cases} k(2a - r_{ij})\hat{\mathbf{r}}_{ij}, & r_{ij} \leq 2a, \\ 0, & \text{otherwise}, \end{cases} \tag{3.2}$$

where k is the repulsion strength, $r_{ij} = |\mathbf{r}_i - \mathbf{r}_j|$ is the distance between the particle centers, and $\hat{\mathbf{r}}_{ij} = (\mathbf{r}_i - \mathbf{r}_j)/r_{ij}$ is the unit vector along the line of centers. The dynamics of the system are governed by a set of overdamped Langevin equations [127, 128, 129]:

$$\dot{\mathbf{r}}_i = \mu \sum_{j>i}^{N} \mathbf{F}_{ij} + \xi_i(t), \tag{3.3}$$

where μ is the inverse of the Stokes coefficient, and $\xi_i(t)$ represents Gaussian white noise with zero mean and unit variance, described in Sec. 2.1. Specifically, the noise satisfies $\langle \xi_i(t)\xi_j(t)\rangle = 2D_i\delta_{ij}\delta(t-t')$, where the noise magnitude is determined by the diffusion coefficient D_i. We define the simulation units based on characteristic parameters of the system: length is measured in units of particle radius a, time is measured in units of $(\mu k)^{-1}$, and other quantities are derived from these. For example, the diffusion coefficient is expressed in units of $a^2\mu k$. In our simulations, the particle radius a, the repulsion strength k, and the inverse of Stokes coefficient μ are all set to unity.

The system is initialized with cold particles arranged in a triangular lattice (lattice constant $2a$), forming a channel structure aligned along the x-axis. The lattice spacing ensures particles are separated by twice their radius, preventing overlap in the initial configuration. The channel's width is determined by the number of cold particle layers n_y, and its length by the number of particles n_x, such that the total number of cold particles composing the channel is $N_c = n_x \times n_y$. This channel is flanked by gas-like phase consisting of N_h hot particles, which are randomly distributed in the surrounding region, as shown in Fig. 10(a).

All simulations are performed in a rectangular box with periodic boundary conditions along both the L_x and L_y directions. The overdamped Langevin dynamics (Equation 3.3) are integrated numerically via the Euler-Maruyama method [130] with a discrete time step of $dt = 0.01(\mu k)^{-1}$. To ensure the robustness of our results, we verified that the outcomes remain consistent even when dt is varied by a factor of 10, either larger or smaller (i.e., $dt \in [0.001, 0.1](\mu k)^{-1}$).

Figura 10 – **Channel configuration.** Snapshots of particle configurations consisting of 960 hot particles (red) and 960 cold particles (blue), with diffusion coefficients $D_h = 5 \times 10^{-3} a^2 \mu k$ and $D_c = 0$, respectively. The simulation was performed in a rectangular box of size $L_x = 240a$ and $L_y = 125a$, with a total packing fraction $\phi = N\pi a^2/(L_x L_y) = 0.2$. a) Initial configuration of the channel, composed of $n_y = 8$ layers of cold particles, with labels indicating the system size. b) Configuration at the moment when the first channel breakup occurring at $t = 1.5 \times 10^6 (\mu k)^{-1}$. c) Configuration at latter times when the cold particles begin to form droplets at $t = 9.3 \times 10^6 (\mu k)^{-1}$.

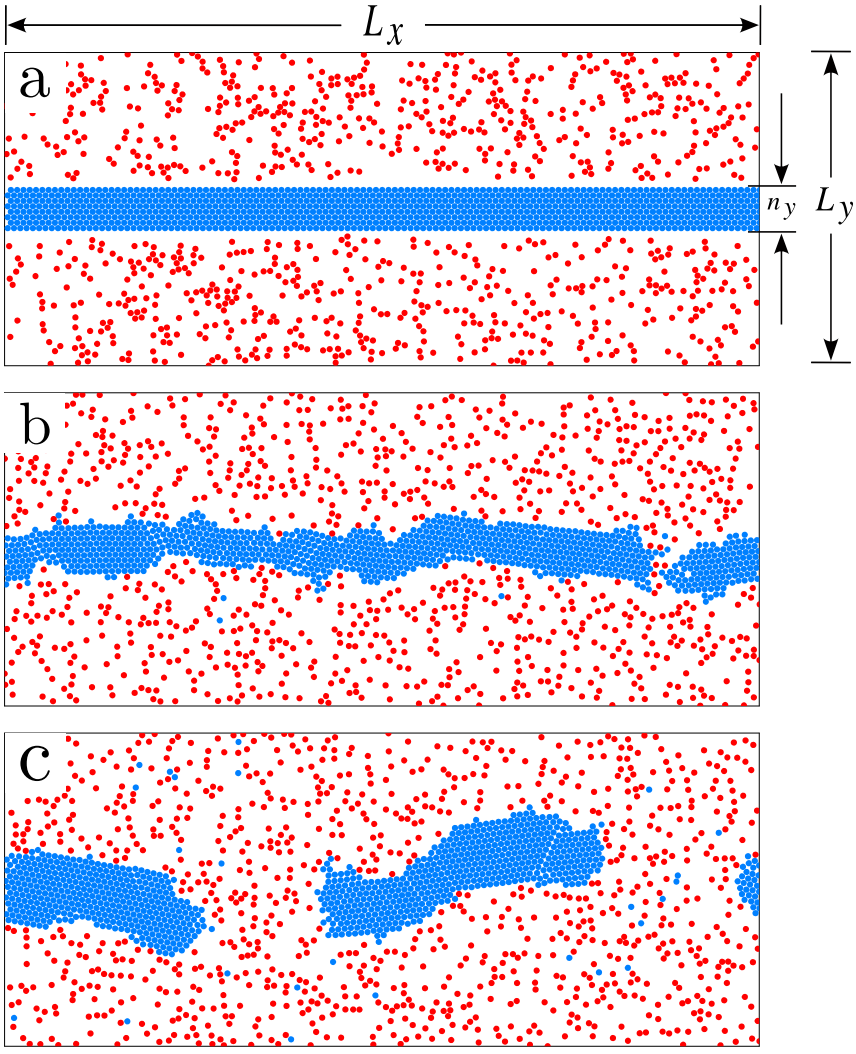

Source: Autor.

The Brownian dynamics simulations reveal that the non-equilibrium energy flux, generated by the hight diffusivity particles, propagates through the system via interparticle interactions. This flux destabilizes the channel structure, inducing fluctuations that culminate in pinch-off, at a characteristic breakup time t_b Fig. 10(b). In this case, the breakup is governed by the non-equilibrium interplay between the differing diffusion coefficients and repulsive forces, resulting in self-organized patterns reminiscent of classical fluid instabilities, such as the Plateau-Rayleigh-like droplet formation in Fig. 10(c). Interestingly, this same channel geometry can stabilize under intermediate density conditions (Fig. 6), where it is particularly relevant to cell-sorting phenomena [59], highlighting the importance of investigating its stability under different conditions. To this end, we systematically examine how the breakup timescale and resulting patterns depend on four key factors: the channel's aspect ratio, the diffusivity of the hot particles, the relative densities of hot and cold particles, and the inclusion of a drift term acting on the cold particles.

3.2 Attractive Interactions

To assess the stability of the two-dimensional channel geometry under attractive interactions, we explore two scenarios. First, we construct a channel identical in geometry to that used in the repulsive interaction case, but here all particles interact via the Lennard-Jones potential (Eq. 2.19) and share the same diffusion constant D. In this setup, we exclude the binary mixture—i.e., no hot particles are introduced—as our aim is not to study differential diffusivity, but rather to examine the role of cohesive forces. Specifically, we test the two-dimensional counterpart of the Plateau-Rayleigh instability, which predicts that channels are stable under small perturbations in 2D due to the absence of destabilizing surface tension effects present in 3D. To probe this, the channel is initialized with sinusoidal perturbations along its boundaries. We systematically vary the wavelength of these perturbations while keeping the initial amplitude ε fixed, as in Fig. 11. In contrast to previous simulations involving differential diffusivity, this system lacks species or mobility contrasts—its stability is determined solely by the interplay between attractive forces and fluctuations.

To examine the evolution and stability of the channel, we track the amplitude of the boundary perturbations, $\varepsilon(t)$, over time. As shown in Fig. 12, the amplitude decays exponentially, indicating the intrinsic stability of the channel. Shorter-wavelength distortions relax significantly faster than longer-wavelength modes. For perturbations with wavelengths similar to or larger

Figura 11 – **Channel perturbation.** Snapshot of a channel composed of particles interacting via the attractive Lennard-Jones potential. The channel boundaries are initialized with sinusoidal perturbations of varying wavelengths to investigate the stability of the configuration.

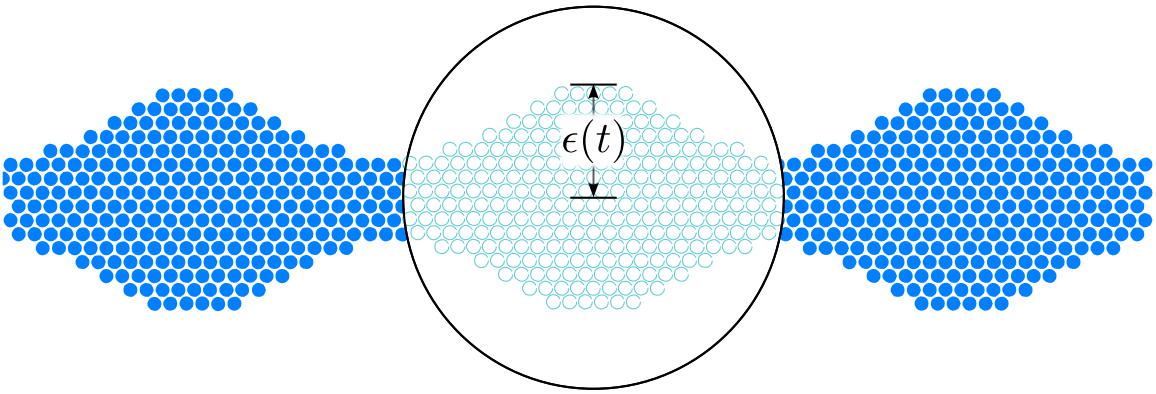

Source: Autor.

than the system size ($\lambda \sim L$), the shape of the channel changes more slowly. In these cases, the structure does not break, but the perturbations take a long time to disappear. As a result, full stabilization is not reached during the simulation time because the large-scale undulations relax very slowly.

In the second scenario, we analyze a binary mixture of particles with differential diffusivity, similar to the repulsive case. Since the channel does not destabilize in this setup, even under high diffusivity contrast, we introduce perturbations at the boundary of the cold particle cluster to test its stability under disturbed conditions (see inset I in Fig.12). When the interactions are governed by the attractive Lennard-Jones potential (Eq. 2.19) instead of the short-range repulsive potential (Eq. 2.18), the channel exhibits significantly enhanced stability under identical diffusivity contrasts. Remarkably, the channel remains stable even when the cold particles have a non-zero diffusion coefficient ($D_c > 0$). This shows that attractive forces between particles are strong enough to prevent the channel from breaking apart, even when there are differences in diffusivity.

The stabilization observed here is due to the cohesive forces provided by the Lennard-Jones potential, which effectively suppress the destabilizing influence of differential diffusivity. These attractive interactions counteract activity-driven fluctuations—such as those caused by diffusivity differences between hot and cold particles—preventing the exponential growth of interfacial perturbations that would otherwise lead to rupture in systems with purely repulsive interactions. This behavior is consistent with the dimensional limitations of the Plateau-Rayleigh

instability, where attractive forces play a stabilizing role similar to surface tension in conventional soft matter systems. As shown in Eq. 3.1, the critical wavelength λ_c diverges ($\sqrt{D-2} \to 0$) in two dimensions ($D = 2$), indicating that the PRI cannot occur in strictly 2D systems[103].

Figura 12 – **Stability in channels with attractive interactions.** Time evolution of the perturbation amplitude $\epsilon(t)$ for three different wavelengths, characterized by the number of anti-nodes n along the channel interface. The plot corresponds to the single-species system with attractive interactions. Insets show snapshots of the channel evolution in the binary mixture case for $n = 7$.

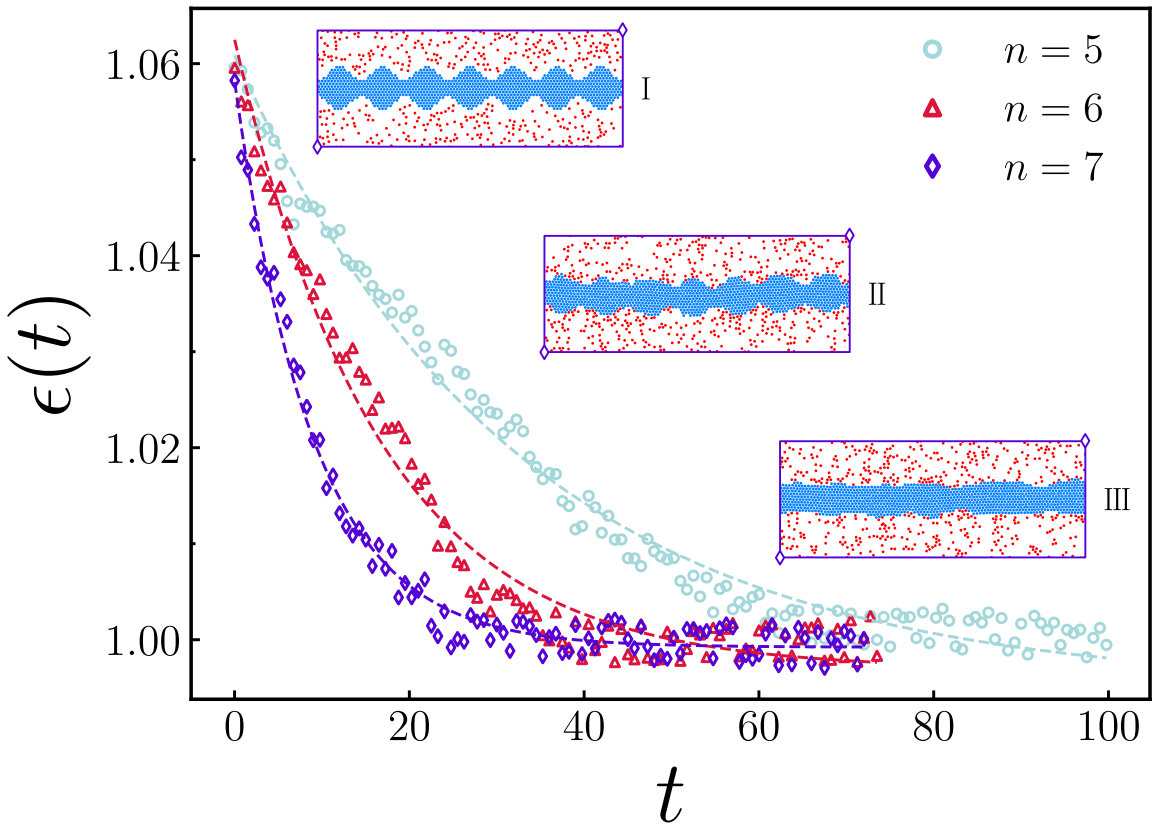

Source: Autor.

Thus, while differential diffusivity alone is sufficient to destabilize systems with purely repulsive interactions, attractive forces create a balance between non-equilibrium activity and particle cohesion. This interplay stabilizes the system, suppressing pinch-off events and producing behavior that resembles equilibrium. Remarkably, this stability persists despite the continuous injection of energy into the system. Nevertheless, since our focus is on understanding the instability of two-dimensional configurations in non-equilibrium conditions, the remainder of this chapter will focus on the case of repulsive interactions.

3.3 Channel Instability

Having established the intrinsic instability of systems with short-range repulsive interactions, we now characterize the instability by identifying the key parameters that govern its emergence and progression. A critical step in this analysis is defining an objective criterion to determine when and where rupture occurs.

To numerically determine the breakup time, t_b, we employ the wrapping condition from the Newman-Ziff algorithm [104], which is particularly well-suited for systems with periodic boundary conditions. This algorithm tracks the connectivity of the "cold" particle cluster: two particles are considered part of the same cluster if their center-to-center distance is less than three particle radii, $3a$. Initially, the cluster is in a percolated state across the system, forming a continuous network. The breakup time, t_b, is defined as the moment when the wrapping condition [104] is no longer satisfied. This means that a gap of at least one particle radius has formed within the channel, at which point the simulation is terminated.

We verify that increasing the gap threshold beyond a does not significantly alter t_b, as the initial gap formation marks an irreversible transition to instability. This robustness ensures our results are insensitive to the choice of termination criterion.

3.3.1 Geometry of the channel

Given that the primary factor determining the PRI is the system's geometry, since the critical wavelength λ_c is set by the cylinder's perimeter, we begin our characterization of the instability in active diffusive mixtures by systematically analyzing the breakup time as a function of the system's geometric parameters. Specifically, we focus on the channel length L_x and the channel width n_y, which is measured by the number of particle layers across the width. This analysis allows us to probe how the aspect ratio governs the dynamics of instability.

In Fig. 13, we show the average breakup time, t_b, as a function of the channel length, L_x, for different values of the initial channel width n_y. Since the channel width introduces a characteristic scale, we assume that the breakup time follows the scaling relation of the form:

$$t_b = n_y^{\alpha} f(L_x/n_y), \tag{3.4}$$

where α quantifies the sensitivity of t_b to channel width, and f is a dimensionless

scaling function. To determine the value of α, we perform a least-squares minimization of the logarithmic deviations of the data across all Lx/ny ratios.

Considering only the data for $n_y \geq 6$ (as the narrower channel $n_y = 5$ deviates significantly from the trend), we find $\alpha = 4.91 \pm 0.21$. Since the integer $\alpha = 5$ lies within the error margin, we adopt this value and present the scaled breakup time t_b/n_y^5, which collapses the data onto a curve in Fig. 13. This scaling relation not only captures the interplay between L_x and n_y but also enables us to extrapolate our results to larger system sizes, which is crucial for studying macroscopic active matter systems.

Figura 13 – **Geometric dependence of the instability.** Average breakup time of the channel, t_b, as a function of the aspect ratio, L_x/n_y, for different channel widths n_y. The diffusion coefficient of the hot particles is set to $D_h = 5 \times 10^{-3} a^2 \mu k$, and the total packing fraction is $\phi = 0.2$. The bars represent one standard deviation over 50 independent simulations. Channels with larger widths ($n_y > 5$) exhibit a strong power-law dependence, $t_b \sim n_y^5$, highlighting the significant influence of channel width on breakup time in this regime. Furthermore, the results suggest the existence of a specific aspect ratio where the system reaches maximum instability, characterized by a sharp decrease in t_b. This implies that at this aspect ratio, external perturbations are most effective in destabilizing the channel.

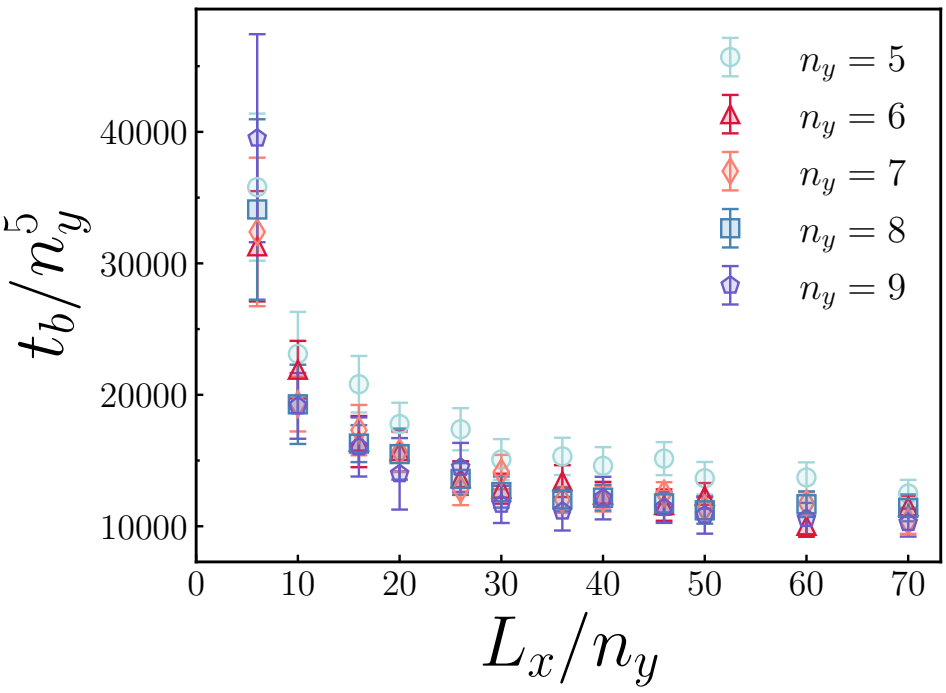

Source: Autor.

We observe that the breakup time t_b increases as the aspect ratio L_x/n_y decreases. Specifically, the scaled breakup time t_b/n_y^5 exhibits a sharp rise for systems with $L_x/n_y < 30$, indicating that channels with smaller aspect ratios (i.e., shorter and wider geometries) are more

robust against perturbations induced by "hot" particles. This behavior is analogous to the PRI [14], where only perturbations with wavelengths exceeding a critical threshold undergo exponential growth. Our results suggest the existence of a similar threshold length in our system, beyond which perturbations grow rapidly, destabilizing the channel.

Interestingly, the observed power-law scaling $t_b \sim n_y^5$ in our system mirrors that reported for the rupture of free liquid films, a phenomenon extensively studied in the context of foams and emulsions. In such systems, the breakup time scales as $t_b \sim h_0^5$, where h_0 represents the uniform thickness of the film [131]. While this similarity hints at universal scaling across disparate systems, the underlying mechanisms differ: in our case, instability arises from non-equilibrium activity (differential diffusivity), whereas in liquid films, it is driven by interfacial tension and drainage dynamics.

A detailed analysis of the temporal evolution of the channel's minimum width (presented later) reveals further parallels to classical pinch-off phenomena, including power-law scaling of the necking dynamics. These findings bridge active matter physics with established frameworks in fluid mechanics, offering a unified perspective on instability across equilibrium and non-equilibrium systems.

3.3.2 Drift Strength

To investigate how external forcing impacts channel stability, we introduce a constant drift velocity v to the "cold" particles, transforming the stationary channel into a propelled jet. This drift models scenarios in which external fields selectively act on the "cold" particles. Our analysis focuses on how the magnitude of the drift velocity v influences the breakup time t_b. As illustrated in Fig. 14, the breakup time t_b grows exponentially with drift strength:

$$t_b \sim e^{\delta v} \tag{3.5}$$

where δ is a coefficient that depends on the channel length L_x. This exponential relationship indicates that even small drift velocities significantly suppress instability. The drift continuously displaces regions where perturbations would otherwise deform the interface and lead to defect formation, thereby effectively delaying rupture.

The interaction between "hot" particles and the moving "cold" channel generates shear at the interface, inducing a velocity gradient between the boundary particles and the bulk.

Figura 14 – **Drift dependence.** Average breakup time, t_b, as a function of the drift strength, v, for different channel lengths, L_x. The data is presented on a semi-logarithmic scale. The diffusion coefficient of the hot particles is fixed at $D_h = 5 \times 10^{-3} a^2 \mu k$, the total packing fraction at $\phi = 0.2$, and the channel width at $n_y = 6$. The bars represent one standard deviation over 25 independent simulations, and dashed lines show exponential fits. The results indicate that t_b increases exponentially with drift strength for all L_x, with a more pronounced stabilization effect in shorter channels. This suggests that the drift term counteracts perturbations induced by hot particles, enhancing stability, particularly in shorter channels.

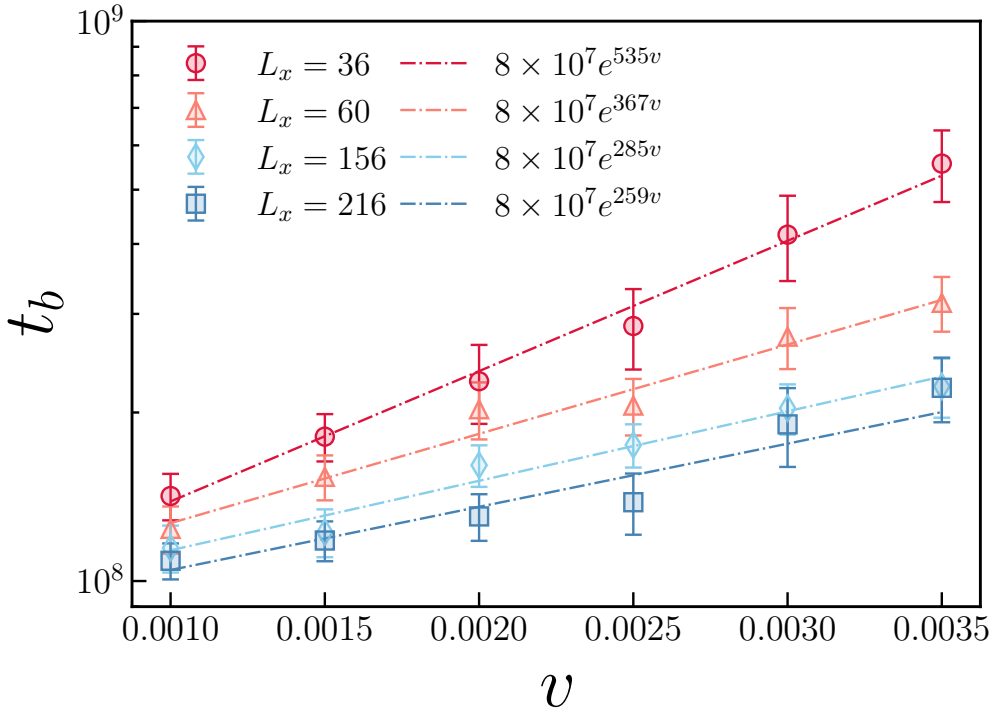

Source: Autor.

This shear introduces a stabilizing effect analogous to the PRI suppression observed in liquid columns [132]. In fluid jets, relative motion between a column's core and its surface suppresses instability for sufficiently thin boundary layers. In our system, the stabilizing effect of drift depends on the channel length L_x, revealing an interplay between geometric constraints and dynamic effects.

Shorter channels exhibit a faster exponential increase in breakup time t_b with increasing drift velocity v, while longer channels show a weaker dependence. This length-dependent behavior arises from a competition between two key timescales: the intrinsic perturbation growth time (τ_g), which governs the amplification of interfacial fluctuations, and the advection time ($\tau_a = L_x/v$), which determines how rapidly particles traverse the channel.

For short channels ($\tau_a \ll \tau_g$), rapid advection limits the time available for perturba-

tions to grow, effectively suppressing instability. This behavior mirrors shear stabilization in fluid jets, where fast relative motion prevents the development of large deformations [132]. In contrast, for long channels, perturbations have sufficient time to amplify, leading to dynamics that resemble those observed in stationary systems.

These findings show that drift velocity v can be used as a control parameter for stabilizing channels. Shorter geometries achieve robust stabilization even with moderate drift, which makes this a useful strategy for dealing with instability in active matter. By combining the effects of geometry and dynamics, these findings open new avenues for designing systems with customized stability properties, applicable to both synthetic materials and biological processes.

3.3.3 Density of hot particles

A critical factor that significantly influences rupture dynamics is the number of hot particles, N_h, which serves as a surrogate for the density of the gas-like phase. The exact density of the system is difficult to quantify due to the undefined excluded area of the cold particles, whose interactions lack a well-defined boundary. To address this, we use N_h as a control parameter, allowing systematic exploration of how the gas-like phase density modulates instability.

By fixing the dimensions of the simulation box and the number of cold particles (N_c) while varying N_h, we isolate the role of hot particle density in rupture dynamics. Modifying N_h increases or decreases the density of the surrounding medium, altering the balance between diffusive behaviors (driven by thermal fluctuations) and interfacial stresses (arising from particle collisions). This balance critically influences the timescales of channel breakup, providing deeper insights into the interplay between density and pattern formation in active systems.

As shown in Fig. 15, N_h plays a critical role in modulating rupture dynamics, with distinct behaviors emerging across three regimes: low, intermediate, and high densities.

At low concentrations of hot particles (region I), interactions between hot particles and the channel interface become less frequent, drastically reducing stochastic collisions. This diminished interaction suppresses surface perturbations, fluctuations that typically initiate instability, slowing their growth along the channel boundaries and significantly prolonging the breakup time t_b. Remarkably, even at minimal hot particle densities, the channel eventually ruptures, demonstrating that the system's inherent instability persists due to differential diffusivity alone. Thus, while N_h modulates the timescales of instability, the fundamental mechanism driving

instability originates from the diffusivity contrast.

Figura 15 – **Density dependence.** Average breakup time of the channel, t_b, as a function of the number of hot particles, N_h, for different channel lengths, L_x. The simulations were performed in a rectangular box of width $L_y = 94.25a$ and channel width of $n_y = 6$. The system exhibits a region of maximum instability at intermediate densities, flanked by two more stable regions, represented by the shaded areas I and II.

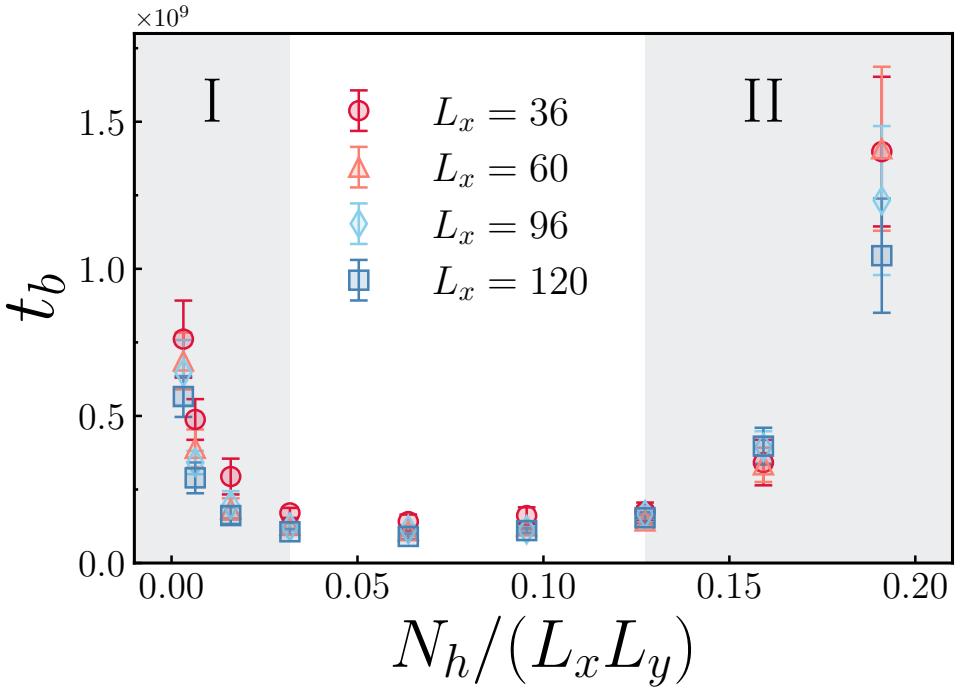

Source: Autor.

As N_h increases, the breakup time decreases, reaching a minimum at intermediate densities (central region). This indicates a regime of maximum instability, where the interactions between hot particles and the channel are most effective at amplifying perturbations. In this regime, the frequent collisions and enhanced mobility of hot particles accelerate the growth of interfacial fluctuations, leading to rapid rupture.

At high densities (region II), the system displays a re-entrant behavior: the breakup time increases again, indicating a return to a more stable regime. This stabilization arises from jamming of the hot particles, where crowding near the channel restricts their diffusion and suppresses collisions. The resulting caging effect reduces momentum transfer to the channel interface, damping perturbations and delaying rupture. As shown in Fig. 16, at high densities the channel does not rupture through smooth interfacial undulations; instead, it breaks in a more abrupt, fracture-like manner, resembling the failure of a solid. Thus, while intermediate densities maximize instability through stochastic forcing, high densities stabilize via collective crowding,

a non-monotonic interplay unique to active mixtures.

Figura 16 – **Hight hot density breakup.** Snapshots of the systems at high densities, consisting of $N = 2160$ particles with 360 cold particles composing the channel and 1800 hot particles, with diffusion coefficient $D_h = 5 \times 10^{-3} a^2 \mu k$. The simulation was performed in a rectangular box of size $L_x = 120a$ and $L_y = 94a$, with total packing fraction of $\phi = 0.60$. a) Intermediate configuration at $t = 1.2 \times 10^6 (\mu k)^{-1}$ of the channel composed of $n_y = 6$ layers of cold particles. b) Configuration at the moment of the first breakup occurring at $t = 2.1 \times 10^6 (\mu k)^{-1}$.

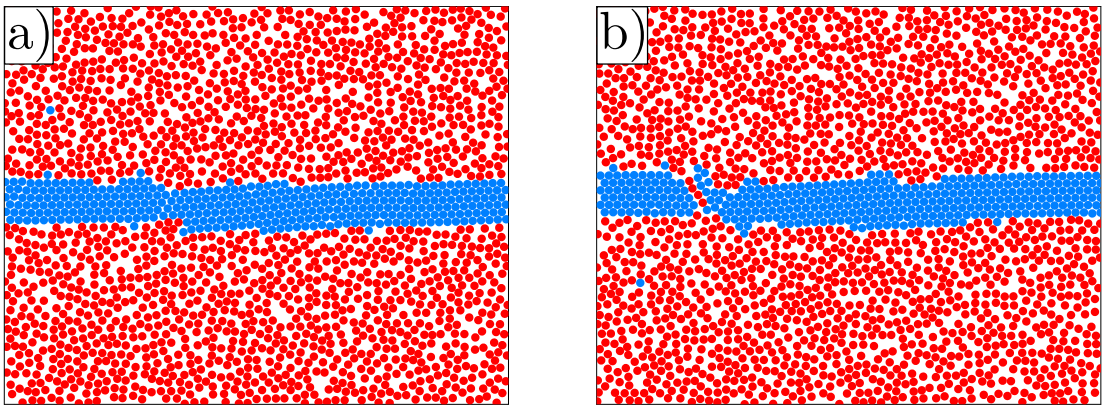

Source: Autor.

The rupture dynamics of the channel reveal that the key parameters influencing its stability—aspect ratio, drift, and particle density—affect the breakup time in distinct ways. Among these, particle density is the only parameter with a non-monotonic impact on instability. As the number of hot particles increases, the system transitions from a stable regime to one of maximum instability before returning to stability due to a caging effect at high densities. This re-entrant behavior underscores the complex interplay between crowding and mobility in active matter systems [59].

In contrast, the aspect ratio defines two distinct instability regions, separated by a threshold value that delineates stable and unstable configurations. This threshold highlights the importance of geometry in determining the stability of the channel, offering insights into how spatial constraints can be used to control rupture dynamics. Meanwhile, the drift term consistently enhances stability, causing an exponential increase in breakup time without introducing new instability thresholds. This shear stabilizing effect demonstrates the potential of directed motion as a robust mechanism for suppressing perturbations.

These findings demonstrate that geometry, drift, and particle density each play a critical role in shaping rupture dynamics. By systematically analyzing these factors, we gain insight into how to control and tune the stability of non-equilibrium systems. This understanding

could inform the design of self-organizing materials and adaptive technologies capable of responding to dynamic environmental conditions.

3.4 Pinch-off Dynamics: minimum width

Having identified the parameters that can suppress or enhance instability, we now focus on the pinch-off dynamics of the channel. In studies of rupture phenomena, a common technique to understand the forces governing the final stage of breakup involves analyzing the scaling law of the minimum radius (for three-dimensional systems like the Plateau-Rayleigh instability) or the minimum width (for two-dimensional systems) as a function of the time remaining until breakup [80]. This approach provides insights into the dominant physical mechanisms driving the pinch-off process.

The value of the exponent in the scaling law reveals the nature of the forces governing the pinch-off process. For example, in the classical PRI, studies have identified distinct exponents corresponding to different physical regimes, such as inertia-dominated, viscosity-dominated, or diffusion-dominated dynamics [125, 133]. By characterizing this scaling law in our system, we aim to identify the dominant forces that govern the final stages of channel rupture. This analysis enhances our understanding of the pinch-off process and highlights potential similarities between active matter systems and passive ones, bridging classical fluid mechanics with active matter physics.

To analyze the rupture dynamics, we track the temporal evolution of the channel's minimum width, w_{min}, as a function of the time remaining until breakup ($\Delta t = t_b - t$). To achieve this, we construct spatial histograms of cold particle positions at each timestep, binarizing the data to identify the channel boundaries using the `contour` function in `MATPLOTLIB` [134]. For every point along one boundary, we compute the perpendicular distance to the opposing boundary, identifying the smallest such distance as w_{min}.

As shown in Fig. 17, w_{min} follows a power-law decay during the final stages of rupture:

$$w_{min} \sim (t_b - t)^{\beta}, \tag{3.6}$$

with the exponent determined to be $\beta = 0.20 \pm 0.01$. This scaling lies outside the classical regimes of the PRI [125], suggesting a novel pinch-off mechanism unique to active diffusive mixtures, where factors such as differential diffusivity may play a dominant role. This finding

highlights the distinct nature of active matter systems, where non-equilibrium forces introduce new modes of instability that differ fundamentally from those in passive systems.

Figura 17 – **Rupture Dynamics.** a) Minimum channel width, w_{min}, as a function of the time until breakup, $(t_b - t)$. The data is presented on a log-log scale. Simulations were performed in a rectangular box with dimensions $L_x = 300a$ and $L_y = 157a$, using $N_h = N_c = 1500$ particles and a total packing fraction of $\phi = 0.2$. The initial channel width was $n_y = 10$, and the diffusion coefficient of the hot particles was fixed at $D_h = 5 \times 10^{-3} a^2 \mu k$. The results show that w_{min} decreases over time following a power-law scaling, $w_{min} \sim (t_b - t)^{\beta}$, with an exponent $\beta = 0.20 \pm 0.20$ (dashed line). This scaling exponent suggests a novel similarity regime with no counterpart in passive systems. The bars represent the standard deviation over 40 independent samples. b) Schematic of w_{min} for one sample approaching the breakup time.

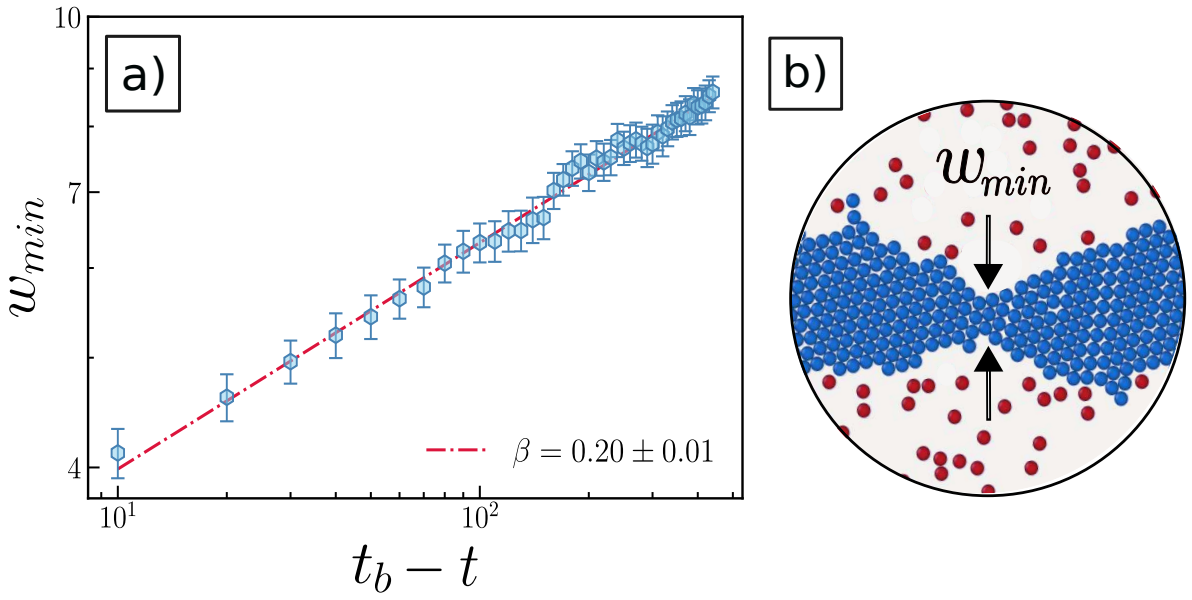

Source: Autor.

The unique geometry and non-equilibrium nature of our system prevent direct comparisons with classical scaling laws, as no universal similarity solutions exist for 2D active diffusive mixtures or analogous non-equilibrium systems. Unlike the PRI, where analytical frameworks provide well-defined parameters such as surface tension and viscosity, our system lacks such thermodynamic quantities. This absence makes it challenging to predict force-driven behaviors in advance and complicates mechanistic interpretations of rupture dynamics. The observed scaling exponent $\beta = 0.20$, is notably smaller than all exponents reported for the PRI, including the diffusion-dominated regime with $\beta = 0.33$. This suggests a greater resistance to thinning and a slower dynamics, which can be attributed to non-equilibrium effects.

In the context of rupture dynamics, the exponent $\beta = 0.20$ has been previously

observed in the power-law thinning of thin liquid films, where Van der Waals forces dominate the process [135]. However, our system represents a fundamentally different scenario, both in terms of dimensionality and the underlying driving mechanisms. Unlike thin liquid films, which are governed by well-defined forces such as surface tension or Van der Waals interactions, the instability in our active system arises from collective effects driven by pronounced differences in diffusivity between particle species.

The emergence of $\beta = 0.20$ in our system suggests the presence of a novel scaling regime unique to active matter. This regime reflects the interplay between stochastic motion, activity-induced stresses, and the geometry of the channel. Such behavior underscores the distinct nature of active systems, where non-equilibrium forces introduce new modes of instability that cannot be explained by traditional frameworks. Understanding this scaling regime not only deepens our insights into the pinch-off process but also provides a foundation for uncovering universal principles governing rupture dynamics in active matter.

In this thesis, we investigated a novel instability mechanism in a two-dimensional active binary mixture of particles with differential diffusivity. This mechanism is fundamentally distinct from rupture phenomena observed in passive systems. While the observed channel breakup and the formation of droplet-like structures resemble the PRI, the underlying mechanism is significantly different: PRI is inherently three-dimensional and governed by surface tension, whereas our system operates in strictly two-dimensional, non-equilibrium conditions. Despite the absence of cohesive forces like surface tension, the interplay between differential diffusivity and repulsive interactions generates an effective destabilizing mechanism that drives rupture.

Through numerical simulations, we identified key parameters—such as aspect ratio, drift strength, and particle density—that govern the breakup dynamics of the channel. We demonstrated that introducing a unidirectional drift to the channel particles enhances stability by counteracting the growth of surface perturbations, a concept of great interest in active microfluidics [136, 137]. A central finding is the re-entrant behavior of instability regimes as the number of "hot"particles increases, driven by the interplay between differential diffusivity and kinetic confinement effects, such as jamming at high densities. This behavior is particularly relevant to biological processes like cell sorting, where similar mechanisms influence structure formation and segregation [59, 138, 139]. Furthermore, our results reveal a power-law scaling behavior for the minimum channel width, $w_{min} \sim (t_b - t)^{\beta}$, with an exponent $\beta = 0.20$. This scaling, along with the identification of a threshold aspect ratio, provides a new framework for

analyzing interface dynamics in two-dimensional active matter. These findings provide insights into pattern formation and instability mechanisms that are unique to non-equilibrium systems.

The methodology developed in this study, combining Brownian dynamics simulations with percolation-based techniques, not only quantifies the stability of active surfaces but also establishes a robust and reproducible framework for investigating interface dynamics under diverse geometries and conditions [140, 141]. This approach enables the systematic exploration of key emergent properties in active systems, such as effective surface tension (arising from diffusivity contrasts), interface roughness (driven by stochastic collisions), and adaptive responses to external perturbations (e.g., shear, confinement) [72, 142].

Furthermore, the framework can be extended to higher-dimensional systems, providing a pathway to deepen our understanding of active matter instabilities and their role in non-equilibrium phase transitions. By bridging microscopic dynamics with macroscopic behavior, this methodology lays the groundwork for uncovering universal principles that govern the collective behavior of active systems.

3.5 Surface Dynamics

In the previous sections, we introduced a novel two-dimensional instability and identified the key parameters that govern its behavior. We also derived scaling laws for the pinch-off dynamics, providing insight into the non-equilibrium nature of the system. However, while these results help characterize the instability, they do not fully explain the forces driving it or the nature of the perturbations that trigger breakup. To address these questions, we now extend the framework using capillary wave theory, as outlined in Sec. 2.5. By analyzing the statistical properties of interface fluctuations, we aim to uncover the physical mechanisms behind the instability and estimate an effective surface tension.

Capillary wave theory has been widely used to describe the roughening of interfaces in equilibrium systems, where thermal fluctuations lead to height variations along the interface [143]. In such systems, CWT predicts well-defined scaling laws that govern interfacial roughness [144], offering insights into the balance between surface tension and thermal agitation [113]. However, extending CWT to active matter requires careful consideration. Interfaces in active systems are shaped by non-equilibrium forces such as self-propulsion and differential diffusivity. These forces break time-reversal symmetry and violate the fluctuation-dissipation theorem, often resulting in behavior that deviates from the scaling laws observed in equilibrium

systems [117].

In some cases, modified scaling laws emerge, reflecting the unique contributions of activity-induced stresses [117]. In others, despite the inherently non-equilibrium nature of the system, interfaces surprisingly follow the same scaling behavior as in equilibrium [38, 62]. This apparent duality remains an open question in the study of surface dynamics, underscoring the need for further investigation into how non-equilibrium forces shape interfacial roughening.

By extending capillary wave theory to active diffusive mixtures, we aim to derive scaling laws that describe non-equilibrium effects—particularly the roughening transition observed at the channel interface. Initially, the cold particle channel is in a low-energy state, corresponding to a flat, well-defined surface. As the hot particles begin to interact with the channel, they disturb its boundary, triggering interfacial roughening. This process reflects the interplay between fluctuations and activity-induced stresses driven by differential diffusivity, which together govern the evolution of the interface.

To analyze the interface at each timestep, we use a procedure similar to the one employed for measuring the minimum width $w_{\min}$. We first construct spatial histograms of particle positions, binarize the data, and use contour detection to extract the channel boundaries. These contours define the active interfaces that serve as the basis for our analysis. Since the detected contours can exhibit overhangs, we apply a smoothing algorithm to convert them into single-valued, continuous height functions. We then compute the spectral density of interface height fluctuations using the Fast Fourier Transform (FFT). This spectral analysis allows us to apply Eq. 2.23 to extract scaling laws that reveal the underlying mechanisms of the system's non-equilibrium behavior and provide a quantitative estimate of the effective surface tension.

The results shown in Fig. 18 were obtained by averaging over an ensemble of 30 independent channel simulations. Since each channel breaks at a different time, we define a scaled time t_s as a percentage of the total breakup time to allow for meaningful comparison. The observed power-law behavior in the spectral density agrees with the findings of Smrek *el. al* [62] who reported similar scaling in a binary polymer mixture with differential diffusivity. Remarkably, even though these systems are out of equilibrium, the interfaces follow the same scaling laws as in thermal equilibrium—a behavior also observed in active Brownian particle systems [46, 38]. This remains an open question in the field.

To the best of our knowledge, the result shown in Fig. 18(b) is novel in the context of rupture dynamics in active systems. It reveals a continuous decrease in the effective

Figura 18 – **Surface evolution.** Ensemble-averaged kinetic roughening of the interface. Simulations were conducted in a rectangular box of dimensions $L_x = 400a$ and $L_y = 94a$, with $N = 2800$ particles, a total packing fraction $\phi = 0.25$, and a channel width of $n_y = 7$. Results were averaged over 30 independent samples. a) Spectral density, multiplied by the interface length, plotted as a function of wavenumber k. The active interface follows the same scaling law Eq. 2.23 as thermal equilibrium interfaces, with $\langle |h(k)|^2 \rangle \sim k^{-\alpha}$ and an exponent $\alpha = 1.98 \pm 0.05$ (dashed line). b) Evolution of the effective surface tension $\beta\rho_{eff}$, obtained via linear fitting, plotted against the scaled time t_s, showing a continuous decrease. c) Time evolution of the exponent α demonstrating that the scaling relation holds throughout the roughening process.

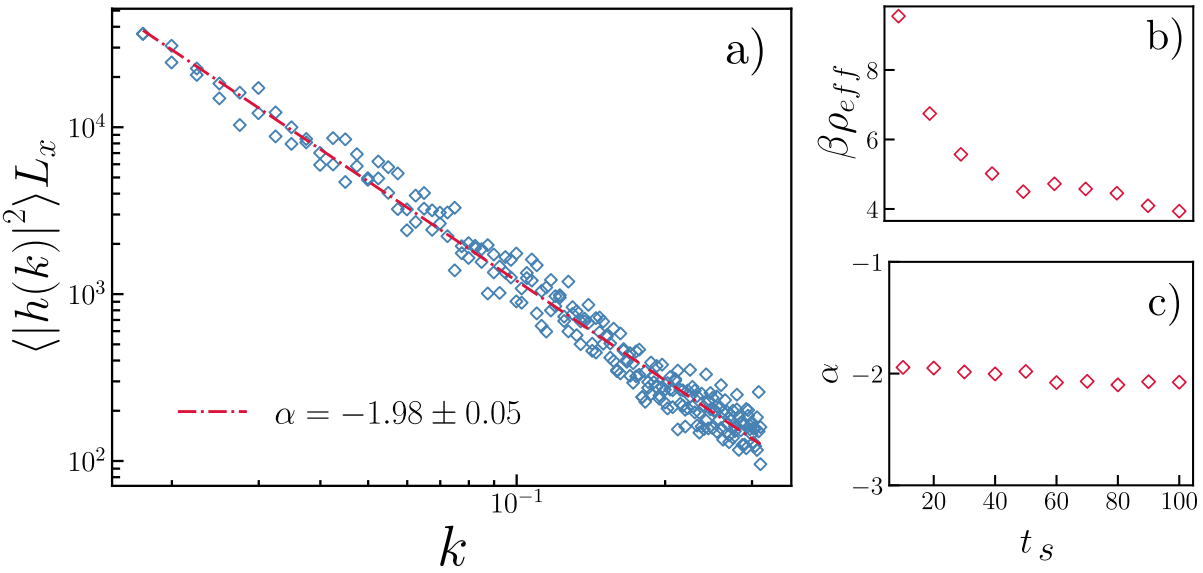

Source: Autor.

surface tension $\beta\rho_{eff}$ as the interface roughness increases, eventually reaching a pseudo-stable plateau before the final breakup. Throughout this process, the perturbations induced by hot particles behave similarly to thermal fluctuations in equilibrium, further reinforcing the surprising consistency with capillary wave theory.

The results presented here mark an initial step toward understanding the mechanics of surface dynamics in active interfaces. This approach allows us to identify the normal modes responsible for breakup and to quantify their growth rates—similar to the analysis of unstable modes in chiral fluids [102]. These spectral quantities provide insight into the force balance that governs each stage of the instability, offering a pathway to disentangle the contributions of activity, fluctuations, and cohesion throughout the rupture process.

4 CONCLUSIONS

Active matter systems, driven by non-equilibrium dynamics, exhibit a wide range of intriguing behaviors—many of which remain poorly understood. Among these, the model of active diffusive mixtures stands out as one of the simplest representations of activity: the particles themselves are not intrinsically active, but activity emerges through interactions between species with contrasting diffusivities. Despite its simplicity, this model displays rich dynamics, including self-organization and emergent behaviors that challenge existing theoretical frameworks and have no counterpart in passive systems.

The analysis of channel instability across various geometrical domains revealed key structural features, including the existence of threshold lengths that govern the onset of rupture—reminiscent of the Plateau–Rayleigh instability. Extending the study to dynamic conditions, where the cold particles experience a constant drift, uncovered a shear-induced stabilization mechanism. This effect depends on the magnitude of the drift and introduces a length-dependent criterion for stability, offering a deeper understanding of how geometry and motion collectively influence the behavior of non-equilibrium systems.

One particularly surprising result emerged when studying the system under varying density conditions, represented in this work by changes in the packing fraction of the cold particles. This parameter introduced non-monotonic stabilization and re-entrant behaviors that were not captured by existing theoretical models. In high-density regimes, the combination of activity and crowding leads to dynamics that deviate significantly from equilibrium behavior, opening the door to new phenomena with no known passive counterpart.

Finally, I identified two key scaling laws related to the time evolution of the instability. The first describes the pinch-off dynamics through the minimum width of the channel, which follows the relation $w_{min} \sim (t_b - t)^{0.20}$. This result provides a foundation for studying rupture dynamics in non-equilibrium configurations. The second scaling law governs the spectral density of interface fluctuations, $\langle |h(k)|^2 \rangle \sim k^{-2}$, indicating that fluctuations induced by high diffusivity contrast behave similarly to thermal fluctuations in equilibrium. This finding allowed for the definition of an effective surface tension and enabled tracking its time evolution throughout the instability process.

Overall, I found this work in active matter to be an effective way to explore non-equilibrium phenomena, which play a central role in many biological processes. It demonstrates how even small differences in diffusivity within a mixture can lead to surprising self-organizing

behaviors, some of which resemble pattern formation typically seen in passive soft matter systems. The combination of Langevin simulations and percolation techniques developed here lays a foundation for future studies of non-equilibrium instabilities in active systems, offering tools to investigate the key parameters that govern rupture dynamics and interfacial behavior.

This work opens several avenues for future research. A natural next step is to extend the analysis to three-dimensional geometries, such as cylindrical configurations resembling Plateau–Rayleigh instabilities or thin films, where curvature and confinement play a key role. These settings may reveal new classes of instabilities relevant to both biological systems and synthetic materials. From a theoretical perspective, investigating the emergent channel structures at high densities could deepen our understanding of the effective surface tension and its role in non-equilibrium systems. In particular, such regimes may exhibit features of a dynamic percolation transition, suggesting the possibility of a non-equilibrium phase transition. Ultimately, these directions may contribute to the design of programmable, self-organizing systems in soft matter physics, active materials, and bioengineering.

REFERENCES

1 KUMAR, N.; SONI, H.; RAMASWAMY, S.; SOOD, A. Flocking at a distance in active granular matter. **Nature communications**, Nature Publishing Group UK London, v. 5, n. 1, p. 4688, 2014.

2 NDLEC, F.; SURREY, T.; MAGGS, A. C.; LEIBLER, S. Self-organization of microtubules and motors. **Nature**, Nature Publishing Group UK London, v. 389, n. 6648, p. 305–308, 1997.

3 FILY, Y.; MARCHETTI, M. C. Athermal phase separation of self-propelled particles with no alignment. **Phys. Rev. Lett.**, American Physical Society, v. 108, p. 235702, Jun 2012.

4 WEBER, S. N.; WEBER, C. A.; FREY, E. Binary mixtures of particles with different diffusivities demix. **Phys. Rev. Lett.**, American Physical Society, v. 116, p. 058301, Feb 2016.

5 KARDAR, M. **Statistical physics of particles**. [S.l.]: Cambridge University Press, 2007.

6 ZWANZIG, R. **Nonequilibrium statistical mechanics**. [S.l.]: Oxford University Press, 2001.

7 RAMASWAMY, S. The mechanics and statistics of active matter. **Annual Review of Condensed Matter Physics**, Annual Reviews, v. 1, n. v. 1, 2010, p. 323–345, 2010. ISSN 1947-5462.

8 SOKOLOV, A.; ARANSON, I. S. Physical properties of collective motion in suspensions of bacteria. **Phys. Rev. Lett.**, American Physical Society, v. 109, p. 248109, Dec 2012.

9 DEGEN, P. Self-propelling capsules as artificial microswimmers. **Current Opinion in Colloid & Interface Science**, v. 19, n. 6, p. 611–619, 2014. ISSN 1359-0294.

10 VICSEK, T.; CZIRÓK, A.; BEN-JACOB, E.; COHEN, I.; SHOCHET, O. Novel type of phase transition in a system of self-driven particles. **Phys. Rev. Lett.**, American Physical Society, v. 75, p. 1226–1229, Aug 1995.

11 BECKER, A. D.; MASOUD, H.; NEWBOLT, J. W.; SHELLEY, M.; RISTROPH, L. Hydrodynamic schooling of flapping swimmers. **Nature communications**, Nature Publishing Group UK London, v. 6, n. 1, p. 8514, 2015.

12 LIEBCHEN, B.; LÖWEN, H. Synthetic chemotaxis and collective behavior in active matter. **Accounts of Chemical Research**, American Chemical Society, v. 51, n. 12, p. 2982–2990, Dec 2018. ISSN 0001-4842.

13 CATES, M. E.; TAILLEUR, J. Motility-induced phase separation. **Annu. Rev. Condens. Matter Phys.**, Annual Reviews, v. 6, n. 1, p. 219–244, 2015.

14 ZHAO, C.; SPRITTLES, J. E.; LOCKERBY, D. A. Revisiting the rayleigh–plateau instability for the nanoscale. **Journal of Fluid Mechanics**, Cambridge University Press, v. 861, p. R3, 2019.

15 ILKER, E.; JOANNY, J.-F. m. c. Phase separation and nucleation in mixtures of particles with different temperatures. **Phys. Rev. Res.**, American Physical Society, v. 2, p. 023200, May 2020.

16 WEBER, C. A.; RYCROFT, C. H.; MAHADEVAN, L. Differential activity-driven instabilities in biphasic active matter. **Phys. Rev. Lett.**, American Physical Society, v. 120, p. 248003, Jun 2018.

17 DUAN, Y.; AGUDO-CANALEJO, J.; GOLESTANIAN, R.; MAHAULT, B. Dynamical pattern formation without self-attraction in quorum-sensing active matter: The interplay between nonreciprocity and motility. **Phys. Rev. Lett.**, American Physical Society, v. 131, p. 148301, Oct 2023.

18 UPLAP, S.; HAGAN, M. F.; BASKARAN, A. Design principles for transporting vesicles with enclosed active particles(a). **Europhysics Letters**, EDP Sciences, IOP Publishing and Società Italiana di Fisica, v. 143, n. 6, p. 67001, oct 2023.

19 WANG, G.; PHAN, T. V.; LI, S.; WOMBACHER, M.; QU, J.; PENG, Y.; CHEN, G.; GOLDMAN, D. I.; LEVIN, S. A.; AUSTIN, R. H.; LIU, L. Emergent field-driven robot swarm states. **Phys. Rev. Lett.**, American Physical Society, v. 126, p. 108002, Mar 2021.

20 NAJMA, B.; WEI, W.-S.; BASKARAN, A.; FOSTER, P. J.; DUCLOS, G. Microscopic interactions control a structural transition in active mixtures of microtubules and molecular motors. **Proceedings of the National Academy of Sciences**, v. 121, n. 2, p. e2300174121, 2024.

21 SIEBERS, F.; JAYARAM, A.; BLüMLER, P.; SPECK, T. Exploiting compositional disorder in collectives of light-driven circle walkers. **Science Advances**, v. 9, n. 15, p. eadf5443, 2023.

22 MARCHETTI, M. C.; JOANNY, J. F.; RAMASWAMY, S.; LIVERPOOL, T. B.; PROST, J.; RAO, M.; SIMHA, R. A. Hydrodynamics of soft active matter. **Rev. Mod. Phys.**, American Physical Society, v. 85, p. 1143–1189, Jul 2013.

23 DELL'ARCIPRETE, D.; BLOW, M. L.; BROWN, A. T.; FARRELL, F. D.; LINTUVUORI, J. S.; MCVEY, A. F.; MARENDUZZO, D.; POON, W. C. A growing bacterial colony in two dimensions as an active nematic. **Nature communications**, Nature Publishing Group UK London, v. 9, n. 1, p. 4190, 2018.

24 PISMEN, L. **Active matter within and around us, from self-propelled particles to flocks and living forms**. [S.l.]: Springer Nature, 2021.

25 GHOSH, S.; SOMASUNDAR, A.; SEN, A. Enzymes as active matter. **Annual Review of Condensed Matter Physics**, Annual Reviews, v. 12, p. 177–200, 2021. ISSN 1947-5462.

26 BALLERINI, M.; CABIBBO, N.; CANDELIER, R.; CAVAGNA, A.; CISBANI, E.; GIARDINA, I.; LECOMTE, V.; ORLANDI, A.; PARISI, G.; PROCACCINI, A.; VIALE, M.; ZDRAVKOVIC, V. Interaction ruling animal collective behavior depends on topological rather than metric distance: Evidence from a field study. **Proceedings of the National Academy of Sciences**, v. 105, n. 4, p. 1232–1237, 2008.

27 GIANNINI, J. A.; PUCKETT, J. G. Testing a thermodynamic approach to collective animal behavior in laboratory fish schools. **Physical Review E**, APS, v. 101, n. 6, p. 062605, 2020.

28 GOMPPER, G.; WINKLER, R. G.; SPECK, T.; SOLON, A.; NARDINI, C.; PERUANI, F.; LöWEN, H.; GOLESTANIAN, R.; KAUPP, U. B.; ALVAREZ, L.; KIøRBOE, T.; LAUGA, E.; POON, W. C. K.; DESIMONE, A.; MUIñOS-LANDIN, S.; FISCHER, A.; SöKER, N. A.; CICHOS, F.; KAPRAL, R.; GASPARD, P.; RIPOLL, M.; SAGUES, F.;

DOOSTMOHAMMADI, A.; YEOMANS, J. M.; ARANSON, I. S.; BECHINGER, C.; STARK, H.; HEMELRIJK, C. K.; NEDELEC, F. J.; SARKAR, T.; ARYAKSAMA, T.; LACROIX, M.; DUCLOS, G.; YASHUNSKY, V.; SILBERZAN, P.; ARROYO, M.; KALE, S. The 2020 motile active matter roadmap. **Journal of Physics: Condensed Matter**, IOP Publishing, v. 32, n. 19, p. 193001, feb 2020.

29 ZHANG, B.; KARANI, H.; VLAHOVSKA, P. M.; SNEZHKO, A. Persistence length regulates emergent dynamics in active roller ensembles. **Soft Matter**, Royal Society of Chemistry, v. 17, n. 18, p. 4818–4825, 2021.

30 FODOR, E.; NARDINI, C.; CATES, M. E.; TAILLEUR, J.; VISCO, P.; WIJLAND, F. van. How far from equilibrium is active matter? **Phys. Rev. Lett.**, American Physical Society, v. 117, p. 038103, Jul 2016.

31 MIZUNO, D.; TARDIN, C.; SCHMIDT, C. F.; MACKINTOSH, F. C. Nonequilibrium mechanics of active cytoskeletal networks. **Science**, American Association for the Advancement of Science, v. 315, n. 5810, p. 370–373, 2007.

32 FODOR, É.; JACK, R. L.; CATES, M. E. Irreversibility and biased ensembles in active matter: Insights from stochastic thermodynamics. **Annual Review of Condensed Matter Physics**, Annual Reviews, v. 13, n. 1, p. 215–238, 2022.

33 GROSBERG, A. Y.; JOANNY, J.-F. Nonequilibrium statistical mechanics of mixtures of particles in contact with different thermostats. **Phys. Rev. E**, American Physical Society, v. 92, p. 032118, Sep 2015.

34 MAGGI, C.; MARCONI, U. M. B.; GNAN, N.; LEONARDO, R. D. Multidimensional stationary probability distribution for interacting active particles. **Scientific reports**, Nature Publishing Group UK London, v. 5, n. 1, p. 10742, 2015.

35 TAKATORI, S. C.; YAN, W.; BRADY, J. F. Swim pressure: stress generation in active matter. **Physical review letters**, APS, v. 113, n. 2, p. 028103, 2014.

36 TAKATORI, S. C.; BRADY, J. F. Towards a thermodynamics of active matter. **Physical Review E**, APS, v. 91, n. 3, p. 032117, 2015.

37 OMAR, A. K.; WANG, Z.-G.; BRADY, J. F. Microscopic origins of the swim pressure and the anomalous surface tension of active matter. **Physical Review E**, APS, v. 101, n. 1, p. 012604, 2020.

38 BIALKÉ, J.; SIEBERT, J. T.; LÖWEN, H.; SPECK, T. Negative interfacial tension in phase-separated active brownian particles. **Physical review letters**, APS, v. 115, n. 9, p. 098301, 2015.

39 SPECK, T. Stochastic thermodynamics for active matter. **Europhysics Letters**, IOP Publishing, v. 114, n. 3, p. 30006, 2016.

40 MANDAL, D.; KLYMKO, K.; DEWEESE, M. R. Entropy production and fluctuation theorems for active matter. **Physical review letters**, APS, v. 119, n. 25, p. 258001, 2017.

41 BOWICK, M. J.; FAKHRI, N.; MARCHETTI, M. C.; RAMASWAMY, S. Symmetry, thermodynamics, and topology in active matter. **Physical Review X**, APS, v. 12, n. 1, p. 010501, 2022.

42 SHANKAR, S.; SOUSLOV, A.; BOWICK, M. J.; MARCHETTI, M. C.; VITELLI, V. Topological active matter. **Nature Reviews Physics**, Nature Publishing Group UK London, v. 4, n. 6, p. 380–398, 2022.

43 TONER, J.; TU, Y. Long-range order in a two-dimensional dynamical xy model: how birds fly together. **Physical review letters**, APS, v. 75, n. 23, p. 4326, 1995.

44 IHLE, T. Towards a quantitative kinetic theory of polar active matter. **The European Physical Journal Special Topics**, Springer, v. 223, n. 7, p. 1293–1314, 2014.

45 DOOSTMOHAMMADI, A.; IGNÉS-MULLOL, J.; YEOMANS, J. M.; SAGUÉS, F. Active nematics. **Nature communications**, Nature Publishing Group UK London, v. 9, n. 1, p. 3246, 2018.

46 PATCH, A. E. **Motility-induced phases: out-of-equilibrium droplets, surfaces, and survival**. Tese (Dissertation) — Syracuse University, United States, 2018. Dissertations - ALL. 930.

47 GANAI, N.; SENGUPTA, S.; MENON, G. I. Chromosome positioning from activity-based segregation. **Nucleic Acids Research**, v. 42, n. 7, p. 4145–4159, 01 2014. ISSN 0305-1048.

48 WENSINK, H. H.; DUNKEL, J.; HEIDENREICH, S.; DRESCHER, K.; GOLDSTEIN, R. E.; LÖWEN, H.; YEOMANS, J. M. Meso-scale turbulence in living fluids. **Proceedings of the national academy of sciences**, National Academy of Sciences, v. 109, n. 36, p. 14308–14313, 2012.

49 CHAIKIN, P. M.; LUBENSKY, T. C. **Principles of Condensed Matter Physics**. New York, NY: Cambridge University Press, 2000. Reprint of the 1995 edition. ISBN 978-0521794503.

50 DOOSTMOHAMMADI, A.; IGNÉS-MULLOL, J.; YEOMANS, J. M.; SAGUÉS, F. Active nematics. **Nature communications**, Nature Publishing Group UK London, v. 9, n. 1, p. 3246, 2018.

51 GIOMI, L.; BOWICK, M. J.; MISHRA, P.; SKNEPNEK, R.; MARCHETTI, M. C. Defect dynamics in active nematics. **Philosophical Transactions of the Royal Society A - Mathematical, Physical and Engineering Sciences**, The Royal Society Publishing, v. 372, n. 2029, p. 20130365, 2014.

52 THAMPI, S. P.; YEOMANS, J. M. Active turbulence in active nematics. **The European Physical Journal Special Topics**, v. 225, n. 4, p. 651–662, Jul 2016. ISSN 1951-6401.

53 GIOMI, L. Geometry and topology of turbulence in active nematics. **Physical Review X**, APS, v. 5, n. 3, p. 031003, 2015.

54 NARAYAN, V.; RAMASWAMY, S.; MENON, N. Long-lived giant number fluctuations in a swarming granular nematic. **Science**, American Association for the Advancement of Science, v. 317, n. 5834, p. 105–108, 2007.

55 SAARLOOS, W. V.; VITELLI, V.; ZERAVCIC, Z. **Soft Matter, Concepts, Phenomena, and Applications**. [S.l.]: Princeton University Press, 2024.

56 ZÖTTL, A.; STARK, H. Modeling active colloids: From active brownian particles to hydrodynamic and chemical fields. **Annual Review of Condensed Matter Physics**, Annual Reviews, v. 14, n. 1, p. 109–127, 2023.

57 SMREK, J.; KREMER, K. Small activity differences drive phase separation in active-passive polymer mixtures. **Phys. Rev. Lett.**, American Physical Society, v. 118, p. 098002, Mar 2017.

58 ILKER, E.; CASTELLANA, M.; JOANNY, J.-F. Long-time diffusion and energy transfer in polydisperse mixtures of particles with different temperatures. **Physical Review Research**, APS, v. 3, n. 2, p. 023207, 2021.

59 MCCARTHY, E.; MANNA, R. K.; DAMAVANDI, O.; MANNING, M. L. Demixing in binary mixtures with differential diffusivity at high density. **Phys. Rev. Lett.**, American Physical Society, v. 132, p. 098301, Feb 2024.

60 XU, M.; ROSS, J. L.; VALDEZ, L.; SEN, A. Direct single molecule imaging of enhanced enzyme diffusion. **Phys. Rev. Lett.**, American Physical Society, v. 123, p. 128101, Sep 2019.

61 BRUINSMA, R.; GROSBERG, A. Y.; RABIN, Y.; ZIDOVSKA, A. Chromatin hydrodynamics. **Biophysical journal**, Elsevier, v. 106, n. 9, p. 1871–1881, 2014.

62 SMREK, J.; KREMER, K. Interfacial properties of active-passive polymer mixtures. **Entropy**, MDPI, v. 20, n. 7, p. 520, 2018.

63 JIANG, Z.; QI, Y.; KAMAT, K.; ZHANG, B. Phase separation and correlated motions in motorized genome. **The Journal of Physical Chemistry B**, ACS Publications, v. 126, n. 30, p. 5619–5628, 2022.

64 CHATTOPADHYAY, J.; RAMASWAMY, S.; DASGUPTA, C.; MAITI, P. K. Two-temperature activity induces liquid-crystal phases inaccessible in equilibrium. **Physical Review E**, APS, v. 107, n. 2, p. 024701, 2023.

65 SCHWARCZ, D.; BUROV, S. Emergence of directed motion in a crowded suspension of overdamped particles with different effective temperatures. **Physical Review Research**, APS, v. 6, n. 1, p. 013156, 2024.

66 GHAFFARIZADEH, S. A.; WANG, G. J. Excess entropy scaling in active-matter systems. **The Journal of Physical Chemistry Letters**, ACS Publications, v. 13, n. 22, p. 4949–4954, 2022.

67 ROMANCZUK, P.; BÄR, M.; EBELING, W.; LINDNER, B.; SCHIMANSKY-GEIER, L. Active brownian particles: From individual to collective stochastic dynamics. **The European Physical Journal Special Topics**, Springer, v. 202, p. 1–162, 2012.

68 WYSOCKI, A.; WINKLER, R. G.; GOMPPER, G. Propagating interfaces in mixtures of active and passive brownian particles. **New journal of physics**, IOP Publishing, v. 18, n. 12, p. 123030, 2016.

69 SHAEBANI, M. R.; WYSOCKI, A.; WINKLER, R. G.; GOMPPER, G.; RIEGER, H. Computational models for active matter. **Nature Reviews Physics**, Nature Publishing Group UK London, v. 2, n. 4, p. 181–199, 2020.

70 HALLATSCHEK, O.; DATTA, S. S.; DRESCHER, K.; DUNKEL, J.; ELGETI, J.; WACLAW, B.; WINGREEN, N. S. Proliferating active matter. **Nature Reviews Physics**, Nature Publishing Group UK London, v. 5, n. 7, p. 407–419, 2023.

71 CAGNETTA, F.; EVANS, M. R.; MARENDUZZO, D. Kinetic roughening in active interfaces. In: EPJ WEB OF CONFERENCES. **EPJ Web of Conferences**. [S.l.], 2020. v. 230, p. 00001.

72 JUNCO, C. del; VAIKUNTANATHAN, S. Interface height fluctuations and surface tension of driven liquids with time-dependent dynamics. **The Journal of Chemical Physics**, v. 150, n. 9, p. 094708, 03 2019. ISSN 0021-9606.

73 SPECK, T. Collective forces in scalar active matter. **Soft Matter**, The Royal Society of Chemistry, v. 16, p. 2652–2663, 2020.

74 GROSBERG, A. Y.; JOANNY, J.-F. Dissipation in a system driven by two different thermostats. **Polymer Science, Series C**, Springer, v. 60, p. 118–121, 2018.

75 CHARI, S. S. N.; DASGUPTA, C.; MAITI, P. K. Scalar activity induced phase separation and liquid–solid transition in a lennard-jones system. **Soft matter**, Royal Society of Chemistry, v. 15, n. 36, p. 7275–7285, 2019.

76 LEE, C. F. Interface stability, interface fluctuations, and the gibbs–thomson relationship in motility-induced phase separations. **Soft matter**, Royal Society of Chemistry, v. 13, n. 2, p. 376–385, 2017.

77 ZIA, R.; LEUNG, K.-T. Interfacial correlation and dispersion in a non-equilibrium steady state system. **Journal of Physics A - Mathematical and General**, IOP Publishing, v. 24, n. 24, p. L1399, 1991.

78 BESSE, M.; FAUSTI, G.; CATES, M. E.; DELAMOTTE, B.; NARDINI, C. Interface roughening in nonequilibrium phase-separated systems. **Physical Review Letters**, APS, v. 130, n. 18, p. 187102, 2023.

79 ADKINS, R.; KOLVIN, I.; YOU, Z.; WITTHAUS, S.; MARCHETTI, M. C.; DOGIC, Z. Dynamics of active liquid interfaces. **Science**, American Association for the Advancement of Science, v. 377, n. 6607, p. 768–772, 2022.

80 GOPAN, N.; SATHIAN, S. P. Rayleigh instability at small length scales. **Physical Review E**, APS, v. 90, n. 3, p. 033001, 2014.

81 ALERT, R.; BLANCH-MERCADER, C.; CASADEMUNT, J. Active fingering instability in tissue spreading. **Physical review letters**, APS, v. 122, n. 8, p. 088104, 2019.

82 YANG, L.; EPSTEIN, I. R. Oscillatory turing patterns in reaction-diffusion systems with two coupled layers. **Physical review letters**, APS, v. 90, n. 17, p. 178303, 2003.

83 WERELEY, S. T.; LUEPTOW, R. M. Velocity field for taylor–couette flow with an axial flow. **Physics of Fluids**, American Institute of Physics, v. 11, n. 12, p. 3637–3649, 1999.

84 SMYTH, W. D.; MOUM, J. N. Ocean mixing by kelvin-helmholtz instability. **Oceanography**, JSTOR, v. 25, n. 2, p. 140–149, 2012.

85 FEI, C.; MAO, S.; YAN, J.; ALERT, R.; STONE, H. A.; BASSLER, B. L.; WINGREEN, N. S.; KOšMRLJ, A. Nonuniform growth and surface friction determine bacterial biofilm morphology on soft substrates. **Proceedings of the National Academy of Sciences**, v. 117, n. 14, p. 7622–7632, 2020.

86 MARTíNEZ-CALVO, A.; BHATTACHARJEE, T.; BAY, R. K.; LUU, H. N.; HANCOCK, A. M.; WINGREEN, N. S.; DATTA, S. S. Morphological instability and roughening of growing 3d bacterial colonies. **Proceedings of the National Academy of Sciences**, v. 119, n. 43, p. e2208019119, 2022.

87 LOHSE, D. Fundamental fluid dynamics challenges in inkjet printing. **Annual Review of Fluid Mechanics**, Annual Reviews, v. 54, p. 349–382, 2022. ISSN 1545-4479.

88 CRASTER, R. V.; MATAR, O. K. Dynamics and stability of thin liquid films. **Rev. Mod. Phys.**, American Physical Society, v. 81, p. 1131–1198, Aug 2009.

89 Porter, J.; Salgado Sánchez, P.; Shevtsova, V.; Yasnou, V. A review of fluid instabilities and control strategies with applications in microgravity. **Math. Model. Nat. Phenom.**, v. 16, p. 24, 2021.

90 BODENSCHATZ, E.; PESCH, W.; AHLERS, G. Recent developments in rayleigh-bénard convection. **Annual review of fluid mechanics**, v. 32, n. 1, p. 709–778, 2000.

91 MEAD-HUNTER, R.; KING, A. J. C.; MULLINS, B. J. Plateau rayleigh instability simulation. **Langmuir**, v. 28, n. 17, p. 6731–6735, 2012. PMID: 22512475.

92 MOSELER, M.; LANDMAN, U. Formation, stability, and breakup of nanojets. **Science**, American Association for the Advancement of Science, v. 289, n. 5482, p. 1165–1169, 2000.

93 EGGERSDORFER, M. L.; SEYBOLD, H.; OFNER, A.; WEITZ, D. A.; STUDART, A. R. Wetting controls of droplet formation in step emulsification. **Proceedings of the National Academy of Sciences**, v. 115, n. 38, p. 9479–9484, 2018.

94 DERBY, B. Inkjet printing of functional and structural materials: Fluid property requirements, feature stability, and resolution. **Annual Review of Materials Research**, Annual Reviews, v. 40, n. Volume 40, 2010, p. 395–414, 2010. ISSN 1545-4118.

95 EGGERS, J.; VILLERMAUX, E. Physics of liquid jets. **Reports on Progress in Physics**, v. 71, n. 3, p. 036601, feb 2008.

96 BANERJEE, A. Rayleigh-taylor instability: A status review of experimental designs and measurement diagnostics. **Journal of Fluids Engineering**, American Society of Mechanical Engineers, v. 142, n. 12, p. 120801, 2020.

97 THOMÉ, H.; RABAUD, M.; HAKIM, V.; COUDER, Y. The saffman–taylor instability: From the linear to the circular geometry. **Physics of Fluids A - Fluid Dynamics**, American Institute of Physics, v. 1, n. 2, p. 224–240, 1989.

98 MASSON, A.; NYKYRI, K. Kelvin–helmholtz instability: lessons learned and ways forward. **Space Science Reviews**, Springer, v. 214, n. 4, p. 71, 2018.

99 VINNINGLAND, J. L.; JOHNSEN, Ø.; FLEKKØY, E. G.; TOUSSAINT, R.; MÅLØY, K. J. Granular rayleigh-taylor instability: experiments and simulations. **Physical review letters**, APS, v. 99, n. 4, p. 048001, 2007.

100 CHEVALIER, C.; LINDNER, A.; CLEMENT, E. Destabilization of a saffman-taylor fingerlike pattern in a granular suspension. **Physical review letters**, APS, v. 99, n. 17, p. 174501, 2007.

101 MILES, C. J.; EVANS, A. A.; SHELLEY, M. J.; SPAGNOLIE, S. E. Active matter invasion of a viscous fluid: Unstable sheets and a no-flow theorem. **Physical Review Letters**, APS, v. 122, n. 9, p. 098002, 2019.

102 SONI, V.; BILILIGN, E. S.; MAGKIRIADOU, S.; SACANNA, S.; BARTOLO, D.; SHELLEY, M. J.; IRVINE, W. T. The odd free surface flows of a colloidal chiral fluid. **Nature physics**, Nature Publishing Group UK London, v. 15, n. 11, p. 1188–1194, 2019.

103 CARDOSO, V.; DIAS, O. J. C. Rayleigh-plateau and gregory-laflamme instabilities of black strings. **Phys. Rev. Lett.**, American Physical Society, v. 96, p. 181601, May 2006.

104 NEWMAN, M. E. J.; ZIFF, R. M. Fast monte carlo algorithm for site or bond percolation. **Phys. Rev. E**, American Physical Society, v. 64, p. 016706, Jun 2001.

105 KAMPEN, N. G. V. **Stochastic processes in physics and chemistry**. [S.l.]: Elsevier, 1992. v. 1.

106 RISKEN, H.; RISKEN, H. **Fokker-planck equation**. [S.l.]: Springer, 1996.

107 FANG, X.; KRUSE, K.; LU, T.; WANG, J. Nonequilibrium physics in biology. **Reviews of Modern Physics**, APS, v. 91, n. 4, p. 045004, 2019.

108 GNESOTTO, F. S.; MURA, F.; GLADROW, J.; BROEDERSZ, C. P. Broken detailed balance and non-equilibrium dynamics in living systems: a review. **Reports on Progress in Physics**, IOP Publishing, v. 81, n. 6, p. 066601, 2018.

109 BATTLE, C.; BROEDERSZ, C. P.; FAKHRI, N.; GEYER, V. F.; HOWARD, J.; SCHMIDT, C. F.; MACKINTOSH, F. C. Broken detailed balance at mesoscopic scales in active biological systems. **Science**, American Association for the Advancement of Science, v. 352, n. 6285, p. 604–607, 2016.

110 ALLEN, M. P.; TILDESLEY, D. J. **Computer simulation of liquids**. [S.l.]: Oxford university press, 2017.

111 TOSCHI, F.; SEGA, M. **Flowing matter**. [S.l.]: Springer Nature, 2019.

112 BOX, G. E.; MULLER, M. E. A note on the generation of random normal deviates. **The annals of mathematical statistics**, Institute of Mathematical Statistics, v. 29, n. 2, p. 610–611, 1958.

113 BEDEAUX, D.; WEEKS, J. D. Correlation functions in the capillary wave model of the liquid–vapor interface. **The Journal of Chemical Physics**, v. 82, n. 2, p. 972–979, 01 1985. ISSN 0021-9606.

114 MACDOWELL, L. G. Capillary wave theory of adsorbed liquid films and the structure of the liquid-vapor interface. **Physical Review E**, APS, v. 96, n. 2, p. 022801, 2017.

115 ZHANG, Y.; DING, Z. Capillary nanowaves on surfactant-laden liquid films with surface viscosity and elasticity. **Physical Review Fluids**, APS, v. 8, n. 6, p. 064001, 2023.

116 JUNCO, C. del; TOCIU, L.; VAIKUNTANATHAN, S. Energy dissipation and fluctuations in a driven liquid. **Proceedings of the National Academy of Sciences**, v. 115, n. 14, p. 3569–3574, 2018.

117 LEUNG, K.-T.; ZIA, R. Anomalous interfacial correlations in non-equilibrium anisotropic systems. **Journal of Physics A: Mathematical and General**, IOP Publishing, v. 26, n. 16, p. L737, 1993.

118 BARABÁSI, A.-L.; STANLEY, H. E. **Fractal concepts in surface growth**. [S.l.]: Cambridge university press, 1995.

119 PRADO, G.; AMAROUCHENE, Y.; KELLAY, H. Experimental evidence of a rayleigh-plateau instability in free falling granular jets. **Phys. Rev. Lett.**, American Physical Society, v. 106, p. 198001, May 2011.

120 TAMIM, S. I.; BOSTWICK, J. B. Plateau–rayleigh instability in a soft viscoelastic material. **Soft Matter**, The Royal Society of Chemistry, v. 17, p. 4170–4179, 2021.

121 XUAN, C.; BIGGINS, J. Plateau-rayleigh instability in solids is a simple phase separation. **Phys. Rev. E**, American Physical Society, v. 95, p. 053106, May 2017.

122 KUMARI, S.; NUNES, A. S.; ARAúJO, N. A. M.; GAMA, M. M. Telo da. Demixing of active particles in the presence of external fields. **The Journal of Chemical Physics**, v. 147, n. 17, p. 174702, 11 2017. ISSN 0021-9606.

123 AI, B.-q.; ZHOU, B.-y.; ZHANG, X.-m. Binary mixtures of active and passive particles on a sphere. **Soft Matter**, The Royal Society of Chemistry, v. 16, p. 4710–4717, 2020.

124 GOMES, M. C. **Dinâmica de Langevin para partículas repulsivas: sistemas confinados e segregação baseada em difusividade**. Tese (Doutorado) — Universidade Federal do Ceará, Fortaleza, 2025.

125 BARKER, B.; BELL, J. B.; GARCIA, A. L. Fluctuating hydrodynamics and the rayleigh–plateau instability. **Proceedings of the National Academy of Sciences**, v. 120, n. 30, p. e2306088120, 2023.

126 GOYCHUK, A.; KANNAN, D.; CHAKRABORTY, A. K.; KARDAR, M. Polymer folding through active processes recreates features of genome organization. **Proceedings of the National Academy of Sciences**, National Academy of Sciences, v. 120, n. 20, p. e2221726120, 2023.

127 ANDRADE, J. S.; SILVA, G. F. T. da; MOREIRA, A. A.; NOBRE, F. D.; CURADO, E. M. F. Thermostatistics of overdamped motion of interacting particles. **Phys. Rev. Lett.**, American Physical Society, v. 105, p. 260601, Dec 2010.

128 BARROZO, P.; MOREIRA, A. A.; AGUIAR, J. A.; ANDRADE, J. S. Model of overdamped motion of interacting magnetic vortices through narrow superconducting channels. **Phys. Rev. B**, American Physical Society, v. 80, p. 104513, Sep 2009.

129 MOREIRA, A. A.; VIEIRA, C. M.; CARMONA, H. A.; ANDRADE, J. S.; TSALLIS, C. Overdamped dynamics of particles with repulsive power-law interactions. **Phys. Rev. E**, American Physical Society, v. 98, p. 032138, Sep 2018.

130 KLOEDEN, P. E.; PLATEN, E. **Numerical Solution of Stochastic Differential Equations**. [S.l.]: Springer, 1992. v. 23. (Applications of Mathematics, v. 23).

131 VRIJ, A. Possible mechanism for the spontaneous rupture of thin, free liquid films. **Discuss. Faraday Soc.**, The Royal Society of Chemistry, v. 42, p. 23–33, 1966.

132 GAñáN-CALVO, A. M.; HERRADA, M. A.; MONTANERO, J. M. How does a shear boundary layer affect the stability of a capillary jet? **Physics of Fluids**, v. 26, n. 6, p. 061701, 06 2014. ISSN 1070-6631.

133 ZHAO, C.; LOCKERBY, D. A.; SPRITTLES, J. E. Dynamics of liquid nanothreads: Fluctuation-driven instability and rupture. **Physical Review Fluids**, APS, v. 5, n. 4, p. 044201, 2020.

134 HUNTER, J. D. Matplotlib: A 2d graphics environment. **Computing in Science & Engineering**, v. 9, n. 3, p. 90–95, 2007.

135 ZHAO, C.; LIU, J.; LOCKERBY, D. A.; SPRITTLES, J. E. Fluctuation-driven dynamics in nanoscale thin-film flows: Physical insights from numerical investigations. **Phys. Rev. Fluids**, American Physical Society, v. 7, p. 024203, Feb 2022.

136 CHANDRAGIRI, S.; DOOSTMOHAMMADI, A.; YEOMANS, J. M.; THAMPI, S. P. Active transport in a channel: stabilisation by flow or thermodynamics. **Soft matter**, Royal Society of Chemistry, v. 15, n. 7, p. 1597–1604, 2019.

137 PATEL, K.; STARK, H. Fluid interfaces laden by force dipoles: towards active matter-driven microfluidic flows. **Soft Matter**, Royal Society of Chemistry, v. 19, n. 12, p. 2241–2253, 2023.

138 ROZMAN, J.; YEOMANS, J. M. Cell sorting in an active nematic vertex model. **Physical Review Letters**, APS, v. 133, n. 24, p. 248401, 2024.

139 MONDAL, K.; BERA, P.; GHOSH, P. Diverse morphology and motility induced emergent order in bacterial collectives. **The Journal of Chemical Physics**, v. 161, n. 9, p. 50, 2024.

140 LANGFORD, L.; OMAR, A. K. Theory of capillary tension and interfacial dynamics of motility-induced phases. **Physical Review E**, APS, v. 110, n. 5, p. 054604, 2024.

141 YUE, H.; PACKARD, C. R.; SUSSMAN, D. M. Scale-dependent sharpening of interfacial fluctuations in shape-based models of dense cellular sheets. **Soft Matter**, Royal Society of Chemistry, v. 20, n. 47, p. 9444–9453, 2024.

142 NGUYEN, M.; QIU, Y.; VAIKUNTANATHAN, S. Organization and self-assembly away from equilibrium: Toward thermodynamic design principles. **Annual Review of Condensed Matter Physics**, Annual Reviews, v. 12, n. 1, p. 273–290, 2021.

143 ZHANG, Y.; SPRITTLES, J. E.; LOCKERBY, D. A. Thermal capillary wave growth and surface roughening of nanoscale liquid films. **Journal of Fluid Mechanics**, Cambridge University Press, v. 915, p. A135, 2021.

144 VINK, R.; HORBACH, J.; BINDER, K. Capillary waves in a colloid-polymer interface. **The Journal of chemical physics**, AIP Publishing, v. 122, n. 13, 2005.

145 RAMIREZ, M. T.; GOMES, M. C.; ANDRADE, J. S.; MOREIRA, A. A. Channel instability in binary mixtures with differential diffusivity. **Soft Matter**, Royal Society of Chemistry, 2025.

146 RAMIREZ, M. T.; ANDRADE, J. S.; MOREIRA, A. A. Screening potentials derived from the central force problem in a deformed space. **Europhysics Letters**, IOP Publishing, v. 138, n. 4, p. 40001, 2022.

APPENDIX A - PUBLISHED ARTICLE

- The results concerning the characterization of the channel instability, including the scaling law of the rupture dynamics [145], were published in **Soft Matter**. The findings related to the attractive case, including the analysis of surface dynamics and the effective surface tension, are currently being prepared for submission in a separate article.

Soft Matter

COMMUNICATION

Channel instability in binary mixtures with differential diffusivity

Michael T. Ramirez, * Marciel C. Gomes, José S. Andrade Jr and André A. Moreira

Cite this: *Soft Matter*, 2025, **21**, 3184

Received 16th January 2025,
Accepted 22nd March 2025

DOI: 10.1039/d5sm00058k

rsc.li/soft-matter-journal

Rupture dynamics and pinch-off phenomena are fundamental for understanding instabilities in fluid dynamics and biological systems. In this study, we investigate the rupture of two-dimensional, channel-like configurations in a binary mixture of particles with differential diffusivities. Through computational simulations, we analyze the evolution of this instability under various conditions, identifying key parameters such as aspect ratio, particle density, and drift strength that influence the system's stability. While its behavior resembles the Plateau–Rayleigh instability (PRI), the underlying mechanism differs fundamentally, as PRI is restricted to three-dimensional systems. Interestingly, similar instabilities have been observed in chiral fluids, further supporting the existence of a novel instability mechanism unique to two-dimensional non-equilibrium systems. Our results suggest that this phenomenon is not a finite-size effect, but rather an intrinsic property of systems with differential diffusivities, offering new insights into pattern formation and instability dynamics in active matter.

Instabilities are fundamental in fluid dynamics, revealing the mechanisms by which competing forces interact, ultimately allowing one to dominate and drive the system toward a new stable configuration. These dynamic transitions arise when small perturbations within the system grow, disrupting equilibrium and leading the fluid to a different stable state. Given the ubiquity of these processes in nature[1,2] and material science,[3,4] understanding and developing methods to control them has attracted significant interest.[5]

A classic example is the Plateau–Rayleigh instability, which describes the breakup of liquid columns into droplets due to surface tension. This phenomenon provides a foundational understanding of how fluids respond to perturbations[6] and helps identify the key variables governing rupture dynamics of free-surface flows.[7,8] Precise control over these parameters enables the manipulation of factors like breakup time and droplet size, which are critical in technologies and applications that depend on micro-scale fluid behavior.[9,10]

While the PRI is not exclusive to conventional fluids, it also appears in other forms of matter, such as granular media,[11] viscoelastic materials,[12] and solids,[13] in regimes where surface tension dominates over other stabilizing forces. However, the dimensionality (D) of the system imposes a critical constraint on the properties of the instability. Specifically, the threshold wavelength, $\lambda_c = 2\pi R/\sqrt{D-2}$, which determines the length scale of perturbations that grow exponentially and drive the instability, becomes not finite for purely two-dimensional systems ($D = 2$). Consequently, the PRI does not occur in strictly bidimensional configurations.[14]

Nevertheless, instabilities have been observed in two-dimensional channel-like configurations that visually resemble the PRI, most notably in chiral fluids, where fluid strips break up into disc-shaped structures.[15] Similar configurations also emerge during segregation processes in non-equilibrium systems, such as driven liquids[16,17] and certain active matter systems,[18–20] although the rupture dynamics of these instabilities remain largely unexplored. These observations suggest the emergence of a distinct instability mechanism that mimics the PRIs visual characteristics but arises under fundamentally different, non-equilibrium conditions.

Active matter systems provide a natural framework to explore these distinct instabilities. As a unique class of non-equilibrium systems, active matter is characterized by components that locally and independently convert energy into motion,[21] generating continuous energy fluxes and emergent collective behaviors.[22] These behaviors often exhibit pattern formation driven by dynamic forces absent in equilibrium systems.[23,24] A notable example is spontaneous phase segregation in mixtures of particles with differential diffusivities,[25,26] which can be used for investigating how activity-induced instabilities develop within constrained, channel-like geometries.

Systems composed of particles with different diffusivities occur naturally across a wide range of phenomena, including the spatial segregation of chromosomes,[27] phase separation in polymers,[28] enhanced diffusion in enzymes,[29] and dynamic behavior in densely crowded environments relevant to biological processes.[20] Although theoretical analyses using Fokker–Planck methods can predict properties such as internal stress and surface

Departamento de Física, Universidade Federal do Ceará, Fortaleza, Ceará 60451–970, Brazil. E-mail: michael@fisica.ufc.br

tension in the dilute limit,[30] these models often fail to capture the complexities of dense environments and the dynamic behavior of surfaces in unstable configurations—especially the critical role of emergent surface tension. This broad applicability highlights the relevance of differential diffusivity models in understanding instabilities across both biological and synthetic systems.

In this paper, we present a numerical analysis of the rupture dynamics of a channel-like structure in a two-dimensional system composed of particles with different diffusivities. Observations of two-dimensional instabilities in these systems reveal that collective behavior cannot be fully explained by surface tension effects alone, as in the classical PRI framework. Instead, the instability arises from the interplay between differential diffusivity and repulsive interactions, a dynamic that predominates in 2D environments, such as biological processes and active matter systems. The main objective is to identify the key variables governing this instability, using the breakup time—the time at which the system experiences its first rupture—as a quantitative measure of the channel's stability. To achieve this, we perform simulations under various system parameters and analyze their influence on the breakup time. Additionally, we investigate the rupture dynamics by examining the power-law scaling of the channel's minimum width as it approaches the pinching time. This allows us to compare the scaling exponent with previously studied similarity solutions from analyses of rupture phenomena.[31]

We consider a system composed of N particles of radius a, divided into two types that differ solely in their diffusion coefficients, $D_i \in \{D_c, D_h\}$, where D_c and D_h correspond to the diffusion coefficients of the "cold" and "hot" particles, respectively, with $D_c \leq D_h$. The particles interact through short-range, soft repulsive forces described by $\mathbf{F}_{ij} = k(2a - r_{ij})\hat{\mathbf{r}}_{ij}$ if the particles overlap ($r_{ij} < 2a$), and $\mathbf{F}_{ij} = 0$ otherwise. Here, k is the repulsion strength, $r_{ij} = |\mathbf{r}_i - \mathbf{r}_j|$ is the distance between the particle centers, and $\hat{\mathbf{r}}_{ij} = (\mathbf{r}_i - \mathbf{r}_j)/r_{ij}$ is the unit vector along the line of centers. The dynamics of the system are governed by a set of overdamped Langevin equations:[32–34]

$$\dot{\mathbf{r}} = \mu \sum_{j}^{N} \mathbf{F}_{ij} + \eta_i(t), \tag{1}$$

where μ is the inverse of the Stokes coefficient, and $\eta_i(t)$ represents Gaussian white noise with zero mean and unit variance. Specifically, the noise satisfies $\langle \eta_i(t)\eta_j(t)\rangle = 2D_i\delta_{ij}\delta(t - t')$, where the noise magnitude is determined by the diffusion coefficient D_i. We define the simulation units based on characteristic parameters of the system: length is measured in units of particle radius a, time is measured in units of $(\mu k)^{-1}$, and other quantities are derived from these. For example, the diffusion coefficient is expressed in units of $a^2\mu k$. In our simulations, the particle radius a, the repulsion strength k, and the inverse of Stokes coefficient μ are all set to unity.

Initially, the cold particles are arranged in a triangular lattice with lattice constant $2a$, forming a channel structure. The channel width is determined by the number of cold particle layers n_y, and its length by the number of particles n_x, such that

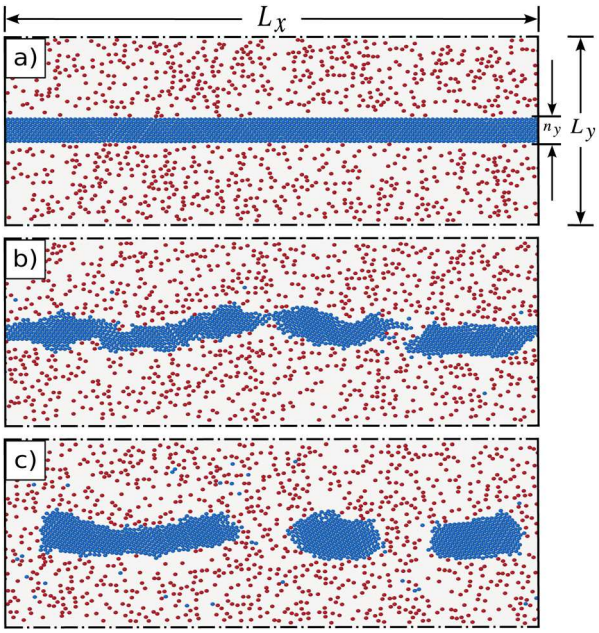

Fig. 1 Snapshots of particle configurations consisting of 960 hot particles (red) and 960 cold particles (blue), with diffusion coefficients $D_h = 5 \times 10^{-3}a^2\mu k$ and $D_c = 0$, respectively. The simulation was performed in a rectangular box of size $L_x = 240a$ and $L_y = 125a$, with a total packing fraction $\phi = N\pi a^2/(L_xL_y) = 0.2$. The solid vertical lines and dot-dashed horizontal lines represent the periodic boundary conditions in L_y and L_x respectively. (a) Initial configuration of the channel, composed of $n_y = 6$ layers of cold particles, with labels indicating the system size. (b) Configuration at the moment when the first channel breakup occurring at $t = 6.4 \times 10^5(\mu k)^{-1}$. (c) Configuration at latter times when the cold particles begin to form droplets at $t = 1.1 \times 10^6(\mu k)^{-1}$.

the total number of cold particles composing the channel is $N_c = n_x \times n_y$. This channel is surrounded by a gas-like phase consisting of N_h hot particles, which are randomly distributed, as shown in Fig. 1(a). All simulations are performed in a rectangular box with periodic boundary conditions along the L_x and L_y directions. eqn (1) is integrated using the Euler method with a discrete time step of $dt = 0.01(\mu k)^{-1}$. To ensure the robustness of our results, we verified that the outcomes remain consistent even when dt is varied by a factor of 10, either larger or smaller (*i.e.*, $dt \in [0.001, 0.1](\mu k)^{-1}$).

The results of the Brownian dynamics simulations reveal that the continuous flux of energy due to the non-persistent activity is transmitted to the channel through particles interactions. This disturbance gradually propagates through the channel, eventually triggering its pinch-off, as shown in Fig. 1. In this case, the breakup is governed by the non-equilibrium interplay between the differing diffusion coefficients and particle interactions, resulting in a self-organized structure that mimics classical fluid instabilities. Interestingly, the same channel geometry has been reported as a stable state under high-density configurations, where it is particularly relevant to cell-sorting phenomena,[20] highlighting the importance of investigating its stability under different conditions. To further explore this, we analyze how the breakup dynamics are influenced by key parameters, including the aspect ratio of the

channel, the diffusivity of the hot particles, the relative density of hot and cold particles, and the addition of a drift term to the cold particles.

Numerically, to determine the breakup time, t_b, we employ the wrapping condition from the Newman–Ziff algorithm,[35] which is particularly well-suited for systems with periodic boundary conditions. This method tracks the percolation state of the cold particle cluster. Two particles are considered part of the same cluster if their center-to-center distance is less than three particle radii, $3a$. Initially, the cluster is in a percolated state across the system. The breakup time is defined as the moment when the wrapping condition[35] is no longer satisfied. This means that a gap of at least one particle radius has formed in the channel, at which point the simulation is terminated. We have verified that using larger gap values does not significantly affect the results for the breakup time.

In Fig. 2, we present the average breakup time, t_b, as a function of the channel length, L_x, for different values of the initial channel width, measured by the number of layers, n_y. Given that the channel width n_y introduces a characteristic scale, we assume that the breakup time follows the scaling relation $t_b = n_y^{\alpha} f(L_x/n_y)$. To determine the value of α, we minimize the sum of the quadratic dispersion of the logarithm of the data for each value of the ratio Lx/ny. Considering only the data for $n_y \geq 6$ (as the narrower channel $n_y = 5$ deviates from the rest), we obtain that $\alpha = 4.91 \pm 0.21$. Since $\alpha = 5$ falls within the error margin, we present the scaled breakup time t_b/n_y^5 in Fig. 2. This scaling relation not only captures the dependence of t_b on both L_x and n_y but also enables us to extrapolate our results to larger system sizes.

We observe, that the average breakup time, t_b, increases as the aspect ratio L_x/n_y decreases. Specifically, a sharp increase in the scaled breakup time t_b/n_y^5 occurs for systems with $L_x/n_y < 30$, indicating that channels with lower aspect ratios are more robust against perturbations induced by hot particles. This behavior is analogous to the PRI,[36] where only perturbations with wavelengths exceeding a critical threshold undergo exponential growth. Our results suggest the existence of a similar threshold length in our system, above which perturbations grow more rapidly.

Interestingly, the system displays a power-law dependence similar to that reported for the rupture of free liquid films, which has been extensively studied in the context of foams and emulsions. In such systems, the breakup time scales as $t_b \sim h_0^5$, where h_0 represents the uniform thickness of the film.[37] A more detailed exploration of this power-law behavior is presented later, focusing on the scaling properties of the minimum channel width and the pinch-off dynamics.

We now examine the case of a jet of cold particles moving with constant drift, rather than a stationary channel. Our goal is to understand how the channel instability is influenced by the addition of a drift term of magnitude v to the cold particles. Fig. 3 illustrates that the drift term significantly enhances the stability, as the breakup time increases exponentially with v. Interestingly, the stabilization effect depends on the length of the channel, with shorter channels showing a faster exponential increase in breakup time compared to longer channels. This suggests that the drift term not only stabilizes the channel but also introduces a length-dependent mechanism that modulates the instability dynamics.

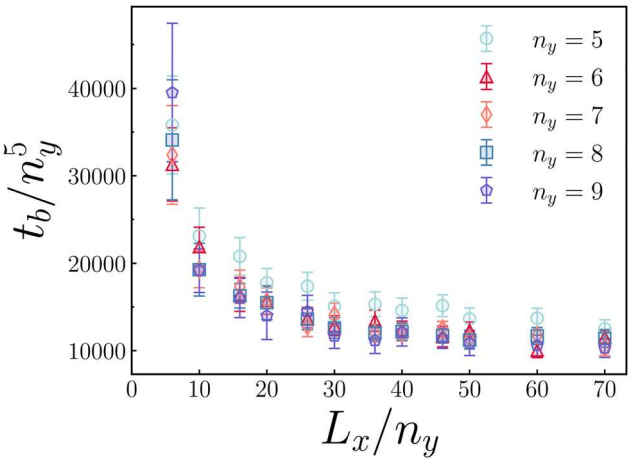

Fig. 2 Average breakup time of the channel, t_b, as a function of the aspect ratio, L_x/n_y, for different channel widths n_y. The diffusion coefficient of the hot particles is set to $D_h = 5 \times 10^{-3} a^2 \mu k$, and the total packing fraction is $\phi = 0.2$. The bars represent one standard deviation over 50 independent simulations. Channels with larger widths ($n_y > 5$) exhibit a strong power-law dependence, $t_b \sim n_y^5$, highlighting the significant influence of channel width on breakup time in this regime. Furthermore, the results suggest the existence of a specific aspect ratio where the system reaches maximum instability, characterized by a sharp decrease in t_b. This implies that at this aspect ratio, external perturbations are most effective in destabilizing the channel.

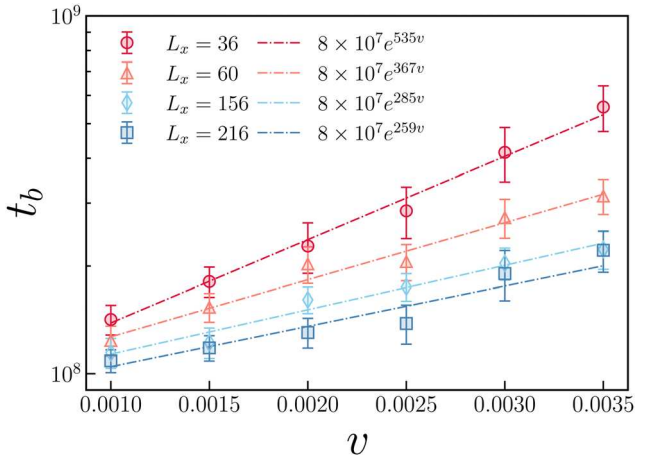

Fig. 3 Average breakup time, t_b, as a function of the drift strength, v, for different channel lengths, L_x. The data is presented on a semi-logarithmic scale. The diffusion coefficient of the hot particles is fixed at $D_h = 5 \times 10^{-3} a^2 \mu k$, the total packing fraction at $\phi = 0.2$, and the channel width at $n_y = 6$. The bars represent one standard deviation over 25 independent simulations, and dashed lines show exponential fits. The results indicate that t_b increases exponentially with drift strength for all L_x, with a more pronounced stabilization effect in shorter channels. This suggests that the drift term counteracts perturbations induced by hot particles, enhancing stability, particularly in shorter channels.

Another crucial factor that significantly influences the rupture dynamics is the number of hot particles, N_h, which serves as a surrogate for the density of the gas-like phase. Since the exact density of the system is difficult to determine due to the undefined excluded area of the cold particles, we use N_h as a control parameter. To explore this, we fix the dimensions of the simulation box and the number of cold particles, N_c, while varying N_h. As shown in Fig. 4, at low concentrations of hot particles (region I), interactions between hot particles and the channel become less frequent, leading to a drastic reduction in surface perturbations. This diminished interaction slows the growth of instabilities at the channel's boundaries, resulting in longer breakup times. Remarkably, the channel still ruptures even at very low number of hot particles, demonstrating the inherent instability of the system.

As N_h increases, the breakup time decreases, reaching its minimum at intermediate densities (central region). This indicates a regime of maximum instability, where the interactions between hot particles and the channel are most effective at driving perturbations. Notably, at high densities (region II), the system displays a re-entrant behavior: the breakup time increases again, signaling a return to a more stable regime. This stabilization arises from the high density of hot particles, which leads to a jamming state that restricts their ability to diffuse freely and interact with the channel. The reduced mobility of the hot particles creates a caging effect, suppressing perturbations and slowing the rupture dynamics.

The rupture dynamics of the channel reveal that the key parameters influencing its stability—aspect ratio, drift, and particle density—affect the breakup time in distinct ways. Among these, particle density is the only parameter with a non-monotonic impact on instability: as the number of hot particles increases, the system transitions from stability to maximum instability before returning to a more stable regime due to a caging effect. In contrast, the aspect ratio defines two distinct instability regions, introducing a critical value that separates stable and unstable configurations. Meanwhile, the drift term consistently enhances the system's stability, causing an exponential increase in breakup time without introducing instability thresholds.

Finally, we analyze the rupture dynamics of the channel by tracking the evolution of its minimum width, w_{min}, as a function of the remaining time until breakup, t_b–t. To achieve this, we construct histograms of the cold particle positions at each time step and binarize the data to determine the channel boundaries using the *contour* function in MATPLOTLIB.[38] For each point along one of the channel boundaries, we compute the perpendicular distance to the opposite boundary. The smallest of these distances is recorded as the minimum width, w_{min}. The time evolution of w_{min}, shown in Fig. 5, reveals that the progressive narrowing of the channel follows a power-law relationship of the form $w_{min} \sim (t_b - t)^{\beta}$, where the exponent is determined to be $\beta = 0.20$.

Given the geometry and the non-equilibrium nature of the system, there is currently no available information regarding the similarity properties of this instability. The lack of analytical results about system properties, such as the determination of surface tension, further complicates direct comparisons with other known results. This contrasts with the well-studied phenomena like the PRI, where the exponent β provides valuable insights into the dominant forces driving the pinch-off process. For instance, in the PRI, different regimes—such as stochastic, diffusive or viscous—result in distinct values of β, reflecting the underlying force balance.[31]

In the context of rupture dynamics, the exponent $\beta = 0.20$ has been previously reported in the temporal power-law behavior of the thickness during the rupture of thin liquid films, where van der Waals forces dominate the thinning process.[39] However, our system represents a fundamentally different case, both in terms of dimensionality and the underlying driving

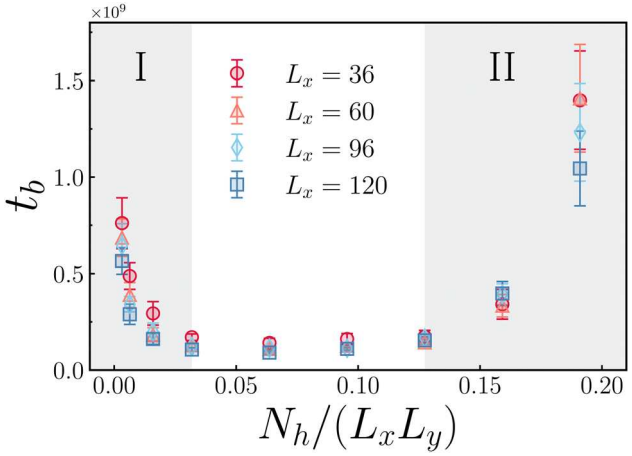

Fig. 4 Average breakup time of the channel, t_b, as a function of the number of hot particles, N_h, for different channel lengths, L_x. The simulations were performed in a rectangular box of width $L_y = 94.25a$ and channel width of $n_y = 6$. The system exhibits a region of maximum instability at intermediate densities, flanked by two more stable regions, represented by the shaded areas I and II.

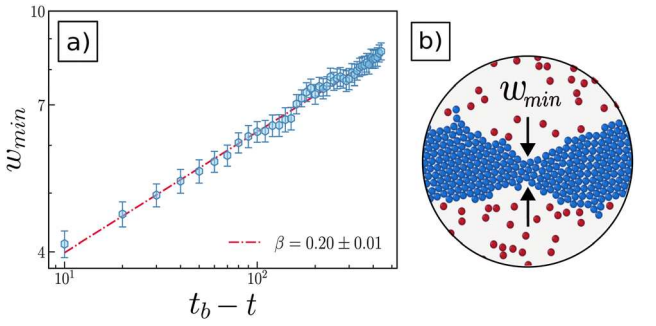

Fig. 5 (a) Minimum channel width, w_{min}, as a function of the time until breakup, $(t_b - t)$. The data is presented on a log–log scale. Simulations were performed in a rectangular box with dimensions $L_x = 300a$ and $L_y = 157a$, using $N_h = N_c = 1500$ particles and a total packing fraction of $\phi = 0.2$. The initial channel width was $n_y = 10$, and the diffusion coefficient of the hot particles was fixed at $D_h = 5 \times 10^{-3} a^2 \mu k$. The results show that w_{min} decreases over time following a power-law scaling, $w_{min} \sim (t_b - t)^{\beta}$, with an exponent $\beta = 0.20 \pm 0.20$ (dashed line). This scaling exponent suggests a novel similarity regime with no counterpart in passive systems. The bars represent the standard deviation over 40 independent samples. (b) Schematic of w_{min} for one sample approaching the breakup time.

mechanisms. In contrast, the observed $\beta = 0.20$ in our system suggests the emergence of a novel scaling regime. Unlike passive systems, where well-defined forces like surface tension or van der Waals interactions govern the dynamics, the instability in this active system appears to emerge from collective effects driven by pronounced differences in diffusivity between the particle species.

In this paper, we investigated a novel instability mechanism in a two-dimensional active binary mixture of particles with differential diffusivity. This mechanism is fundamentally distinct from rupture phenomena observed in passive systems. While the observed channel breakup and the formation of droplet-like structures resemble the PRI, the underlying mechanism is significantly different: PRI is inherently three-dimensional and governed by surface tension, whereas our system operates in strictly two-dimensional, non-equilibrium conditions. Remarkably, despite the absence of cohesive forces like surface tension, the interplay between differential diffusivity and repulsive interactions generates an effective destabilizing mechanism that drives rupture.

Through numerical simulations, we identified key parameters—such as aspect ratio, drift strength, and particle density—that govern the breakup dynamics of the channel. We demonstrated that introducing a unidirectional drift to the channel particles enhances stability by counteracting the growth of surface perturbations, a concept of great interest in active microfluidics.[40,41] A central finding is the re-entrant behavior of instability regimes as the number of ''hot'' particles increases, driven by the interplay between differential diffusivity and kinetic confinement effects, such as jamming at high densities. This behavior is particularly relevant to biological processes like cell sorting, where similar mechanisms influence structure formation and segregation.[20,42,43] Furthermore, our results reveal a power-law scaling behavior for the minimum channel width, $w_{\min} \sim (t_b - t)^{\beta}$, with an exponent $\beta = 0.20$. This scaling, along with the identification of a threshold aspect ratio, provides a new framework for analyzing interface dynamics in two-dimensional active matter. These findings provide insights into pattern formation and instability mechanisms that are unique to non-equilibrium systems.

The methodology developed in this study, combining Brownian dynamics simulations with percolation-based techniques, not only quantifies the stability of active surfaces but also establishes a reproducible framework for investigating interface dynamics under diverse geometries and conditions.[44,45] This approach opens new avenues for exploring effective properties of active systems, such as emergent surface tension, interface roughness, and responses to external perturbations.[17,46] Furthermore, the framework can be generalized to higher-dimensional systems, offering a pathway to deepen our understanding of active matter instabilities and their role in non-equilibrium phase transitions.

Author contributions

All authors contributed to the conceptualization of the study, the development of the numerical investigation, and the analysis of the results. M. T. R., M. C. G., and A. A. M. designed and implemented the computer codes. M. T. R. prepared the original draft, and all authors participated in its critical revision and approved the final manuscript.

Data availability

No new data were generated in this study. This article is based on theoretical analyses and simulations described in the main text and references therein.

Conflicts of interest

There are no conflicts to declare.

Acknowledgements

We thank the Brazilian agencies CNPq, CAPES and FUNCAP, and the National Institute of Science and Technology for Complex Systems (INCT-SC) in Brazil for financial support.

Notes and references

1 C. Fei, S. Mao, J. Yan, R. Alert, H. A. Stone, B. L. Bassler, N. S. Wingreen and A. Košmrlj, *Proc. Natl. Acad. Sci.*, 2020, **117**, 7622–7632.
2 A. Martínez-Calvo, T. Bhattacharjee, R. K. Bay, H. N. Luu, A. M. Hancock, N. S. Wingreen and S. S. Datta, *Proc. Natl. Acad. Sci.*, 2022, **119**, e2208019119.
3 D. Lohse, *Annu. Rev. Fluid Mech.*, 2022, **54**, 349–382.
4 R. V. Craster and O. K. Matar, *Rev. Mod. Phys.*, 2009, **81**, 1131–1198.
5 J. Porter, P. Salgado Sánchez, V. Shevtsova and V. Yasnou, *Math. Model. Nat. Phenom.*, 2021, **16**, 24.
6 R. Mead-Hunter, A. J. C. King and B. J. Mullins, *Langmuir*, 2012, **28**, 6731–6735.
7 M. Moseler and U. Landman, *Science*, 2000, **289**, 1165–1169.
8 M. L. Eggersdorfer, H. Seybold, A. Ofner, D. A. Weitz and A. R. Studart, *Proc. Natl. Acad. Sci.*, 2018, **115**, 9479–9484.
9 B. Derby, *Annu. Rev. Mater. Res.*, 2010, **40**, 395–414.
10 J. Eggers and E. Villermaux, *Rep. Prog. Phys.*, 2008, **71**, 036601.
11 G. Prado, Y. Amarouchene and H. Kellay, *Phys. Rev. Lett.*, 2011, **106**, 198001.
12 S. I. Tamim and J. B. Bostwick, *Soft Matter*, 2021, **17**, 4170–4179.
13 C. Xuan and J. Biggins, *Phys. Rev. E*, 2017, **95**, 053106.
14 V. Cardoso and O. J. C. Dias, *Phys. Rev. Lett.*, 2006, **96**, 181601.
15 V. Soni, E. S. Bililign, S. Magkiriadou, S. Sacanna, D. Bartolo, M. J. Shelley and W. T. Irvine, *Nat. Phys.*, 2019, **15**, 1188–1194.
16 C. del Junco, L. Tociu and S. Vaikuntanathan, *Proc. Natl. Acad. Sci.*, 2018, **115**, 3569–3574.
17 C. del Junco and S. Vaikuntanathan, *J. Chem. Phys.*, 2019, **150**, 094708.

18 S. Kumari, A. S. Nunes, N. A. M. Araújo and M. M. Telo da Gama, *J. Chem. Phys.*, 2017, **147**, 174702.
19 B.-Q. Ai, B.-Y. Zhou and X.-m Zhang, *Soft Matter*, 2020, **16**, 4710–4717.
20 E. McCarthy, R. K. Manna, O. Damavandi and M. L. Manning, *Phys. Rev. Lett.*, 2024, **132**, 098301.
21 G. Gompper, R. G. Winkler, T. Speck, A. Solon, C. Nardini, F. Peruani, H. Löwen, R. Golestanian, U. B. Kaupp, L. Alvarez, T. Kiørboe, E. Lauga, W. C. K. Poon, A. DeSimone, S. Muiños-Landin, A. Fischer, N. A. Söker, F. Cichos, R. Kapral, P. Gaspard, M. Ripoll, F. Sagues, A. Doostmohammadi, J. M. Yeomans, I. S. Aranson, C. Bechinger, H. Stark, C. K. Hemelrijk, F. J. Nedelec, T. Sarkar, T. Aryaksama, M. Lacroix, G. Duclos, V. Yashunsky, P. Silberzan, M. Arroyo and S. Kale, *J. Phys.: Condens. Matter*, 2020, **32**, 193001.
22 B. Liebchen and H. Löwen, *Acc. Chem. Res.*, 2018, **51**, 2982–2990.
23 P. Romanczuk, M. Bär, W. Ebeling, B. Lindner and L. Schimansky-Geier, *Eur. Phys. J. Special Topics*, 2012, **202**, 1–162.
24 T. Speck, *Soft Matter*, 2020, **16**, 2652–2663.
25 S. N. Weber, C. A. Weber and E. Frey, *Phys. Rev. Lett.*, 2016, **116**, 058301.
26 A. Y. Grosberg and J.-F. Joanny, *Phys. Rev. E*, 2015, **92**, 032118.
27 N. Ganai, S. Sengupta and G. I. Menon, *Nucleic Acids Res.*, 2014, **42**, 4145–4159.
28 J. Smrek and K. Kremer, *Phys. Rev. Lett.*, 2017, **118**, 098002.
29 M. Xu, J. L. Ross, L. Valdez and A. Sen, *Phys. Rev. Lett.*, 2019, **123**, 128101.
30 E. Ilker and J.-F. M. C. Joanny, *Phys. Rev. Res*, 2020, **2**, 023200.
31 B. Barker, J. B. Bell and A. L. Garcia, *Proc. Natl. Acad. Sci.*, 2023, **120**, e2306088120.
32 J. S. Andrade, G. F. T. da Silva, A. A. Moreira, F. D. Nobre and E. M. F. Curado, *Phys. Rev. Lett.*, 2010, **105**, 260601.
33 P. Barrozo, A. A. Moreira, J. A. Aguiar and J. S. Andrade, *Phys. Rev. B: Condens. Matter Mater. Phys.*, 2009, **80**, 104513.
34 A. A. Moreira, C. M. Vieira, H. A. Carmona, J. S. Andrade and C. Tsallis, *Phys. Rev. E*, 2018, **98**, 032138.
35 M. E. J. Newman and R. M. Ziff, *Phys. Rev. E*, 2001, **64**, 016706.
36 C. Zhao, J. E. Sprittles and D. A. Lockerby, *J. Fluid Mech.*, 2019, **861**, R3.
37 A. Vrij, *Discuss. Faraday Soc.*, 1966, **42**, 23–33.
38 J. D. Hunter, *Comput. Sci. Eng.*, 2007, **9**, 90–95.
39 C. Zhao, J. Liu, D. A. Lockerby and J. E. Sprittles, *Phys. Rev. Fluids*, 2022, **7**, 024203.
40 S. Chandragiri, A. Doostmohammadi, J. M. Yeomans and S. P. Thampi, *Soft Matter*, 2019, **15**, 1597–1604.
41 K. Patel and H. Stark, *Soft Matter*, 2023, **19**, 2241–2253.
42 J. Rozman and J. M. Yeomans, *Phys. Rev. Lett.*, 2024, **133**, 248401.
43 K. Mondal, P. Bera and P. Ghosh, *J. Chem. Phys.*, 2024, **161**, 50.
44 L. Langford and A. K. Omar, *Phys. Rev. E*, 2024, **110**, 054604.
45 H. Yue, C. R. Packard and D. M. Sussman, *Soft Matter*, 2024, **20**, 9444–9453.
46 M. Nguyen, Y. Qiu and S. Vaikuntanathan, *Annu. Rev. Condens. Matter Phys.*, 2021, **12**, 273–290.

APPENDIX B - OTHER WORKS

- The first work is an article [146] published in **EPL (Europhysics Letters)**. It presents the initial result of the PhD and offers a theoretical framework to derive the screening term used to model diatomic molecules from first principles. The study is carried out within a deformed space formalism and provides analytical insight into the central force problem under modified spatial geometries.
- The second work is currently in preparation and focuses on the application of the generalized extended momentum operator in quantum mechanics. In this work, we connect classical quantum potentials to their analogs in (anti-)de Sitter spacetimes, and we derive a general expression that unifies hyperbolic potentials such as the Pöschl–Teller and Rosen–Morse types.

A Letters Journal Exploring the Frontiers of Physics

May 2022

EPL, **138** (2022) 40001
doi: 10.1209/0295-5075/ac6f7c

www.epljournal.org

Screening potentials derived from the central force problem in a deformed space

Michael T. Ramirez[(a)], José S. Andrade jr.[(b)] and André A. Moreira[(c)]

Departamento de Física, Universidade Federal do Ceará - Caixa Postal 6030, Campus do Pici, 60455-760 Fortaleza, Ceará, Brazil

received 15 February 2022; accepted in final form 13 May 2022
published online 8 June 2022

Abstract – The action of long-range potentials can be hindered by the collective effect of free charges in a medium, a process dubbed screening. This effect is usually modeled by adding an exponential crossover to a power-law potential. We show here how these exponential cutoffs can be obtained from first principles in the central force problem through the addition of a radial deformation of space, $\nabla_\eta = (1+\gamma r)\nabla_r$. When considering a potential in the form $V = -(K_1/r + K_2/r^2)$, we find that the radial part of the Schrödinger equation displays an effective potential that takes the form of two well-known screening potentials, namely, the Eckart and the Manning-Rosen potentials.

Quite often, elements interacting via long-range potentials have the resulting force being dampened by the screening action of free charges in the background. Such screening effects are relevant in the physics of plasmas [1,2], in the description of molecular interactions [3,4], and in determining the nuclear energy of different isotopes [5], among other cases. A complete description of the screening process should depend on the treatment of the N-body problem [6]. To circumvent this complication, it has been proposed that the collective effect of the background can be modeled by effective exponential-type potentials [7–9] such as

$$V_n(r;\lambda,A,B) = A\frac{e^{-r/\lambda}}{e^{-r/\lambda}-1} + B\frac{(e^{-r/\lambda})^n}{(e^{-r/\lambda}-1)^2}. \qquad (1)$$

Figure 1 shows that the terms in (1) follow power-laws near the origin and then crossover to exponential cutoffs. The case $n = 2$ of eq. (1) corresponds to the Manning-Rosen potential that was initially proposed to describe the interaction of diatomic molecules [10]. This potential has been used to describe optical properties in spherical quantum dots [11] and pseudo-spin symmetry in nuclear physics [12]. It has also motivated approximation techniques for the solution of the Schrödinger equation for central potentials with angular momentum $L^2 > 0$. The bound state and scattering properties of this potential have been investigated using different techniques as, for example, the differential equation approach [13], asymptotic iteration method (AIM) [14], the Pekeris-type approximation [15], and the Nikiforov-Uvarov (NU) method [16].

The case $n = 1$ of eq. (1) corresponds to the Eckart potential [17], widely applied in physics [18,19] and chemical physics [20,21]. The s-wave solutions of the Schrödinger and Dirac equations with Eckart potential have been studied to obtain the bound states [22,23], while the ℓ-wave case has been studied using approximation methods for the centrifugal term [24]. Both the Eckart and Manning-Rosen potentials reduce to the Hulthén potential [25] for $B = 0$.

Behaving like the Coulomb potential near the origin and asymptotically decreasing like an exponential, the Hulthén potential has been developed to describe screening phenomena for short-range interactions in nuclear and particle physics [26], atomic physics [27], solid state physics [28] and chemical physics [29]. In addition, the bound states and scattering solutions of the Schrödinger equation with the Hulthén potential have been investigated through a variety of techniques [30–32].

Since both Eckart and Manning-Rosen are radial potentials, probably the forms of these potential for $r/\lambda < 0$ has not been of much concern. Here, however, we will make use of the fact that, considering a negative screening length $\lambda < 0$, and neglecting a shift in the potential,

[(a)] E-mail: michael@fisica.ufc.br (corresponding author)
[(b)] E-mail: soares@fisica.ufc.br
[(c)] E-mail: auto@fisica.ufc.br

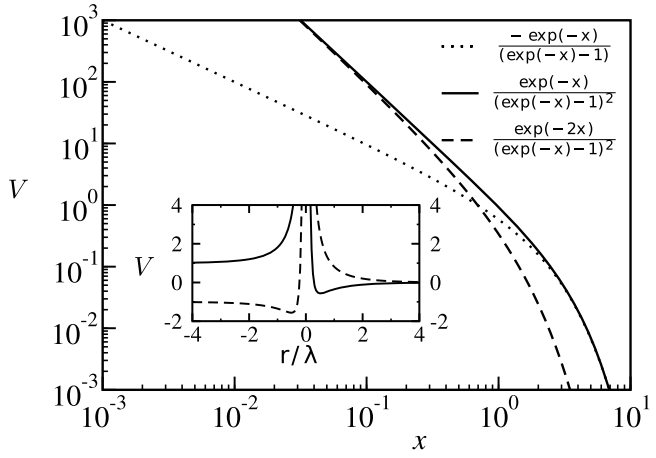

Fig. 1: The terms of the screened potentials defined in eq. (1). The term $\exp(-x)/(\exp(-x)-1)$ is a deformation of the attractive Coulomb potential, diverging at the origin as $-1/x$, then crossing over to an exponential cutoff. The term $\exp(-nx))/(\exp(-x)-1)^2$ diverges as $1/x^2$ at the origin, and also presents exponential cutoffs at different scales. On the inset, the potentials defined in eq. (1). The straight line represents the Eckart potential ($n=1$), with $A=1$ and $B=1/4$, while the dashed line represents the Manning-Rosen potential ($n=2$), with $A=-5/4$ and $B=1/4$. Note that, as indicated in eq. (2), disregarding a shift the negative region of one case mirrors the positive region of the other.

the Manning-Rosen potential ($n=2$) can be identified with the Eckart potential ($n=1$), and vice versa. That is, as illustrated in the inset of fig. 1, the cases $n=1$ and 2 in eq. (1) can be mapped one onto the other,

$$V_1(r;\lambda,A,B) = V_2(r;-\lambda,-(A+B),B) + A. \quad (2)$$

In a previous work [33], it was shown that when a harmonic potential is defined around a contracted region of a deformed space, the resulting effective interaction takes the form of the Morse potential [34]; in this way revealing a hidden correspondence between these two physical problems. In the same vein, here we show how two different screening potential models can also be related, through a similar space distortion, to a fundamental problem in physics, namely, the central force problem.

The central force problem is a leading problem in the development of physics. In the twentieth century, quantum solutions of central force models have been employed to describe the hydrogen atom [35], transition metals [36], and utilized to perform perturbation calculations in atomic and nuclear physics [37,38].

The Eckart and Manning-Rosen potentials are model descriptions of the effective radial interaction within a screening medium. In these models, both the Coulomb-like $1/r$ interaction, as well as the $1/r^2$ effective term due to angular momentum conservation, are deformed by an exponential cutoff. This cutoff is tailored to account for exchange of linear and angular momentum with the medium. This leads us to question whether a similar cutoff effect could be obtained by employing a spatial deformation. To test this hypothesis we investigate the three-dimensional generalization of the deformed space in spherical coordinates, and how the central force problem is changed by the introduction of a radial space deformation [39] into the translation operator $\hat{\tau}_\gamma$, resulting in non-additive displacements, and leading to a deformed generator of spatial translations,

$$\hat{p}_\gamma = -i\hbar D_\gamma, \quad (3)$$

where $D_\gamma \equiv (1+\gamma r)\mathrm{d}/\mathrm{d}r$ is a deformed derivative in space. The deformation parameter γ has the dimension of inverse of length and relates to the metric tensor of the dilated/contracted space [40]. This kind of deformed momentum operator has been used to describe systems with effective mass dependent on position in the quantum formalism [41–46]. In addition, it leads to a modified uncertainty relation, which has serious implications in the fields of generalized uncertainty principle [40,43,47] and curved spaces [48].

A natural generalization of the deformed momentum in three-dimensional spherical coordinates can be written as

$$\hat{P}_\gamma = -i\hbar f_\gamma(r,\theta,\phi)\nabla = -i\hbar\nabla_\gamma, \quad (4)$$

where $f_\gamma(r,\theta,\phi)$ is the deformation. In this work, we constrain the problem to a radial deformation $f_\gamma(r)$, so that the Schrödinger equation can be written as

$$i\hbar\frac{\partial}{\partial t}\psi(\mathbf{r}) = -\frac{\hbar^2}{2m}f_\gamma(r)\nabla f_\gamma(r)\nabla\psi(\mathbf{r}) + V(r)\psi(\mathbf{r}), \quad (5)$$

where, to preserve the spherical symmetry, we are restricting our approach to the case of radial potentials $V \equiv V(r)$. Since the deformation also acts only in the radial direction, eq. (5) is separable, and the wave function can be written as

$$\psi(\mathbf{r}) = \psi(r,\theta,\varphi) = R(r)Y_{\ell m}(\theta,\varphi), \quad (6)$$

where $Y_{\ell m}(\theta,\varphi)$ are the spherical harmonics.

Using the fact that $\psi(r,\theta,\varphi)$ is an eigenfunction of $\hat{L}^2$ with eigenvalue $L^2 = \ell(\ell+1)\hbar^2$, we obtain the radial differential equation

$$ER(r) = -\frac{\hbar^2}{2m}\left(f_\gamma^2(r)\left(\frac{\mathrm{d}}{\mathrm{d}r}+\frac{2}{r}\right) + f_\gamma(r)f_\gamma'(r)\right)\frac{\mathrm{d}}{\mathrm{d}r}R(r) + \left(\frac{f_\gamma^2(r)L^2}{2mr^2} + V(r)\right)R(r). \quad (7)$$

A common way to tackle the radial part of the Schrödinger equation is to define $Q(r) = rR(r)$, which leads to

$$EQ(r) = \left[V_{\mathrm{eff}}(r) - \frac{\hbar^2}{2m}\left(f_\gamma^2(r)\frac{\mathrm{d}^2}{\mathrm{d}r^2} + f_\gamma(r)f_\gamma'(r)\frac{\mathrm{d}}{\mathrm{d}r}\right)\right]Q(r), \quad (8)$$

where

$$V_{\text{eff}}(r) = \frac{L^2}{2m}\left(\frac{f_\gamma(r)}{r}\right)^2 + \frac{\hbar^2}{2m}\left(\frac{f_\gamma(r)f'_\gamma(r)}{r}\right) + V(r). \tag{9}$$

We see that two terms are added to the effective potential. The first term, proportional to $(f_\gamma/r)^2$, is due to angular momentum conservation, and vanishes when $L^2 = 0$. The second term, proportional to $f_\gamma f'_\gamma/r$, vanishes when f_γ is a constant, which corresponds to an undeformed space. Finally, defining η, where $(\mathrm{d}/\mathrm{d}\eta) = f_\gamma(r)(\mathrm{d}/\mathrm{d}r)$, we obtain a more familiar version of the time-independent Schrödinger equation in one dimension,

$$EQ(\eta) = -\frac{\hbar^2}{2m}\frac{\mathrm{d}^2Q(\eta)}{\mathrm{d}\eta^2} + V_{\text{eff}}(\eta)Q(\eta), \tag{10}$$

with $Q(\eta) \equiv Q(r(\eta))$ and $V_{\text{eff}}(\eta) \equiv V_{\text{eff}}(r(\eta))$.

Now we focus on a particular form of distortion, $\eta = \ln(1+\gamma r)/\gamma$, or $r = (e^{\gamma\eta}-1)/\gamma$. In this case, we have $f_\gamma(r) = (1+\gamma r) = e^{\gamma\eta}$, and our effective potential takes the form

$$V_{\text{eff}}(\eta) = \gamma^2\left(\frac{\hbar^2}{2m}\frac{e^{\gamma\eta}}{e^{\gamma\eta}-1} + \frac{L^2}{2m}\frac{e^{2\gamma\eta}}{(e^{\gamma\eta}-1)^2}\right) + V(\eta), \tag{11}$$

with $V(\eta) \equiv V(r(\eta))$.

Surprisingly, even considering that the external potential vanishes, $V(\eta) = 0$, we have an interesting form for the effective potential, $V_{\text{eff}}(\eta)$. In fact, considering $\gamma < 0$, we notice that $V_{\text{eff}} - V$ takes the form of the Manning potential, $n = 2$ in eq. (1), with $\lambda = -1/\gamma$, $A = \frac{\hbar^2\gamma^2}{2m}$, and $B = \frac{L^2\gamma^2}{2m}$. It should be noted that this effective potential has the same mathematical form of one of the Pekeris approximations proposed in [49] to deal with the centrifugal term for exponential-type potentials.

Considering the case $\gamma > 0$, one should also note that, when $\eta \to \infty$, $V_{\text{eff}}(\eta) - V$ does not tend to zero but rather to $V_\infty = \frac{(L^2+\hbar^2)\gamma^2}{2m}$. However, making use of eq. (2) and eq. (11), we identify $V_{\text{eff}} - V - V_\infty$ as the Eckart potential, $n = 1$ in eq. (1), with $\lambda = 1/\gamma$, $A = -\frac{(L^2+\hbar^2)\gamma^2}{2m}$, and $B = \frac{\gamma^2L^2}{2m}$.

Next, we investigate cases where $V(r(\eta)) \neq 0$. In particular, we will deal with the case of a potential in the form

$$V(r) = -\frac{K_1}{r} - \frac{K_2}{r^2}, \tag{12}$$

that can be written in terms of η as

$$V(\eta) = K1\gamma\frac{e^{-\gamma\eta}}{e^{-\gamma\eta}-1} - K_2\gamma^2\frac{e^{-2\gamma\eta}}{(e^{-\gamma\eta}-1)^2}. \tag{13}$$

When $\gamma > 0$, eq. (13) is associated with the Manning-Rosen potential, $n = 2$ in eq. (1), with $\lambda = 1/\gamma$. On the other hand, when $\gamma < 0$, we again use eq. (2) to show that, in this case, $V(\eta) - K_1\gamma + K_2\gamma^2$ can be associated with the Eckart potential, $n = 1$ in eq. (1), with $\lambda = -1/\gamma$ $A = -K1\gamma + K_2\gamma^2$, and $B = -K_2\gamma^2$. As a consequence, the effective potential V_{eff} and the external potential V will always take the form of the Eckart and Manning-Rosen potentials. Summarizing, for $\gamma > 0$ we have

$$V_{\text{eff}}(\eta) = \frac{(L^2+\hbar^2)\gamma^2}{2m} + V_1\left(\eta; 1/\gamma, -\frac{(L^2+\hbar^2)\gamma^2}{2m}, \frac{L^2\gamma^2}{2m}\right) + V_2\left(\eta; 1/\gamma, K_1\gamma, -K_2\gamma^2\right), \tag{14}$$

while for $\gamma < 0$ we have

$$V_{\text{eff}}(\eta) = -K_1|\gamma| - K_2\gamma^2 + V_2\left(\eta; 1/|\gamma|, \frac{\hbar^2\gamma^2}{2m}, \frac{L^2\gamma^2}{2m}\right) + V_1\left(\eta; 1/|\gamma|, K_1|\gamma| + K_2\gamma^2, -K_2\gamma^2\right). \tag{15}$$

Considering that $K_2 = 0$, we have, for $\gamma > 0$,

$$V_{\text{eff}}(\eta) = \frac{(L^2+\hbar^2)\gamma^2}{2m} + V_1\left(\eta; 1/\gamma, -\frac{(L^2+\hbar^2)\gamma^2}{2m} + K_1\gamma, \frac{L^2\gamma^2}{2m}\right), \tag{16}$$

and for $\gamma < 0$ we have

$$V_{\text{eff}}(\eta) = -K_1|\gamma| + V_2\left(\eta; 1/|\gamma|, \frac{\hbar^2\gamma^2}{2m} + K_1|\gamma|, \frac{L^2\gamma^2}{2m}\right). \tag{17}$$

Note that the first term in both V_1 and V_2, from eq. (1), will be *attractive* as long as $A > 0$, while the second term of both potentials models will be *repulsive* as long as $B > 0$. The occurence of bounded states demand that the two terms act in opposition, with both A and B positive. Looking at eqs. (16) and (17), we see that, when $\gamma > 0$, a bounded state implies the condition $K_1 > \frac{(L^2+\hbar^2)\gamma}{2m}$. On the other hand, when $\gamma < 0$, bound states depend on $K_1 > -\frac{\hbar^2|\gamma|}{2m}$. In this last case, due to the space deformation, bound states may be observed even considering a repulsive potential in the deformed space, $K_1 < 0$.

In conclusion, we have shown a solution of the Schrödinger equation in a radially symmetrical deformed space. Even considering no external potentials, $V = 0$, the radial part of the Schrödinger equation reveals two terms of effective potential. One of these terms is due to the conservation of angular momentum, while the other is due to the form of the distorted space, and will not be present in an undeformed frame. Considering a deformation of the translation operator described as $\nabla_\eta = (1+\gamma r)\nabla_r$, we were able to relate these two terms of the effective potential to the Eckart and Manning-Rosen potentials, for $\gamma > 0$ and $\gamma < 0$, respectively. Curiously, in the radially deformed space, when considering a central potential as a sum of two inverse power laws, $V = -(K_1/r + K_2/r^2)$, we observe that, in the case of the undeformed space, the central potential also takes the form of the Eckart and Manning-Rosen potentials, two well-known potentials that have been frequently used to describe screening effects.

* * *

We thank the Brazilian agencies CNPq, CAPES and FUNCAP, and the National Institute of Science and Technology for Complex Systems (INCT-SC) in Brazil for financial support.

Data availability statement: No new data were created or analysed in this study.

REFERENCES

[1] Ichimaru S., *Basic Principles of Plasma Physics: A Statistical Approach* (CRC Press) 2018.
[2] Soylu A., *Phys. Plasmas*, **19** (2012) 072701.
[3] Simonson T. and Brooks C. L., *J. Am. Chem. Soc.*, **118** (1996) 8452.
[4] Keblinski P., Eggebrecht J., Wolf D. and Phillpot S., *J. Chem. Phys.*, **113** (2000) 282.
[5] Engstler S., Raimann G., Angulo C., Greife U., Rolfs C., Schröder U., Somorjai E., Kirch B. and Langanke K., *Z. Phys. A*, **342** (1992) 471.
[6] Escande D., Doveil F. and Elskens Y., *Plasma Phys. Control. Fusion*, **58** (2015) 014040.
[7] Varshni Y., *Phys. Rev. A*, **41** (1990) 4682.
[8] Roy A. K., *Mod. Phys. Lett. A*, **29** (2014) 1450042.
[9] Dong S., Sun G.-H. and Dong S.-H., *Int. J. Mod. Phys. E*, **22** (2013) 1350036.
[10] Manning M. F. and Rosen N., *Phys. Rev.*, **44** (1933) 951.
[11] Onyeaju M., Idiodi J., Ikot A., Solaimani M. and Hassanabadi H., *J. Opt.*, **46** (2017) 254.
[12] Yanar H. and Havare A., *Adv. High Energy Phys.*, **2015** (2015) 915796.
[13] Khirali B., Behera A., Bhoi J. and Laha U., *J. Phys. G: Nucl. Part. Phys.*, **46** (2019) 115104.
[14] Falaye B., Oyewumi K., Ibrahim T., Punyasena M. and Onate C., *Can. J. Phys.*, **91** (2013) 98.
[15] Wei G.-F. and Dong S.-H., *Phys. Lett. B*, **686** (2010) 288.
[16] Ikhdair Sameer M., *International Scholarly Research Notices*, **2012** (2012) 201525.
[17] Eckart C., *Phys. Rev.*, **35** (1930) 1303.
[18] Onate C., Okoro J., Adebimpe O. and Lukman A., *Results Phys.*, **10** (2018) 406.
[19] Brown R., *J. Res. Natl. Bur. Stand.*, **86** (1981) 357.
[20] Weiss J. J., *J. Chem. Phys.*, **41** (1964) 1120.
[21] Cimas A., Aschi M., Barrientos C., Rayón V., Sordo J. and Largo A., *Chem. Phys. Lett.*, **374** (2003) 594.
[22] Dong S.-H., Qiang W.-C., Sun G.-H. and Bezerra V., *J. Phys. A: Math. Theor.*, **40** (2007) 10535.
[23] Wei G.-F., Long C.-Y., Duan X.-Y. and Dong S.-H., *Phys. Scr.*, **77** (2008) 035001.
[24] Chen C.-Y., Sun D.-S. and Lu F.-L., *J. Phys. A: Math. Theor.*, **41** (2008) 035302.
[25] Hulthén L., *Ark. Mat. Astron. Fys. A*, **28** (1942) 1.
[26] Laha U. and Bhoi J., *Phys. At. Nucl.*, **79** (2016) 62.
[27] Lam C. and Varshni Y., *Phys. Rev. A*, **4** (1971) 1875.
[28] Berezin A., *Phys. Status Solidi (b)*, **50** (1972) 71.
[29] Pyykkö P. and Jokisaari J., *Chem. Phys.*, **10** (1975) 293.
[30] Ahmadov H., Jafarzade S. I. and Qocayeva M., *Int. J. Mod. Phys. A*, **30** (2015) 1550193.
[31] Gönül B., Özer O., Cançelik Y. and Koçak M., *Phys. Lett. A*, **275** (2000) 238.
[32] Bayrak O., Kocak G. and Boztosun I., *J. Phys. A: Math. Gen.*, **39** (2006) 11521.
[33] Costa Filho R. N., Alencar G., Skagerstam B.-S. and Andrade J. S. jr., *EPL*, **101** (2013) 10009.
[34] Morse P. M., *Phys. Rev.*, **34** (1929) 57.
[35] Mills R. L., *Int. J. Hydrog. Energy*, **25** (2000) 1171.
[36] Moriarty J. A., *Phys. Rev. B*, **42** (1990) 1609.
[37] Heyde K. L., *The Nuclear Shell Model* (Springer) 1994, pp. 58–154.
[38] Otsuka T., *Phys. Scr.*, **2013** (2013) 014007.
[39] Costa Filho R., Almeida M., Farias G. and Andrade J. S. jr., *Phys. Rev. A*, **84** (2011) 050102.
[40] Costa Filho R. N., Braga J. P., Lira J. H. and Andrade J. S. jr., *Phys. Lett. B*, **755** (2016) 367.
[41] Barbagiovanni E. and Costa Filho R., *Phys. E: Low-Dimens. Syst. Nanostruct.*, **63** (2014) 14.
[42] da Costa B. G., Gomez I. S. and Portesi M., *J. Math. Phys.*, **61** (2020) 082105.
[43] da Costa B. G., da Silva G. A. and Gomez I. S., *J. Math. Phys.*, **62** (2021) 092101.
[44] da Costa B. G. and Borges E. P., *J. Math. Phys.*, **59** (2018) 042101.
[45] da Costa B. G., Gomez I. S. and Borges E. P., *Phys. Rev. E*, **102** (2020) 062105.
[46] Aguiar V., Cunha S., da Costa D. and Costa Filho R. N., *Phys. Rev. B*, **102** (2020) 235404.
[47] Costa Filho R. N., Oliveira S., Aguiar V. and da Costa D., *Phys. E: Low-Dimens. Syst. Nanostruct.*, **129** (2021) 114639.
[48] Quesne C. and Tkachuk V., *J. Phys. A: Math. Gen.*, **37** (2004) 4267.
[49] Qiang W.-C., Li K. and Chen W.-L., *J. Phys. A: Math. Theor.*, **42** (2009) 205306.

Emergence of Hyperbolic Potentials in Deformed Quantum Spaces

Michael T. Ramirez,* José S. de Andrade Jr.,† and André A. Moreira‡
Departamento de Física, Universidade Federal do Ceará,
Caixa Postal 6030, Campus do Pici, 60455-760 Fortaleza, Ceará, Brazil

Using the formalism of the non-additive translation operator, we establish a direct connection between hyperbolic potentials and fundamental potentials commonly encountered in physics, such as the harmonic and Coulomb potentials. Starting from the one-dimensional case, we demonstrate that the quantum harmonic oscillator in the deformed space induced by the non-additive translation operator becomes equivalent to the symmetric Pöschl–Teller potential when the equilibrium position is at the origin. When the oscillator is displaced from the origin, its potential transforms into the Rosen–Morse potential. Extending the analysis to three dimensions, we show that the full Pöschl–Teller potential emerges naturally as the effective potential in the central force problem—even in the absence of an external potential.

Keywords: Pöschl-Teller potential, Rosen-Morse potential.

Hyperbolic-type potentials have been widely applied across various areas of physics, including molecular physics [1, 2], quantum dots [3], spatial solitons [4], and information entropy analysis [5]. Their bound-state spectra and scattering properties have been extensively studied using a range of analytical and numerical techniques [6–8]. In this work, we introduce a generalized class of hyperbolic potentials defined as:

$$V_{pqs}(x) = A\text{sech}^p(\alpha x) + B\text{csch}^q(\alpha x) + C\tanh^s(\alpha x), \quad (1)$$

where A, B and C are tunable potential parameters, α characterizes the potential range, and p, q, s take integer values that determine the specific form of the potential. By appropriately choosing these exponents, various well-known potentials can be recovered as particular cases. For instance, the choice $p = q = 2$, $s = 0$ corresponds to the modified Pöschl–Teller (PT) potential, originally introduced to model vibrational excitations in molecular systems [9]. This potential has since found diverse applications, including the analysis of quasinormal modes of black holes [10], optical properties of quantum wells [11], solitonic dynamics in Bose–Einstein condensates [12], and waveguiding in two-dimensional Dirac materials [13]. A particularly notable case is the symmetric PT potential with $q = 0$ and $A = -\lambda(\lambda+1)$, which yields a class of reflectionless potentials for integer ¿0¿0, where wave packets are perfectly transmitted regardless of their energy [14, 15].

Another notable case of the generalized potential in Eq. (1) arises for $p = 2$, $q = 0$, $s = 1$, which corresponds to the Rosen–Morse potential. This potential has been extensively used to model diatomic molecular interactions [16], investigate features of supersymmetric quantum mechanics [17], and explore nonlinear quantum effects [18]. In our work, we demonstrate that both the symmetric Pöschl–Teller and the Rosen–Morse potentials emerge naturally as effective interactions when a particle is subjected to a harmonic potential in a deformed, or "contracted", space. This deformation arises from the application of a non-additive translation operator, defined by:

$$\langle x|\, T_\gamma(\epsilon)\, |\phi\rangle = \phi\left(x + \epsilon\left(1 + g(\gamma x)\right)\right), \quad (2)$$

where $g(\gamma x)$ is the deformation function, and γ is a parameter with dimensions of inverse length. When the deformation function is linear in x, the properties of this operator have been thoroughly investigated [19–23], leading to applications in modeling electronic transport in semiconductor heterostructures [24, 25]. Moreover, this formalism connects with Tsallis thermostatistics [26] through its relation to the qq-exponential function. In this work, we extend the analysis to the quadratic case, choosing a deformation function of the form $g(\gamma x) = -(\gamma x)^2$, which leads to the following form of the translation operator:

$$\langle x|\, T_\gamma(\epsilon)\, |\phi\rangle = \phi\left(x + \epsilon\left(1 - \gamma^2 x^2\right)\right). \quad (3)$$

This deformation implies a modified generator of spatial translations, yielding a deformed momentum operator given by:

$$\hat{p}_\gamma = -i\hbar f_\gamma(x)\frac{d}{dx} = -i\hbar D_\gamma, \quad (4)$$

with D_γ denotes the deformed derivative, and $f_\gamma(x) = 1-\gamma^2x^2$ is the position-dependent deformation function. In the limit $\gamma = 0$, we recover the standard momentum operator in Euclidean space. Importantly, $\hat{p}_\gamma$ is Hermitian with respect to the modified scalar product:

$$\langle\varphi|\phi\rangle = \int \frac{dx}{1-\gamma^2x^2}\, \varphi^*(x)\phi(x). \quad (5)$$

* E-mail: michael@fisica.ufc.br
† E-mail: soares@fisica.ufc.br
‡ E-mail: auto@fisica.ufc.br

This inner product defines the appropriate Hilbert space structure in the deformed geometry, ensuring the consistency of the quantum mechanical framework.

Writing down the Schrödinger equation for this deformed space, with the deformed kinetic operator

$$i\hbar\frac{\partial}{\partial t}\phi(x,t) = -\frac{\hbar^2}{2m}\left[(1-\gamma^2x^2)^2\frac{\partial^2}{\partial x^2} -2\gamma^2x(1-\gamma^2x^2)\frac{\partial}{\partial x}\right]\phi(x,t) + V(x)\phi(x,t), \tag{6}$$

the above equation can be obtained alternatively, studying the dynamics of a particle with effective mass, $m_e(x) = m/(1-\gamma^2x^2)$, moving in Euclidean space. In terms of this effective mass, equation (6) can be written

$$i\hbar\frac{\partial}{\partial t}\phi(x,t) = -\frac{\hbar^2}{2}\left[\frac{1}{m_e}\frac{\partial^2}{\partial x^2} + \frac{d}{dx}\left(\frac{1}{2m_e}\right)\frac{\partial}{\partial x}\right]\phi(x,t) + V(x)\phi(x,t), \tag{7}$$

revealing the duality between a particle with constant mass moving in a deformed space and a particle with position dependent mass in flat space, which is a widely studied problem due to their applications in condensed-matter physics [27, 28]. Equations (6) and (7) represent two unconventional type of Schrödinger equations, which are related through specific relations between the deformation function of the mass and the metric tensor [29]. In [21] was shown the explicit relation between the translation operator (2) and the metric tensor of the space, proving that the measure of the space used in (5), $dx/1-\gamma^2x^2$, define a natural change of variables

$$\eta = \frac{\text{Arctanh}(\gamma x)}{\gamma}. \tag{8}$$

With this new variable the Schrödinger equation takes the usual form

$$i\hbar\frac{\partial}{\partial t}Q(\eta,t) = -\frac{\hbar}{2m}\frac{\partial^2}{\partial x^2}Q(\eta,t) + V_{\text{eff}}(\eta)Q(\eta,t), \tag{9}$$

with $Q(\eta,t) = \phi(x(\eta),t)$ and $V_{\text{eff}}(\eta) = V(x(\eta))$.

Square well

Let us consider now a particle described by equation (6) confined in a infinite square well potential of length L, or equivalent in the deformed space $L_\eta = \text{Arctanh}(\gamma L)/\gamma$. The solution of the Schrödinger can be written as

$$\phi_n(x) = \begin{cases} A_n \sin\left[\frac{k_n}{\gamma}\text{Arctanh}(\gamma x)\right], & \text{if } 0 < x < \text{L}, \\ 0, & \text{otherwise}, \end{cases} \tag{10}$$

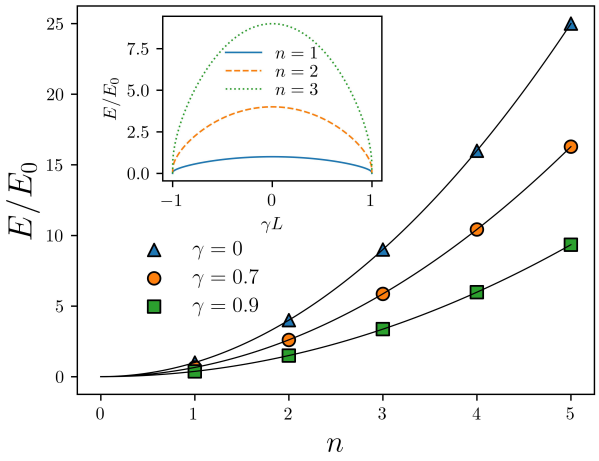

Figure 1. The energy spectrum for a particle confined in a deformed square well. As we can see in (12) the energies are discrete; the solid lines are just guides for the eye. The inset shows the energy against γL for the first three energy levels. In this figure $E_0 = \pi^2\hbar^2/2mL^2$ represents the ground state for the undeformed problem, $\gamma \to 0$.

where the wave vectors are quantized to satisfy the boundary conditions,

$$k_n = \frac{n\pi\gamma}{\text{Arctanh}(\gamma\text{L})}, \quad n = 1, 2, 3, ..., \tag{11}$$

and the corresponding energy eigenvalues

$$E_n = \frac{\hbar^2n^2\pi^2\gamma^2}{2m\,\text{Arctanh}^2(\gamma L)}, \quad n = 1, 2, 3.... \tag{12}$$

In Figure 1, we show how the energy levels of a particle confined in a deformed square well increase with n for different values of γ, also we can see that the energy is maximum in the undeformed case ($\gamma = 0$) and it tends to the minimum value as γ approach to ±1. In Figure 2 we show the behavior of the average position as function of γL, as expected when $\gamma = 0$ the average value is 0.5, whereas γ approach to ±1 the particle is confined in the farthest location from the origin, in contrast with the linear case $g(\gamma x) = \gamma x$ where the particle is confined close the origin as γ increase.

The coefficients A_n in (10) are determined imposing the normalization condition to the wave functions, leading to $A_n^2 = 2/\text{L}_\eta = 2\gamma/\text{Arctanh}(\gamma\text{L})$. Since the position operator in different space directions still commutes, the problem can be straightforward generalized to higher dimensions. For example, in the two dimensional square well problem the corresponding wave function can be written as a product of one-dimensional (10) wave functions as $\Phi(x,y) = \phi(x)\phi(y)$. The contour plots for the probability density, $\rho(x,y) = |\Phi(x,y)|^2$, of the two-dimensional infinite well for different values of the quantum numbers are shown in Fig 3. In the presence of

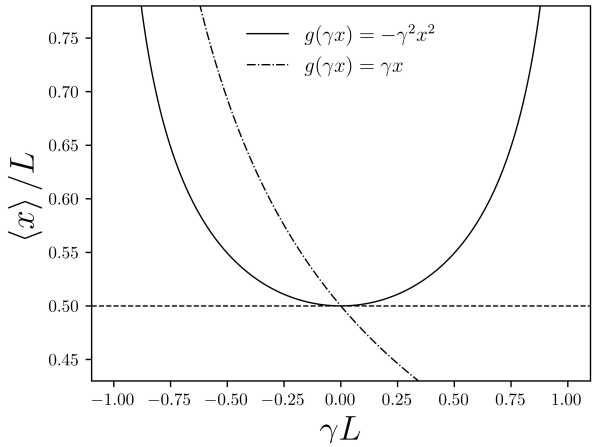

Figure 2. The average position for a particle confined in a deformed square well. The solid line gives the average value of x for a particle described by equation (6), whereas the dashed-dotted correspond to the linear case studied in [19]. Both cases recover the $\langle x \rangle / L = 0.5$ when $\gamma \to 0$.

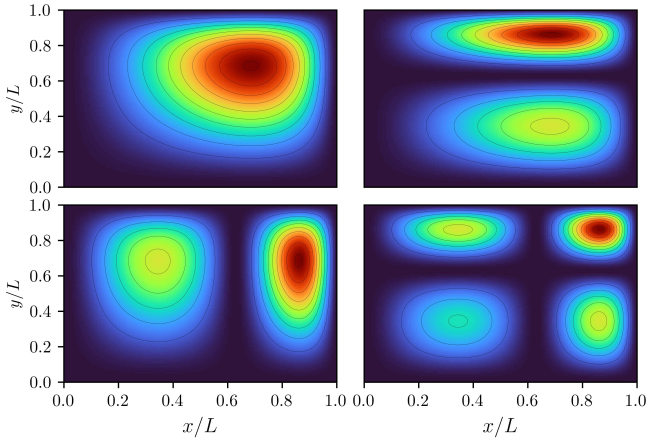

Figure 3. The contour plot of the probability density for a particle in a two-dimensional box for $\gamma = 0.8$, where the quantum numbers are (a) $n_x = n_y = 1$, (b) $n_x = 1$, $n_y = 2$, (c) $n_x = 2$, $n_y = 1$, and (d) $n_x = n_y = 2$. The probability increases from blue to red.

the non-additive translations operator (3) is more likely to find the particle away from the origin, this contrast with the behavior reported in [30] for the linear case $g(\gamma x) = \gamma x$, where the particle stay closer to the origin as γ increases.

Harmonic oscillator

Let us consider a particle confined in the archetypal case of a harmonic oscillator, $V(x) = \frac{1}{2}m\omega^2 x^2$, for this case the transformed potential becomes,

$$V_{\text{eff}}(\eta) = -\frac{m\omega^2}{2\gamma^2}\text{sech}^2(\gamma\eta), \tag{13}$$

where we have used the identity $\tanh^2 x = 1 - \text{sech}^2 x$ and the fact that an additive constant do not affect the equations of motions. We can see that the effective potential (13) takes the form of the symmetric Pöschl-Teller potential by identifying $A = -\frac{m\omega^2}{\gamma^2}$, it also corresponds to the case $p = 2$, $q = s = 0$ in (1). In order to find the solution of the equation (9) with the potential (13) usually is performed a transformation $u = \tanh(\gamma\eta)$, obtaining the wave function solution of the form [31]

$$Q\left(\tanh(\gamma\eta)\right) = N_n^q P^{q-n}\left(\tanh(\gamma\eta)\right), \quad n = 1, 2, 3, ..., \tag{14}$$

where $P^{q-n}(u)$ are the Legendre polynomials, q is related to the deep of the potential, is determined by $q(q+1) = m^2\omega^2/\hbar^2\gamma^2$ and N_n^q is a normalization constant. On the other hand the eigenvalues are determined by

$$E_n = -\frac{\gamma^2\hbar^2}{2m}(q-n)^2. \tag{15}$$

Now considering the case of the harmonic oscillator with the equilibrium position $x_0 \neq 0$, we have $V(x) = \frac{1}{2}m\omega^2(x-x_0)^2$, therefore the corresponding effective potential is

$$V_{\text{eff}}(\eta) = -\frac{m\omega^2}{2\gamma^2}\text{sech}^2(\gamma\eta) - m\omega^2 x_0 \tanh(\gamma\eta), \tag{16}$$

by identifying $A = -\frac{m\omega^2}{\gamma^2}$ and $C = -m\omega^2 x_0$ we conclude that (16) corresponds to the Rosen-Morse potential (case when $p = 2$, $q = 0$, $s = 1$ in (1)).

Three dimensionla case

In [23], was proposed a three dimensional generalization of the deformed momentum $\hat{p}_\gamma$ described in equation (4), in order to obtain a formalism to describe screening potentials from the central force problem in a deformed space. Using the same approach for the space characterized by the deformation function $f_\gamma(r) = 1 - \gamma^2 r^2$, we obtain the generalization of the momentum operator in spherical coordinates as

$$\hat{P}_\gamma = -i\hbar(1-\gamma^2 r^2)\nabla = -i\hbar\nabla_\gamma, \tag{17}$$

then, the kinetic operator determined by equation (17) gives the following Schrodinger equation

$$i\hbar\frac{\partial}{\partial t}\psi(\mathbf{r}) = -\frac{\hbar^2}{2m}(1-\gamma^2r^2)\nabla(1-\gamma^2r^2)\nabla\psi(\mathbf{r}) \quad (18)$$
$$V(r)\psi(\mathbf{r}).$$

Both, the deformation function and the potential act only in the radial direction, then equation (18) is separable, and the wave function can be written as $\psi(\mathbf{r}) = R(r)Y_{\ell m}(\theta,\varphi)$, where $Y_{\ell m}(\theta,\varphi)$ are the spherical harmonics. Using the fact that $\psi(\mathbf{r})$ is an eingenfunction of $\hat{L}^2$ with eigenvalues $L^2 = \ell(\ell+1)\hbar^2$, we obtain the radial differential equation

$$ER(r) = -\frac{\hbar^2}{2m}\left(f_\gamma^2(r)\left(\frac{\mathrm{d}}{\mathrm{d}r}+\frac{2}{r}\right)+f_\gamma(r)f_\gamma'(r)\right)\frac{\mathrm{d}}{\mathrm{d}r}R(r) + \left(\frac{f_\gamma^2(r)L^2}{2mr^2}+V(r)\right)R(r). \quad (19)$$

A common way to tackle the radial part of the Schrodinger equation is to define $Q(r) = rR(r)$, which leads to

$$EQ(r) = \left[V_{\text{eff}}(r) - \frac{\hbar^2}{2m}\left((1-\gamma^2r^2)^2\frac{d^2}{dr^2} - 2\gamma^2r(1-\gamma^2r^2)\frac{d}{dr}\right)\right]Q(r), \quad (20)$$

with the effective potential given by

$$V_{\text{eff}}(r) = -\frac{\gamma^2}{2m}(L^2+\hbar^2)\text{sech}^2(\gamma\eta)+\frac{L^2\gamma^2}{2m}\text{csch}^2(\gamma\eta)+V(\eta), \quad (21)$$

Surprisingly, even considering that the external potential vanishes, $V(\eta) = 0$, we have an interesting form of the potential, indeed it has the same form of the Pöschl-Teller potential (the $p = q = 2$, $s = 0$ case in equation (1)).

[1] S. M. Ikhdair, International Journal of Modern Physics C **20**, 1563 (2009).
[2] U. S. Okorie, A. N. Ikot, C. Edet, G. Rampho, R. Sever, and I. Akpan, Journal of Physics Communications **3**, 095015 (2019).
[3] G. Liu, K. Guo, H. Hassanabadi, and L. Lu, Physica B: Condensed Matter **407**, 3676 (2012).
[4] Y.-Y. Wang, C.-Q. Dai, and X.-G. Wang, Nonlinear dynamics **77**, 1323 (2014).
[5] G.-H. Sun, S.-H. Dong, K. D. Launey, T. Dytrych, and J. P. Draayer, International Journal of Quantum Chemistry **115**, 891 (2015).
[6] H. Eğrifes, D. Demirhan, and F. Büyükkiliç, Physica Scripta **59**, 90 (1999).
[7] F.-K. Wen, Z.-Y. Yang, C. Liu, W.-L. Yang, and Y.-Z. Zhang, Communications in Theoretical Physics **61**, 153 (2014).
[8] M. Miranda, G.-H. Sun, and S.-H. Dong, International Journal of Modern Physics E **19**, 123 (2010).
[9] G. Pöschl and E. Teller, Zeitschrift für Physik **83**, 143 (1933).
[10] E. Berti, V. Cardoso, and A. O. Starinets, Classical and Quantum Gravity **26**, 163001 (2009).
[11] H. Yıldırım and M. Tomak, Physical Review B **72**, 115340 (2005).
[12] B. B. Baizakov and M. Salerno, Physical Review A **69**, 013602 (2004).
[13] R. Hartmann and M. Portnoi, Scientific Reports **7**, 1 (2017).
[14] N. Kiriushcheva and S. Kuzmin, American Journal of Physics **66**, 867 (1998).
[15] J. Lekner, American Journal of Physics **75**, 1151 (2007).
[16] G.-D. Zhang, J.-Y. Liu, L.-H. Zhang, W. Zhou, and C.-S. Jia, Physical Review A **86**, 062510 (2012).
[17] K. Oyewumi and C. Akoshile, The European Physical Journal A **45**, 311 (2010).
[18] B. Midya and R. Roychoudhury, Physical Review A **87**, 045803 (2013).
[19] R. Costa Filho, M. Almeida, G. Farias, and J. Andrade Jr, Physical Review A **84**, 050102 (2011).
[20] R. N. Costa Filho, G. Alencar, B.-S. Skagerstam, and J. S. Andrade, EPL (Europhysics Letters) **101**, 10009 (2013).
[21] R. N. Costa Filho, J. P. Braga, J. H. Lira, and J. S. Andrade Jr, Physics Letters B **755**, 367 (2016).
[22] B. G. Da Costa, I. S. Gomez, and M. A. Dos Santos, EPL (Europhysics Letters) **129**, 10003 (2020).
[23] M. T. Ramirez, J. S. de Andrade Jr, and A. A. Moreira, Europhysics Letters (2022).
[24] E. Barbagiovanni, D. Lockwood, N. Rowell, R. Costa Filho, I. Berbezier, G. Amiard, L. Favre, A. Ronda, M. Faustini, and D. Grosso, Journal of Applied Physics **115**, 044311 (2014).
[25] E. Barbagiovanni and R. Costa Filho, Physica E: Low-dimensional Systems and Nanostructures **63**, 14 (2014).
[26] C. Tsallis, Journal of statistical physics **52**, 479 (1988).
[27] O. von Roos, Physical Review B **27**, 7547 (1983).
[28] G. Bastard, (1990).
[29] C. Quesne and V. Tkachuk, Journal of Physics A: Mathematical and General **37**, 4267 (2004).
[30] S. H. Mazharimousavi, Physical Review A **85**, 034102 (2012).
[31] S.-H. Dong and R. Lemus, International journal of quantum chemistry **86**, 265 (2002).

These two works were developed during the PhD but were not included as part of this thesis, as they address topics that differ significantly from the main focus of the research. While the core of this thesis lies in the study of non-equilibrium dynamics in active matter systems, the additional works explore problems in quantum mechanics and field theory, particularly involving deformed spaces and extended operator formalisms. Despite their thematic divergence, these studies reflect the broader scope of theoretical interests pursued throughout the doctoral period.